Surface Interactions of Layered Chalcogenides in Covalent Functionalization and Metal Adsorption

by

Duo Li

A Dissertation Presented in Partial Fulfillment
of the Requirements for the Degree
Doctor of Philosophy

Approved July 2019 by the
Graduate Supervisory Committee:

Qing Hua Wang, Chair
Alexander A. Green
Candace K. Chan
Yang Jiao

ARIZONA STATE UNIVERSITY

August 2019

ABSTRACT

Layered chalcogenides are a diverse class of crystalline materials that consist of covalently bound building blocks held together by van der Waals forces, including the transition metal dichalcogenides (TMDCs) and the pnictogen chalcogenides (PCs) among all. These materials, in particular, MoS_2 which is the most widely studied TMDC material, have attracted significant attention in recent years due to their unique physical, electronic, optical, and chemical properties that depend on the number of layers. Due to their high aspect ratios and extreme thinness, 2D materials are sensitive to modifications via chemistry on their surfaces. For instance, covalent functionalization can be used to robustly modify the electronic properties of 2D materials, and can also be used to attach other materials or structures. Metal adsorption on the surfaces of 2D materials can also tune their electronic structures, and can be used as a strategy for removing metal contaminants from water. Thus, there are many opportunities for studying the fundamental surface interactions of 2D materials and in particular the TMDCs and PCs.

The work reported in this dissertation represents detailed fundamental studies of the covalent functionalization and metal adsorption behavior of layered chalcogenides, which are two significant aspects of the surface interactions of 2D materials. First, we demonstrate that both the Freundlich and Temkin isotherm models, and the pseudo-second-order reaction kinetics model are good descriptors of the reaction due to the energetically inhomogeneous surface MoS_2 and the indirect adsorbate-adsorbate interactions from previously attached nitrophenyl (NP) groups. Second, the covalent functionalization using aryl diazonium salts is extended to nanosheets of other representative TMDC materials $MoSe_2$, WS_2, and WSe_2, and of the representative PC materials Bi_2S_3 and Sb_2S_3, demonstrated using atomic force

microscopy (AFM) imaging and Fourier transform infrared spectroscopy (FTIR). Finally, using AFM and X-ray photoelectron spectroscopy (XPS), it is shown that Pb, Cd Zn and Co form nanoclusters on the MoS_2 surface without affecting the structure of the MoS_2 itself. The metals can also be thermally desorbed from MoS_2, thus suggesting a potential application as a reusable water purification technology.

DEDICATION

To all who have helped and supported me.

ACKNOWLEDGEMENTS

First and foremost, I must thank Dr. Qing Hua Wang, who offered me the opportunity of pursuing my PhD degree at Arizona State University (ASU) when I was still exploring which research area that I would be interested in. I really appreciate the guidance and support she has provided not only as my advisor, but also as a friend.

I would also like to acknowledge other members of my committee, Dr. Alexander Green, Dr. Candace Chan and Dr. Yang Jiao, for their help and encouragement to broaden my perspective of my research area. I also appreciate the unselfish help and support from the members of our research group and collaborated group. In particular, Dr. Ximo Chu has helped to set up the chemical vapor deposition system. Suneet Kale and Matthew Gilliam have helped me with characterization for my projects.

During years of research, many research scientists and technicians have helped me. I gratefully acknowledge Dr. Hao Yan for generously allowing me to use the Raman spectroscopy and atomic force microscope (AFM) belonging to his research group and I appreciate the training and help provided by Dr. Shuoxing Jiang. Dr. Gwyneth Gordon and Dr. Trevor Martin have helped me with the training and operation of the inductively coupled plasma mass spectrometry (ICP-MS) system. Dr. Timothy Karcher and Dr. Shreya Bhattacharyya have helped me with surface characterization.

I would also like to thank my parents and my friends, for their continuous support and encouragement.

Finally, I gratefully acknowledge the funding support from ASU Startup

Funding, Salt River Project and Nanosystems Engineering Research Center for Nanotechnology-Enabled Water Treatment (NEWT) (EEC-1449500). I also acknowledge the use of equipment from Goldwater Materials Science Facility, John M. Cowley Center for High Resolution Electron Microscopy and W. M. Keck Foundation Laboratory for Environmental Biogeochemistry.

TABLE OF CONTENTS

CHAPTER Page

CHAPTER Page

CHAPTER Page

LIST OF TABLES

LIST OF FIGURES

Figure Page

Figure Page

Chapter 1

INTRODUCTION AND MOTIVATION

1.1 Surface Interactions of Two-Dimensional Materials

Over the past few decades, dimensionality has been shown to play a crucial role in determining the properties of materials[1, 2]. Nanostructured materials feature one or more dimensions that are reduced to nanometer-scale sizes, resulting in new properties that differ from those of the bulk material. Recently, the most prominent form of nanomaterials are two-dimensional (2D) materials, which often have corresponding in bulk forms with atomically thin layers stacked together with weak interlayer attractions[3]. The rapid development in our understanding of graphene, the prototypical 2D material composed of atomic layers of carbon, has led to significant research efforts other 2D materials which can be exfoliated to ultrathin layers[1, 4, 5], such as transitional metal dichalcogenides (TMDCs)[6, 7], pnictogen chalcogenides (PCs)[8, 9], elemental graphene analogues[10, 11], and perovskite-based oxides[12, 13].

In particular, 2D TMDCs are more promising in electronic applications than semi-metallic graphene because some of them are naturally abundant semiconductors with sizable bandgaps[4, 5]. As shown in **Figure 1.1a**, TMDCs are a class of materials with formula MX_2, where M represents a transition metal element from groups IV, V or VI, and X represents a chalcogen (S, Se, and so on). These materials exist as stacked layers of the form X-M-X, with a hexagonal plane of metal atoms sandwiched by two hexagonal planes of chalcogen[14]. Each of these sandwich-structured

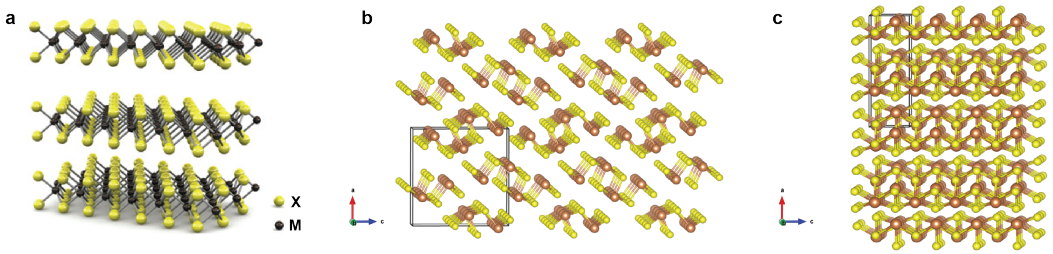

Figure 1.1: Structure of TMDCs and PCs. (a) 3D schematic illustration of a typical MX_2 structure, with X representing chalcogen atoms and M representing metal atoms[14]. (b)-(c) Crystal structures of Pn_2X_3 materials inside and top views (yellow atoms: X; brown atoms: Pc).

layers are covalently bound internally, but there are weak vdW interactions between adjacent layers, so TMDCs can be relatively easily delaminated to monolayer thickness, with dramatic changes of electronic properties as summarized in **Table 1.1**.

The PCs are another class of layered chalcogenides, with the general formula Pn_2X_3, where Pn is a group 15 pnictogen (Pn = As, Sb, and Bi). While the broader group includes semiconductors, topological insulators, and thermoelectrics, here in this thesis we focus on the semiconductors Sb_2S_3 and Bi_2S_3. These materials have been grown in thin films[8], nanowires and nanorods[9, 20–24], and exfoliated into 1D nanoribbons and 2D nanosheets[25–27]. Examples of applications for Bi_2S_3 and Sb_2S_3 include solar cells, batteries, and catalysts[9, 20, 27–30]. The crystal structure of the Pn_2X_3 materials including Sb_2S_3 (antimony trisulfide or antimonite or stibnite) and Bi_2S_3 (bismuth(III) sulfide or bismuthinite), which belong to the Pnma space group (No. 62), are shown in **Figure 1.1b** and **c**.

While the layered chalcogenides have many promising optical, magnetic, and electronic properties[1, 2, 4, 5], strategies for taking advantage them in a range of applications requires understanding and controlling their surface interactions.

	-S_2	-Se_2	-Te_2
Nb	Metal; Superconducting; CDW[16]	Metal; Superconducting; CDW[16]	Metal[15]
Ta	Metal; Superconducting; CDW[16]	Metal; Superconducting; CDW[16]	Metal[15]
Mo	Semiconducting;[4] 1L:1.8 eV; Bulk:1.2 eV	Semiconducting;[17] 1L:1.5 eV; Bulk:1.1 eV[18]	Semiconducting;[17] 1L: 1.1 eV; Bulk:1.0 eV
W	Semiconducting;[19] 1L:2.1 eV; 1L:1.9 eV;[17] Bulk:1.4 eV[18]	Semiconducting;[15] 1L:1.7eV; Bulk:1.2 eV[18]	Semiconducting;[15] 1L:1.1 eV

Table 1.1: Summary of TMDC Materials and Properties. The electronic properties of TMDC materials are listed as metallic, superconducting, semiconducting or charge density wave (CDW). For the semiconducting materials, the bandgap energies for monolayer (1L) and bulk forms are listed.

Because of their atomic thinness, they have very high surface-to-volume ratios so that their surfaces can greatly affect their behaviors[1, 2, 31–33] In particular, in this thesis we will focus on the covalent functionalization with organic molecules and the adsorption of metal ions.

1.2 Motivations

The work in this thesis is motivated by the need for fundamental studies on understanding the surface interactions of layered chalcogenides. First, the direct

covalent functionalization of MoS_2 using aryl diazonium salts was demonstrated in our group's earlier work in Chu *et al.*[34]. However, the reaction kinetics also plays a crucial role in the functionalization and needs to be further studied to achieve a full understanding of the reaction process and to enable more precise control of the functionalization. Moreover, there exists an unmet need for mild chemistries that will enable direct covalent functionalization of semiconducting TMDC and PC surfaces other than MoS_2. It is crucial to demonstrate a generalizable and broadly applicable approach for modifying the surface of more TMDCs and PCs.

Second, the adsorption of metals onto TMDCs has recently been reported for doping[35] and for the removal of heavy metal ions from water[36–40]. However, the previous reports have primarily focused on either theoretical simulations or evaluation of macroscopic performance, rather than microscopic characterization. Thus, there is a need to study the fundamental interaction between TMDC surfaces and adsorbed metal ions, in particular the morphology, mechanism, and structure.

1.3 Overview of Thesis

In this thesis, we report three detailed studies of different aspects of the surface chemistry of 2D metal chalcogenides. First, in Chapter 2, we presented more detailed background on several important aspects of the synthesis, characterization, and surface functionalization of TMDCs and PCs. In **Chapter 3**, we present a detailed study of the reaction kinetics for the direct covalent functionalization of unmodified semiconducting 2H-MoS_2 by the aryl diazonium salt 4-NBD, which was first shown in our earlier work (see Chu *et al.*[34]), and which has been used to probe the chemical reactivity of graphene[41–43]. Here, we chose 4-NBD as a model compound to

investigate the reaction kinetics of the functionalization by conducting an adsorption isotherm with varying concentrations of 4-NBD aqueous solution using different models to fit the data to describe the reaction. In addition, the reaction kinetics and spatial distribution of the resulting nitrophenyl (NP) groups covalently attached on the surface of MoS_2 were studied via a series of reactions at different concentrations and time sequences. We find that the best models to describe the process are the Temkin and Freundlich adsorption models and pseudo-second-order kinetics model in which the adsorbate−adsorbate interaction is considered. These findings are also consistent with our previous DFT simulations (see Chu *et al.*[34]) Previous literature on the kinetics of the diazonium functionalization of graphene showed a first-order reaction[24], which, we find, does not adequately describe the scenario for MoS_2.

In **Chapter 4**, we expand this covalent functionalization with aryl diazonium salts to several other members of the TMDC and PC families beyond MoS_2 to further extend the applicability and broad utility of this chemistry, namely to functionalize $MoSe_2$, WS_2, WSe_2, Bi_2S_3, and Sb_2S_3. We prepare and functionalize samples of these materials using mechanical exfoliation, liquid phase dispersion, and chemical vapor deposition (CVD) techniques. Using vibrational and absorbance spectroscopies, we show the formation of chemical bonds and attachment of functional groups to the TMDC and PC nanosheets. Using atomic force microscopy (AFM), we show the spatial distribution of NP groups across the TMDC and PC surfaces with functionalization. This work shows that the covalent functionalization using aryl diazonium salts can indeed be applied to many related layered chalcogen materials, thus greatly expanding the scope of utility of the chemical scheme, and that it can open the door to further modifications of these materials. These surface-modified nanomaterials have potential applications in biosensing, antimicrobial, therapeutic,

environmental, energy, and optoelectronic applications. The winder literature on the diazonium functionalization of 2D materials and carbon nanomaterials, which has demonstrated changes to properties such as the electronic and transport[44], shifts in optical emission[34], and the covalent attachment of other materials[34, 41, 43] like proteins, polymers, and quantum dots, can be brought to inform future work on TMDCs and PCs.

Finally, in **Chapter 5**, we report the adsorption of heavy metal ions from aqueous solutions onto the surface of MoS_2 nanosheets and subsequent formation of nanoclusters. We characterize these adsorbed structures using AFM and XPS to show the presence of Pb, Cd, Zn and Co. The metal nanoclusters can be desorbed from the surface of MoS_2 by thermal annealing. The MoS_2 nanosheets can then be incorporated into three-dimensional structures polyurethane foam, which can then be used for removal of heavy metal contamination at trace concentrations from water.

Chapter 2

BACKGROUND

In this chapter, we introduce more detailed background including synthesis, characterization, and previous work on surface interactions of TMDC and PC materials.

2.1 Synthesis and Characterization of TMDCs and PCs

2.1.1 Mechanical Exfoliation

Mechanical exfoliation was the technique originally developed to prepare graphene[3–5, 45, 46]. Atomically thin flakes of TMDCs can be acquired from peeling apart bulk crystals to induce micromechanical cleavage using scotch tape, then applied to target substrate and identified by using optical microscopy[14, 47]. A flake of as-exfoliated MoS_2 with regions of different layer numbers is shown in **Figure 2.1b**. The samples of TMDCs prepared using this method are very high-quality crystals with very few defects, so that they are suitable for various types of fundamental research[48]. However, the size of the flakes is limited to usually a few microns across.

2.1.2 Liquid Phase Exfoliation

As shown in **Figure 2.1d**, TMDCs can be exfoliated by ultrasonication in liquids such as aqueous surfactant solutions, organic solvents, or solutions of polymer in solvents[49, 50]. Typically, the sizes of flakes acquired using this method are a few hundred nanometers which is also rather small. However, a large amount of material can be produced by this method in a dispersion that is compatible with solution

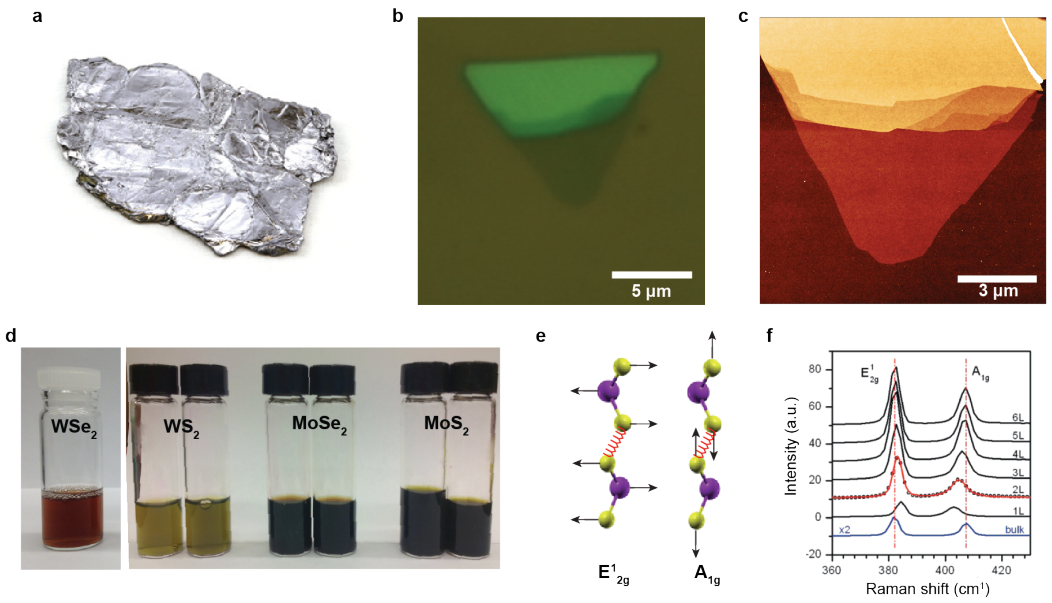

Figure 2.1: Preparation and characterization of TMDCs. (a) A photograph of bulk crystal of MoS_2. (b) Optical microscopy image of mechanically exfoliated MoS_2 monolayer and multilayer from our current experimental work. (c) AFM image of MoS_2 flake shown in b. (d) Liquid phase dispersion of TMDCs prepared by Dr. Alexander Green's group. (e) A schematic illustration of two phonon vibration modes corresponding to typical Raman peaks of MoS_2. (f) A series of Raman spectra show thickness dependence.

phase processing steps, so that it is promising for experiments that require large quantities of materials[49].

2.1.3 Chemical Vapor Deposition (CVD)

Uniformly, large area of TMDCs are needed for the fabrication of electronic and optoelectronic devices[46, 51, 52]. Atomically thin films of MoS_2 can be grown on insulating substrates using chemical vapor deposition (CVD) methods[52]. As shown in **Figure 2.2**, different precursors have been used to generate MoS_2: MoO_3 powder and sulfur powder were heated to become vapors and co-deposit on the

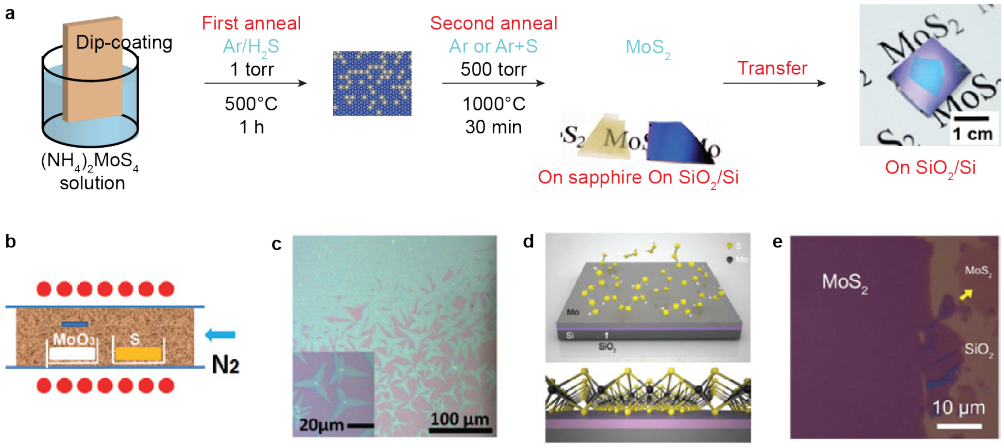

Figure 2.2: Synthesis of MoS_2 by CVD with different precursors. (a) The process of synthesizing MoS_2 from a dip-coated chemical precursor on SiO_2/Si or sapphire substrate. (b) Schematic of CVD synthesis of MoS_2 from S and MoO_3 powders. Red dots indicate the heating coil of a tube furnace. (c) Optical microscope image of CVD grown MoS_2, where blue star shapes are MoS_2, and the purple background is SiO_2/Si substrate. (d) A schematic illustration of CVD MoS_2 synthesized from a solid layer of Mo. (e) Optical microscope image of MoS_2 grown from solid film of Mo, where dark and light purple regions are MoS_2 of different thickness, and brown background is substrate. a, ref 26, b & c, ref 24, d & e, ref 25.

target substrate[46, 53]; substrates were dip-coated with a solution of $(NH_4)_2MoS_4$ in dimethylformamide (DMF), and heated in a sulfur vapor[52]; a thin film of Mo metal was deposited onto target substrate, and heated in a sulfur vapor[51]. In general, the thickness of the MoS_2 film produced depends on the concentration of precursors or the initial thickness[54], and the areas are on the order of centimeters. These methods have already resulted in MoS_2 films that are large enough for fabricating devices and for use with characterization tools that requires larger areas, including Fourier transform infrared spectroscopy (FT-IR) and X-ray photoelectron spectroscopy (XPS).

2.1.4 Characterization

There are many techniques that are used to characterize 2D TMDCs. Optical microscopy can be used to identify monolayer and few-layer crystals of 2D materials, due to the optical interference of the crystals on SiO_2 capping layers of precise thicknesses on Si wafer substrates[55]. Raman spectroscopy can detect the phonon vibration of the materials[56], and based on the typical Raman peaks of TMDCs, we can identify the materials, and also estimate their thicknesses due to the layer number dependence of the positions of particular characteristic peaks[46], shown in **Figure 2.1e** and **f**. With a spatial map of Raman spectra, the uniformity of a specific flake can be shown[57]. Atomic force microscopy (AFM) is essential and commonly used for TMDCs since it is usually used to characterize thin films. It can provide us information about the morphology and roughness of the surface[57], and layer thicknesses. In addition, techniques that are used for thin films, including transmission electron microscopy[57] (TEM) and scanning electron microscopy (SEM), are also used for characterization of 2D TMDCs.

2.2 Chemical Functionalization

2.2.1 Functionalization of TMDCs

In order to utilize the various properties of 2D layered chalcogenides, surface interaction/modification is significant due to the high surface-to-volume ratio and their relatively weak reactivity[58, 59]. Covalent functionalization of TMDCs, in particular, MoS_2, has been drawing attentions in recent years[58]. The chemical functionalization of nanomaterials is used to tune their physical properties, control their interfacial interactions with other materials, and to protect them from dele-

terious environments. In general, 2D materials like graphene can be functionalized by both covalent and non-covalent methods[43, 60, 61]. For example, the surface functionalization of TMDCs can allow them to have improved biosensing capabilities by introducing biophilic moieties to bind particular biomolecules[62–64], better antimicrobial activity[65, 66], sorption of contaminants from water[67], and doping of the semiconducting material[68].

Semiconducting TMDCs, however, due to the lack of dangling bonds on their basal planes[55, 69], are less reactive than the low-dimensional carbon allotropes. Previously reported methods of covalent functionalization of semiconducting TMDCs have required the participation of aggressive chemicals to enhance the formation of covalent bond or harsh treatments that impair the desirable properties of the TMDCs. For example, it was reported that using organoiodides (Voiry *et al.*[70]) and aryl diazonium salts (Knirsch *et al.*[71]), respectively, MoS_2 can be covalently functionalized only after being conversed from the semiconducting 2H phase to the electron-rich metallic 1T phase. These previous works require the highly pyrophoric n-butyllithium to promote the formation of the metallic MoS_2 phase. During the treatment, either the S plane or both S and Mo plane will glide and the crystal structure of MoS_2 transforms from trigonal to octahedral[72]. The Fermi-level shifts from the d band gap to the d band[73] which is easier to be accessed by electrons and ions resulting in, abolishing the semiconducting and photoluminescence properties of the pristine 2H phase as shown in **Figure 2.3**. Lei *et al.* applied $TiCl_4$ and $SnCl_4$ to form coordination bonds with S or Se atoms on the surface of TMDCs via Lewis acid-base mechanism[74]. However, the metal chlorides are highly volatile and they either decompose in air or dramatically react with water releasing HCl[75]. In addition, milder chemistries have been reported to be limited to noncovalent

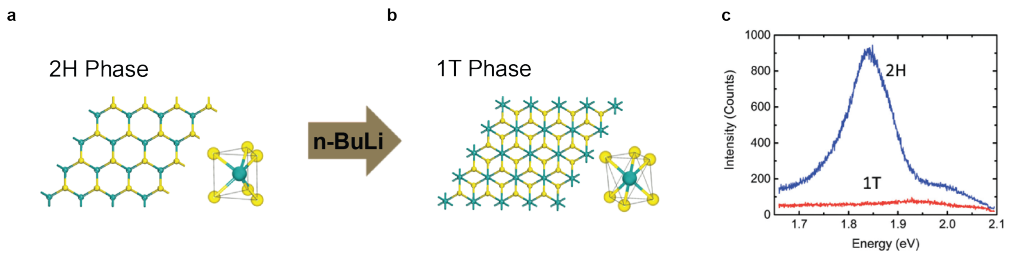

Figure 2.3: Transformation of MoS_2 from 2H phase to 1T phase. (a) Atomic structure of pristine 2H-MoS_2 (b) Atomic structure of 1T-MoS_2 after treatment using n-butyllithium. (c) Photoluminescence (PL) spectra of 2H-MoS_2 and 1T-MoS_2. The PL emission nearly disappears after transformation from 2H to 1T.

bonds or defect sites on TMDC surface. Even though various organic[63, 69, 76–79] and inorganic[27] chemicals have been used for noncovalent functionalization of TMDC[23, 80], these interactions are not as robust as covalent bonds due to relying on physisorption to the TMDC surface. It was also demonstrated that metal acetates[81] and ligand[78, 79] conjugated at defect sites on semiconducting TMDCs, but the maximum coverage is always limited to the initial binding sites.

2.2.2 Functionalized MoS_2 in Applications

There has been increasing interest in using MoS_2 nanosheets in environmental applications as sorbents and ion-exchange materials for heavy-metal ions[82, 83] and organic contaminants[84–86]. However, the 1T phase of MoS_2 is susceptible to corrosion[45] and recent studies have shown that the removal mechanism of pollutants on MoS_2 is likely from redox[40] or precipitation[87] reactions mediated by the solubilized molybdate ions, rather than from adsorption, although covalent functionalization of the 1T-MoS_2 surface can enable high capacity and multifunctional removal of pollutants[67]. Covalent functionalization of the more stable 2H-MoS_2 phase may offer a route toward using these materials as sorbents

through the attachment of organic functional groups that can selectively remove pollutants. In general, covalent functionalization is an important route for tuning the properties of 2D materials[34, 88–91], for engineering their interactions with external environments[77, 92], and for potential applications including transistors[14, 77, 92], flexible electronics[93, 94], and biosensors[95, 96].

2.2.3 Direct Covalent Functionalization of MoS_2

Recently, we reported (see Chu *et al.*[34]) that the basal plane of unmodified semiconducting 2H-MoS_2 can be directly covalently functionalized using aryl diazonium salts 4- nitrobenzene diazonium tetrafluoroborate (4-NBD) without any pretreatment and without the conversion to the metallic 1T phase that previous researchers have used[71, 97]. The schematic is shown in **Figure 2.4**. When the 4-NBD molecule approaches, the charges at MoS_2 surface cause the break between the diazonium group and the benzene ring resulting in a nitrogen (N_2) molecule and a nitrobenzene radical. From density functional theory (DFT) calculations in our earlier work[34], we showed a S-vacancy or defect will allow the nitrobenzene radical to covalently attached to a S atom with a stable binding energy. Moreover, we developed a reaction mechanism where the functionalization initiates from a single defect or S-vacancy due to the increased density of states in MoS_2 at these locations. The region immediately surrounding a covalently attached group also has increased reactivity, so that subsequent covalent attachment will preferentially occur next to an existing group, resulting in the covalent functionalization propagating across the surface of MoS_2 in a chain-like formation. Thus, a very low initial concentration of defects is needed to nucleate the covalent surface functionalization across the entire MoS_2 basal plane. However, more information relating to reaction kinetics is

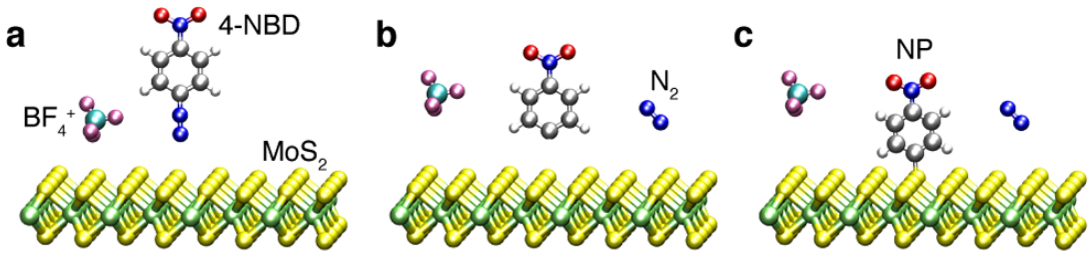

Figure 2.4: Schematic illustrations of the direct covalent functionalization. (a)-(c) The diazonium group breaks from 4-NBD as a N_2 molecule due to charges at the MoS_2 surface. The nitrobenzene radical covalently attaches to a sulfur atom on the surface, resulting in a nitrophenyl (NP) functional group[34].

still essential to control the aryl diazonium salts functionalization chemistry more precisely.

2.2.4 Functionalization of Other TMDCs and PCs

Aryl diazonium functionalization has also previously been applied to other materials such as graphene[41–43, 61] black phosphorus,[98], and carbon nanotubes[99]. The TMDCs, in particular MoS_2, have been the focus of several surface functionalization studies[63, 70, 71], and a variety of approaches and chemical schemes have been used[64, 70, 74, 100–104]. Many of these methods require lithium-based phase conversion or the formation of defects. There have also been some examples of surface functionalization for the PCs[97, 105–107]. It is reported that chitosan functionalized Bi_2S_3 quantum dot has been studied as a candidate for fluorescent biomarker[105, 106] and the polyvinylpyrrolidone functionalized rGO/Bi_2S_3 has potential to be applied for chemo-photothermal therapy of cancer[107]. However, there are fewer such methods for PCs than for TMDCs to the best of our knowledge.

2.3 Adsorption Behavior of Metal Ions on MoS_2 Surface

Other than covalent functionalization, the metal adsorption is another significant aspect relating to surface interaction of MoS_2[11]. MoS_2 is two-dimensional with a high surface-to-volume ratio, making it attractive for the size reduction of devices[1, 2, 31–33]. In addition, there is a great potential to use transitional metal atoms to modulate the electronic and magnetic properties of MoS_2[35]. Moreover, in contrast to graphene, MoS_2 itself is catalytic[108] without functionalization and doping. It is reported that MoS_2 nanosheets have already been applied to epitaxial growth of Au, Ag, Pd and Pt and ambient conditions[109]. Based on the research relative to MoS_2 and metals, there is a great opportunity to experimentally study the adsorption of metals on MoS_2 since there is a great deal of first-principles simulations of the interaction between metals and MoS_2[15]. Adsorption energy, stable geometry, and electronic properties were studied by means of first-principle computations within density functional theory (DFT)[33] and different metals have various adsorption energy on MoS_2 and it affects the stability of the adsorption[33, 35].

Besides, multiple industrial and household sources induce heavy metal contamination in water supplies[110, 111]. Our health can be threatened by heavy metal in water, such as organ damage caused by Cd poisoning and developmental delay in children caused by Pb poisoning[110]. It is reported that the fact that the adsorption of metals on MoS_2 has already been used to removal the heavy metals from water[36–40]. For instance, Wang *et al.*[40] reported the removal of Ag from water using layer-stacked MoS_2 membranes and Ai *et al.*[39] demonstrated the removal of Hg from natural water samples using widened defect-rich nano MoS_2. Embedded in saw dust, MoS_2 nanosheets can also remove Pb selectively from water

when competitor ions are present[36]. However, some aspects in the adsorption of metal on MoS_2 are still unclear, such as the morphology change after the process.

Chapter 3

REACTION KINETICS FOR THE COVALENT FUNCTIONALIZATION OF TWO-DIMENSIONAL MOS_2 BY ARYL DIAZONIUM SALTS

3.1 Background

The two-dimensional transition metal dichalcogenide (TMDC) molybdenum disulfide (MoS_2) has been intensely studied in the past several years due to its exceptional electronic, optical, and chemical properties in a wide range of applications. The chemical functionalization of MoS_2 allows its properties and interfacial interactions to be tuned and controlled. Recently, we reported the direct covalent functionalization of semiconducting MoS_2 with aryl diazonium salts, without the use of harsh initial treatments or phase engineering.

In this chapter, we confirm and expand the covalent functionalization reaction model by performing a detailed study of the reaction kinetics for monolayer MoS_2 functionalized by 4-nitrobenzene tetrafluoroborate (4-NBD). We find that both the Freundlich and Temkin isotherm models are good descriptors of the reaction due to the energetically inhomogeneous surface of MoS_2 and the indirect adsorbate-adsorbate interactions from previously attached nitrophenyl (NP) groups, respectively. The reaction kinetics was then found to be well described using a pseudo-second-order model, showing that the order of this reaction is two. This study supports our previous work and gives us a deeper understanding of the nature of the covalent functionalization of MoS_2.

3.2 Experimental Methods

3.2.1 Sample Preparation

Si substrates with a 300 nm layer of SiO_2 were ultrasonically cleaned in sequential baths of acetone and isopropyl alcohol and then blown dry with ultrahigh purity nitrogen gas. MoS_2 flakes were prepared by the mechanical exfoliation method from a bulk crystal (SPI Supplies) using scotch tape and deposited on the clean substrates. Tape residue was removed by annealing the samples in vacuum at 300°C for 3 hours. Monolayer and multilayer MoS_2 flakes were identified on the substrate by optical microscopy and Raman spectroscopy.

3.2.2 Functionalization Reaction

MoS_2 flakes deposited on SiO_2/Si were immersed in various concentrations of 4-nitrobenzenediazonium tetrafluoroborate (4-NBD) (Sigma Aldrich) aqueous solutions at 35°C with constant stirring at 125 rpm. The reaction was performed in a parafilm-sealed beaker in the dark. At specific reaction times, the samples were extracted from the solutions, rinsed with ultrapure water to remove non-covalently attached molecules, blown dry with ultrahigh purity nitrogen gas, and then characterized.

3.2.3 Atomic Force Microscopy (AFM)

AFM images were taken after each reaction time using a Multimode V system (Bruker Inc.) in ScanAsyst mode with ScanAsyst-Air tips (tip diameter: 2 nm).

3.2.4 Image Processing and Calculations

AFM images were processed using the Gwyddion software package.[112] The coverage calculations were performed using ImageJ.[113] The adsorption isotherm and reaction kinetics curves were fitted using Matlab.

3.2.5 Raman Spectroscopy

Raman spectroscopy and optical microscopy were conducted on a WITec alpha300R system confocal Raman microscope system. Raman spectra were obtained with a 532 nm excitation laser and 100X objective lens with 1 μm laser spot size. The laser power was kept to 0.3 mW to minimize damage to the MoS_2 samples.

3.2.6 Scanning Tunneling Microscopy

STM imaging was conducted on an ultrahigh vacuum (UHV) ScientaOmicron VT system with base pressure around 10-10 mbar operating at room temperature. The MoS_2 sample was freshly cleaved immediately prior to introduction to the UHV chamber, and then degassed overnight at 200-300^{o}C. Imaging was conducted using electrochemically etched W tips. STM images were processed using the Gwyddion software package[112].

3.3 Results and Discussion

3.3.1 Covalent Functionalization of MoS_2 by Aryl Diazonium Salts

The covalent functionalization of pristine semiconducting 2H-MoS_2 was previously demonstrated by our group in Chu *et al.*[34]. We showed that the pristine MoS_2 surface is chemically inert, but with the addition of a single defect such as a sulfur vacancy we can initiate a chain-like propagating reaction across the surface for aryl diazonium salts leading to covalently attached chemical groups on the MoS_2 basal plane. The reaction process is illustrated in **Figure 3.1**: the 4-NBD diazonium salt approaches the MoS_2 surface in solution (**Figure 3.1a**); charge transfer from the surface causes the formation of an aryl radical and the release of a nitrogen molecule; the aryl radical forms a covalent C−S bond forms to produce MoS_2 functionalized by NP groups (**Figure 3.1b**). The spatial dependence of the reaction is schematically illustrated in **Figure 3.1c**. The region immediately surrounding an initial point defect has a higher charge density, which enables more effective charge transfer to the diazonium molecule, which then forms a radical that can readily form a covalent C-S bond with the surface. The region immediately surrounding that newly attached group also has a higher charge density, and acts as a point of increased reactivity, so that subsequent molecules attach adjacent to it. Thus, the basal plane gradually becomes functionalized in a chain-like morphology and only requires a very low concentration of initial defects as nucleation sites as illustrated in **Figure 3.1c**. In our earlier work, the covalent functionalization of MoS_2 was confirmed by x-ray photoelectron spectroscopy (XPS) and Fourier transform infrared spectroscopy (FTIR), and the reaction mechanism was supported by DFT[34].

In the following experiments, the covalent functionalization of mechanically

exfoliated flakes of atomically thin MoS_2 with 4-NBD was studied in detailed to determine the reaction kinetics so that further insights on the reaction can be obtained. Scanning probe microscopy is used here as a valuable tool to obtain detailed, spatially resolved data that relates chemical properties[114]. **Figure 3.1d** shows an atomic force microscopy (AFM) image of a bilayer (2L) MoS_2 flake exfoliated onto a 300 nm SiO_2/Si wafer substrate. This MoS_2 flake sample is atomically thin and very flat. An optical microscope image of the exfoliated MoS_2 is shown in **Figure 3.2**. Atomically resolved scanning tunneling microscopy (STM) images of a representative exfoliated MoS_2 surface with very few initial defects are shown in **Figure 3.3**.

The sample was then covalently functionalized by immersing it into an aqueous solution of 4-NBD followed by thorough rinsing by micropure water. After the functionalization reaction, small protrusions are observed on the MoS_2 flake, as shown by the AFM image in **Figure 3.1e**. This is also confirmed by the height profiles before and after the reaction as shown in **Figure 3.1**. The height of the protrusions is about 1-2 nm. This result is consistent with and similar to our previous data in Chu *et al.*[34], where we showed that these protrusions can be interpreted as the covalently attached nitrophenyl (NP) groups on the MoS_2 surface after the 4-NBD reaction. Representative Raman spectra and photoluminescence (PL) spectra before and after reaction with 4-NBD are shown in **Figure 3.2**. The spectra show that the covalently functionalized MoS_2 maintains its semiconducting nature and becomes slightly n-doped[34].

In general, the minimal change in Raman and PL spectra indicate that the MoS_2 material generally retains its crystal structure and electronic and optical properties after functionalization.

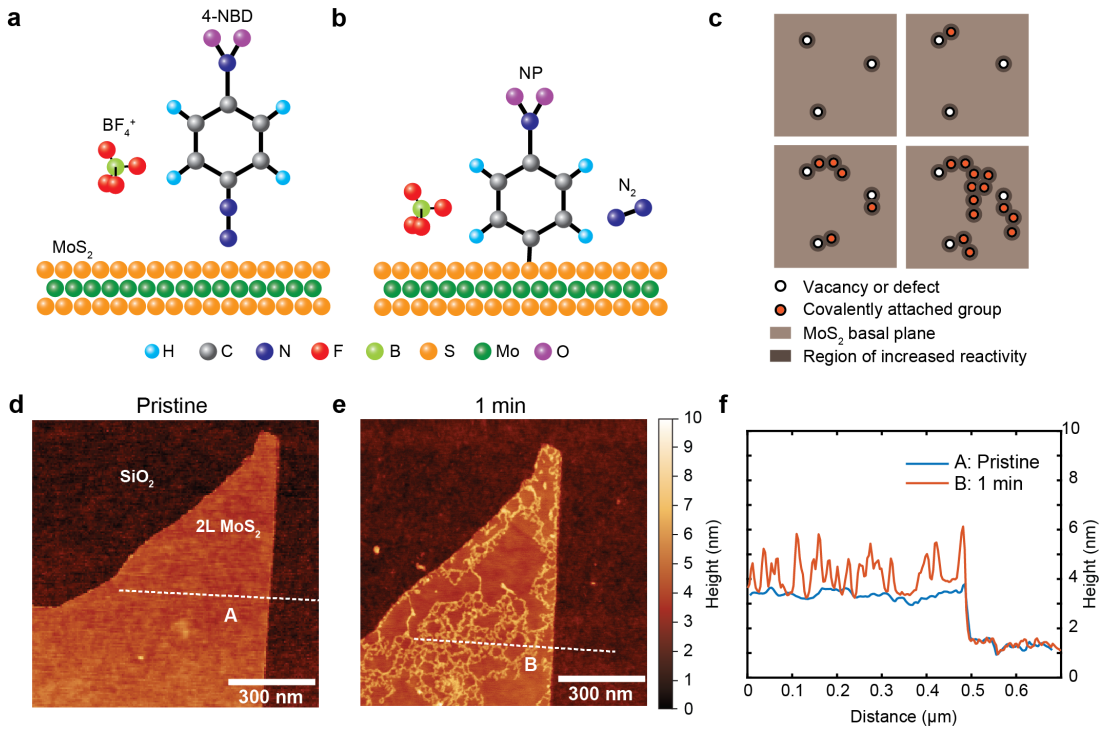

Figure 3.1: Covalent functionalization of MoS_2 using aryl diazonium salts. (a) Schematic of reaction between 4-NBD molecule and the MoS_2 sheet. (b) After the reaction, the NP group is attached to MoS_2 surface with C-S bond and N¬2 molecules are released. (c) The reaction starts from a S-vacancy and propagates across the surface in a chain-like formation due to regions of increased reactivity surrounding defects and covalently attached groups. (d) AFM image of as-exfoliated pristine bilayer MoS_2 flake on SiO_2/Si substrate. (e) The same flake shown in (d) after 1 min covalent functionalization. (f) Height profiles along the dashed lines in (d) and (e).

The Raman spectra of MoS_2 before and after functionalization were also discussed in our previous work in Chu *et al.*[34], which we will briefly summarize here. The positions and intensities of the characteristic peaks (the E^1_{2g} andA_{1g} peaks) indicate that the MoS_2 material remains semiconducting and in the same 2H phase. The LA(M) peak at around 225 cm^{-1} (which is usually associated with structural defects for MoS_2)[115] is not observed in any of our spectra. We attribute the lack of this peak to the defect concentration below the threshold where it would be strong enough to be detected. In addition, the C-S bond may not be distorting the MoS_2

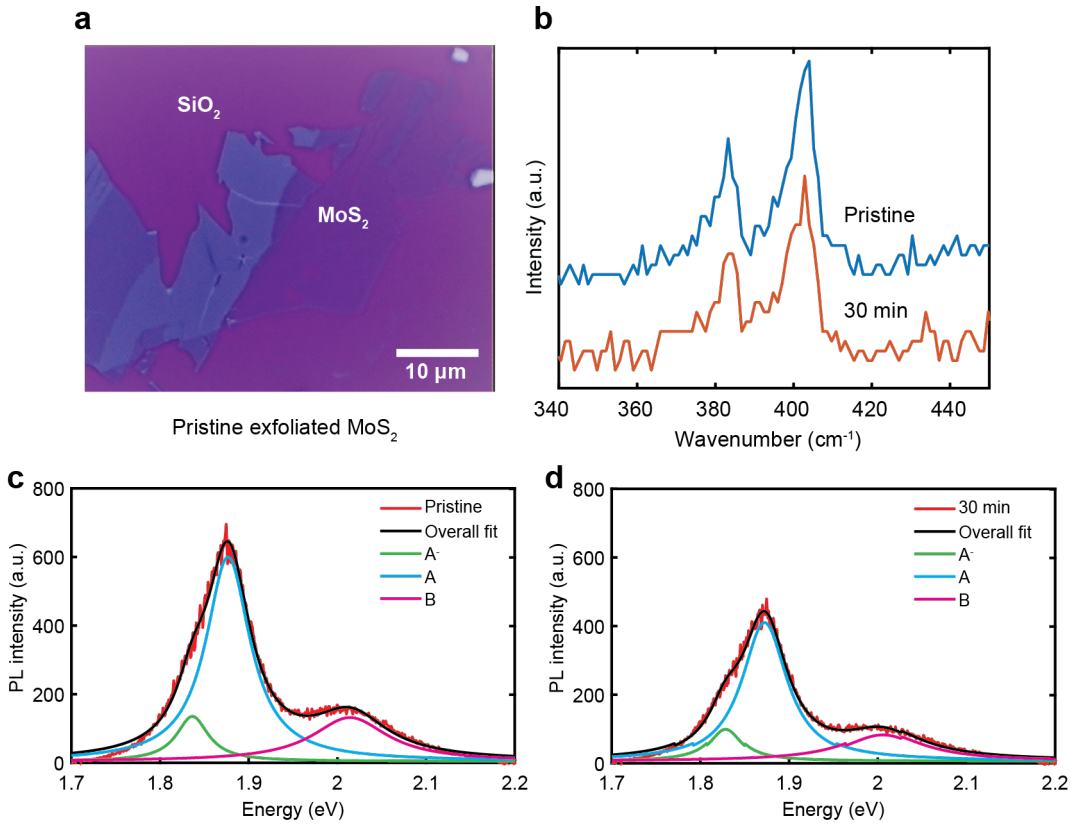

Figure 3.2: Raman and photoluminescence (PL) spectra. (a) Representative optical microscopy image of as-exfoliated MoS_2 flake from mechanical exfoliation supported on SiO_2/Si substrate. (b) Raman spectra of pristine monolayer MoS_2 and after 30 min functionalization with 4-NBD at 10 mM. (c)-(d) PL spectra of pristine monolayer MoS_2 and after 30 min functionalization, normalized to the intensities of the Raman peaks, and showing curve fitting of the A, A- and B excitons.

lattice enough to generate a significant LA(M) peak.

The PL spectrum shows a large peak at about 1.88 eV for the A exciton, and a smaller peak at about 2.02 eV for the B exciton, and there is also a smaller A- trion peak. There is a decrease of the A exciton intensity by about 35% upon functionalization. This decrease is consistent with more detailed PL measurements from our earlier work in Chu *et al.*[34] which we interpret as due to primarily n-doping upon functionalization with 4-NBD because of the electron-donating NO_2 group.

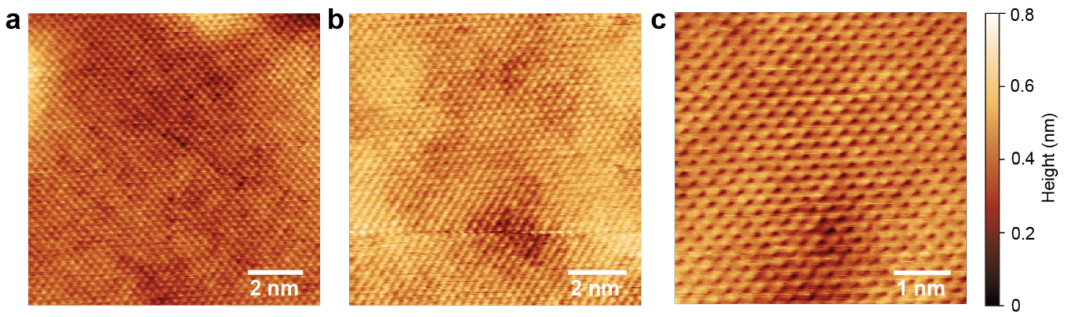

Figure 3.3: Representative scanning tunneling microscopy (STM) images of as-exfoliated pristine MoS_2 at different magnification levels. There are very few point defects in the MoS_2 surface prior to functionalization. STM imaging conditions: (a) 0.5 nA tunneling current, -1.5V applied bias; (b) 0.8 nA, -0.5 V; (c) 0.5 nA, -0.8V.

3.3.2 Concentration Dependence of Functionalization and Adsorption Isotherms

To study the covalent functionalization process as a function of the initial reactant concentration, the reaction was carried out using 4-NBD solutions at five different concentrations acting on five separate mechanically exfoliated monolayer MoS_2 samples supported by SiO_2/Si. The concentrations of the aqueous 4-NBD solutions were 1 mM, 5 mM, 10 mM, 15 mM, and 20 mM, and AFM imaging was conducted after 5 s of reaction in each of these solutions to observe the concentration and spatial distribution of covalently attached NP groups at the initial stage of reaction. As shown in **Figure 3.4a-e** protrusions formed by these NP groups were observed on MoS_2 flakes for all five concentrations, but different spatial distributions and shapes appear on each sample. Thus, it is clear that the concentration of 4-NBD in solution has a significant influence on the formation of covalent functionalization on MoS_2. AFM images of each of the MoS_2 samples before functionalization are shown in **Figure 3.5**.

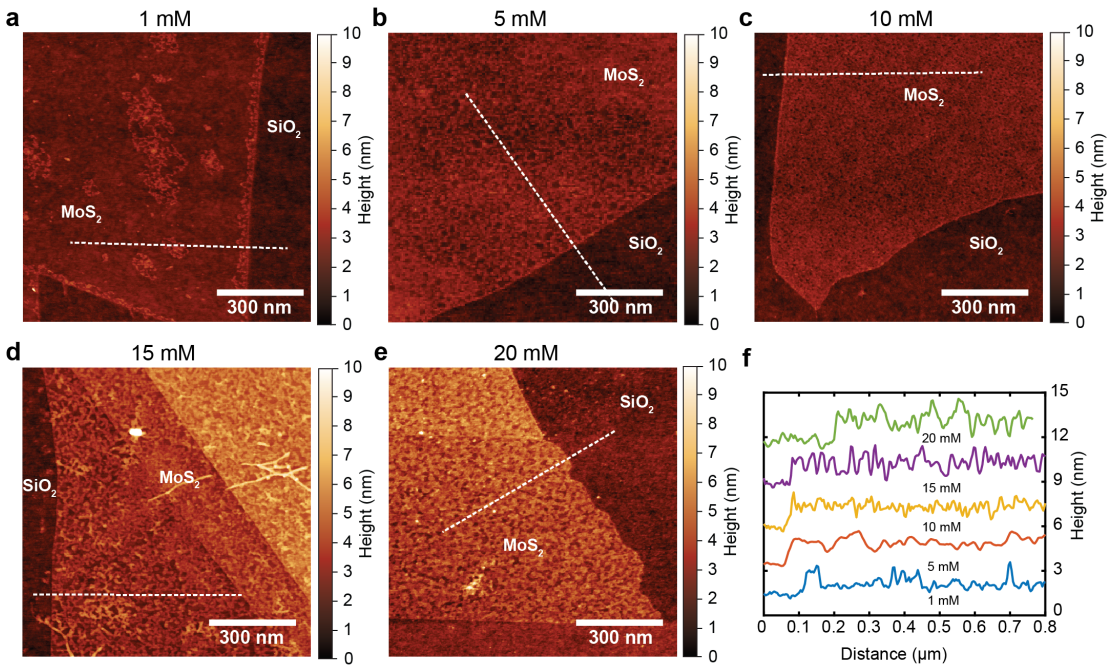

Figure 3.4: Concentration dependence of functionalization of MoS_2. (a)-(e) AFM images taken after 5 s reaction in different initial concentrations of 4-NBD solution: 1 mM, 5 mM, 10 mM, 15 mM, and 20 mM. (f) Height profiles along the dashed lines on monolayer regions in (a)-(e).

While the surface coverage of NP groups increases with increasing 4-NBD concentration, we observe also that when the concentration is as low as 1 mM in **Figure 3.4a**, the NP groups form much longer chains on the surface of MoS_2 flake. The chain-like features are also quite evident at 5 mM initial 4-NBD concentration. In Chu *et al.*[34], it was shown via AFM imaging and DFT simulations that the reaction preferentially starts from a defect or a sulfur vacancy due to the higher density of states, and then the newly attached NP group will encourage additional molecules to be attached around it (see reaction schematic in **Figure 3.1c**). Thus, at the lower 4-NBD concentration, the initiation and propagation are more evident, due to the molecules preferring to attach adjacent to existing covalently attached groups. This picture of the reaction mechanism is also expanded to include the role of edges as shown in **Figure 3.4a**, where there are more attached molecules along

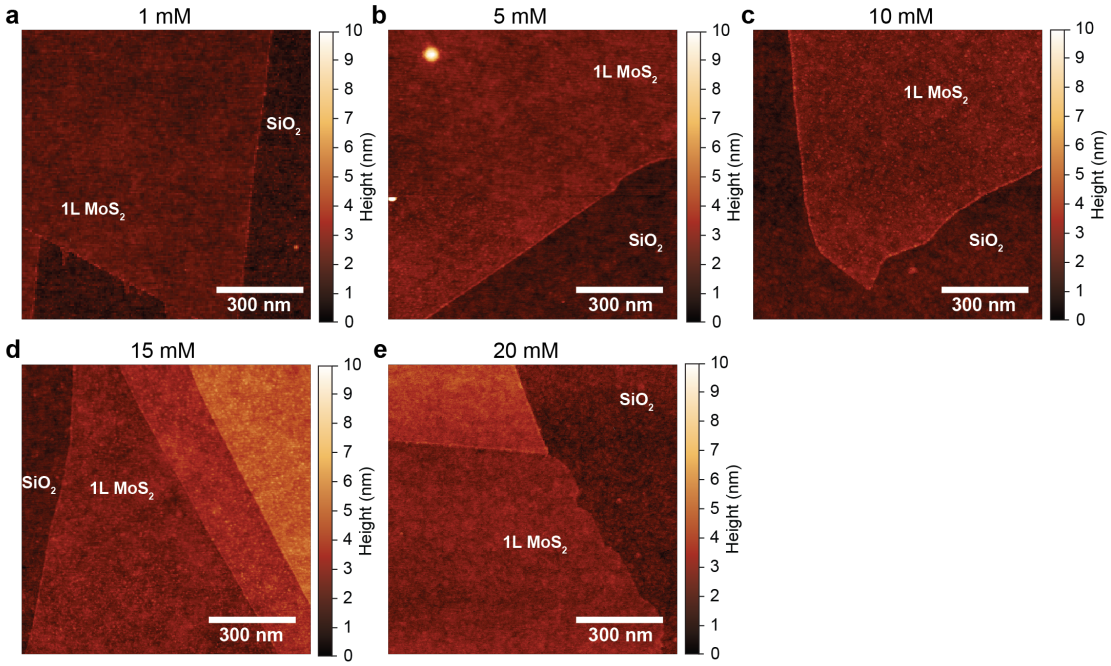

Figure 3.5: Atomic force microscopy (AFM) images of pristine MoS_2.(a)-(e) AFM images of MoS_2 samples used for isotherm study. Samples are shown here before any functionalization occurs and monolayers are labeled as "1L MoS_2". The samples are then functionalized for 5 s using 4-NBD solutions with initial concentrations of 1 mM, 5 mM, 10 mM, 15 mM and 20 mM, respectively.

the edges of the MoS_2 flake, suggesting that the charge density is higher there than in the interior of the flake. Furthermore, the inhomogeneous distribution of chains in the interior of the flake may be caused by the uneven distribution of defects or S-vacancies[116]. These observations are consistent with our previous DFT results showing that it is energetically preferable for new molecules to attach adjacent to existing defects or molecules on the surface of MoS_2[34].

With increasing 4-NBD concentration in the reaction solution, as shown in **Figure 3.4b-e**, when there are enough 4-NBD molecules to saturate all the defects in a certain area, the morphology of the attached molecules will become more and more uniform. However, when the concentration reaches as high as 20 mM, the uniformity decreases due to the piling up of NP groups, perhaps caused by the

formation of oligomers protruding from the surface, which has previously been observed for 4-NBD functionalization of graphene[117, 118]. The change in height profiles in **Figure 3.4a-e** are shown in **Figure 3.4f** and the increase in thickness due to the attached NP groups is around 2 nm.

To further advance our quantitative understanding of the mechanism of the functionalization, we performed an adsorption isotherm study by plotting the concentration of NP groups as a function of initial 4-NBD solution concentration and fitting them by three empirical adsorption models that each contain different assumptions. The Langmuir[119, 120], Freundlich[120, 121], and Temkin models[120, 121] are given in **equations 3.1, 3.2 and 3.3**, respectively:

$$\theta = \frac{K_L c}{1 + K_L c} \tag{3.1}$$

$$\theta = K_F c^{\frac{1}{n}} \tag{3.2}$$

$$\theta = \left(\frac{RT}{b}\right) ln\,(Ac) \tag{3.3}$$

In these equations, θ is the coverage of NP groups on the monolayer MoS_2 flake; c is the concentration of 4-NBD in aqueous solution; K_L and K_F are the equilibrium constants in Langmuir and Freundlich models, respectively. In the Temkin model, R is the gas constant (8.314 J mol^{-1} K^{-1}) and T is the reaction temperature (310 K); and A and b are fitting constants. In the Langmuir adsorption model, the surface of the adsorbent is assumed to be energetically homogenous so that all the adsorption sites are equivalent[119]. In contrast, the Freundlich isotherm model is a better

model to describe multi-site adsorption on inhomogeneous surfaces[119]. Since our DFT simulations in Chu *et al.*[34] demonstrated the interaction between NP groups on the MoS_2 surface during the attachment reaction, the Temkin adsorption isotherm was also chosen to fit the data since the effect of the previously attached covalent groups is considered in the model[121].

The molecular coverage of each MoS_2 sample was estimated by processing AFM images using ImageJ[34, 122]. In each AFM image, an area of covalently functionalized monolayer MoS_2 was isolated (**Figure 3.6a**) and then converted to a black and white binary image (**Figure 3.6b**). The molecular coverage was then calculated as the percentage of white pixels. We note that this estimate of coverage only accounts for the covalent surface functionalization, and does not account for any possible polymerization of the 4-NBD with molecules already on the surface that has previously been seen for graphene[117, 118]. The effect of polymerization in our experiments is much less pronounced than the laterally spreading covalent surface functionalization, as estimated by the increase in height of the AFM features with reaction time (**Figure 3.7**).

The fitting curves to the three adsorption models, the Langmuir, Freundlich, and Temkin models in **equations 3.1**, **3.2**, and **3.3** are shown in **Figure 3.6** along with their correlation coefficients (R_2 values) of 0.9610, 0.9765, and 0.9954, respectively. These fits suggest that the Temkin and Freundlich models are better descriptions of the reaction. In the Langmuir model, the surface is assumed to be energetically homogeneous. However, since the adsorption site (i.e. the covalent reaction site) is more energetically favorable when it is adjacent to either a defect or S-vacancy or previously attached molecule where there is an increase in reactivity, the surface

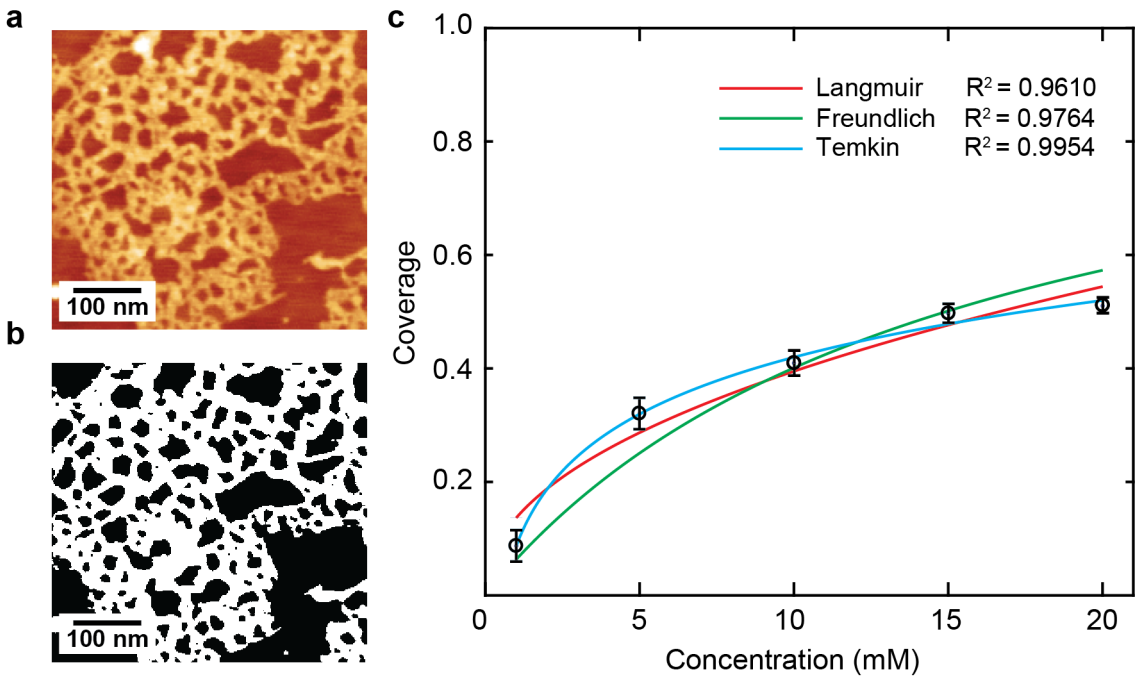

Figure 3.6: Image processing and adsorption isotherms.(a)-(e) AFM images of MoS_2. (a) AFM image of monolayer MoS_2 after functionalization. (b) Black and white image converted from (a). (c) Fitting curves of Langmuir, Freundlich, and Temkin isotherm models. The coverages were calculated from the monolayer regions in **Figure 3.4** after 5 s functionalization.

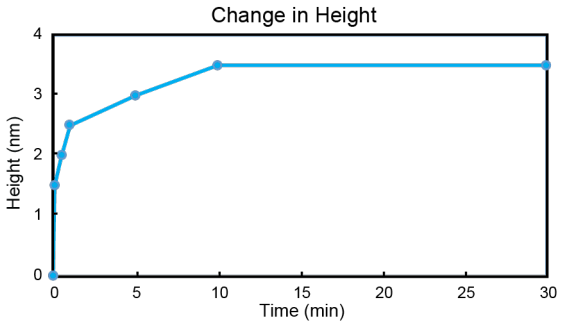

Figure 3.7: Change in height of features on MoS_2 surface as a function of reaction time from topographic data in Figure 3.10 of main text.(a)-(e) AFM images of MoS_2. The change in height is attributed to polymerization between molecules, and is much smaller and saturates at about 3.5 nm by 10 min, compared to the increase in lateral coverage due to covalent surface attachment, which continues for longer reaction times.

energies on the MoS_2 surface must change at these sites. This scenario corresponds better with the Freundlich model, which is more suitable for an inhomogeneous surface. In addition, the high correlation coefficient in the fit for the Temkin model indicates that the molecules in the solution tend to arrange themselves next to previously attached molecules, since indirect adsorbate-adsorbate interactions are taken into account in the Temkin model. In other words, the effect of previously attached NP groups are crucial to the attachment of new groups from the aqueous solution, which is consistent with our previous DFT calculation that shows the chain-like features will be formed starting from a single defect. Therefore, both the Freundlich and Temkin models can describe the reaction better than the Langmuir model, since they have higher R_2 values. Finally, we note that the observed equilibrium coverage is about 50%, which is consistent with our earlier DFT results showing that saturation occurs at about that level of coverage due to some desorption of previously attached groups at saturation[34].

3.3.3 Time Dependence of Functionalization and Morphology

The time dependence of the 4-NBD functionalization of the MoS_2 surface was studied using by taking AFM images of a sample of MoS_2 at different time points during the functionalization reaction using a 4-NBD concentration of 1 mM, as shown in **Figure 3.8**. We observe that the functionalization reaction starts from the edges and at some randomly distributed locations in the basal plane where there may be more defect sites. The molecules form long chains as they grow quickly with increasing reaction time. The reaction progress is much faster in the first 5 min, but there is still some increase in coverage with longer reaction time even though it is slower. In addition, the thin chains form islands of NP groups that grow larger with

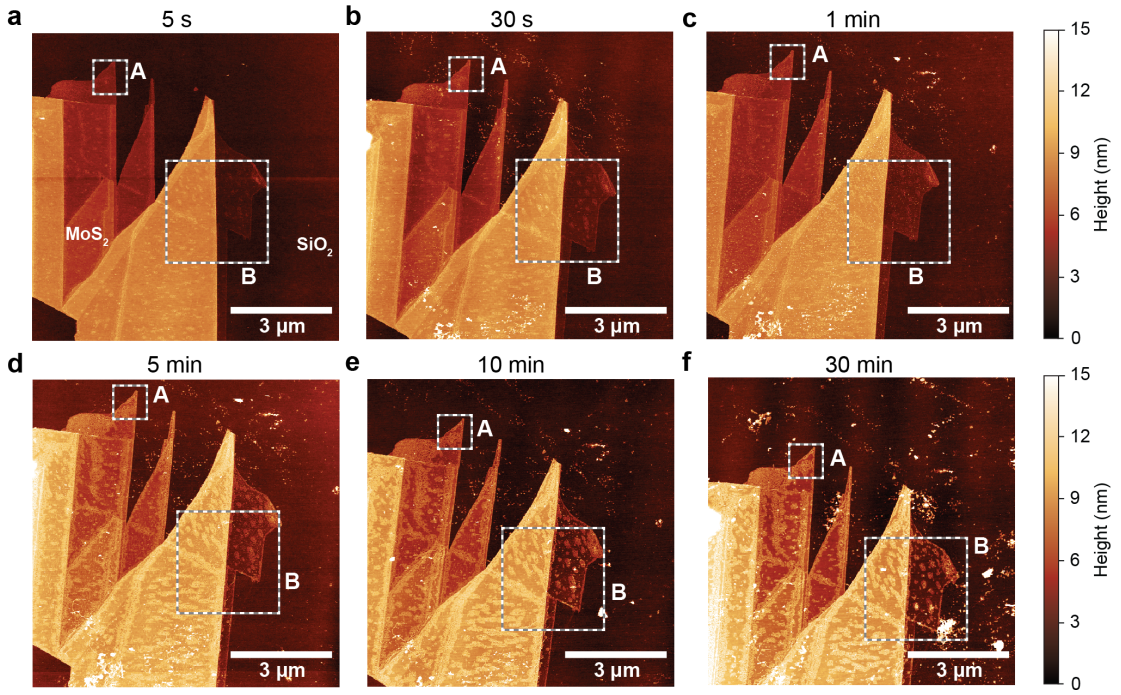

Figure 3.8: Time dependence of functionalization.(a)-(f) AFM images of monolayer MoS_2 taken after different reaction times in a 4-NBD solution of 1 mM concentration at reaction times of 5 s, 30 s, 1 min, 5 min, 10 min and 30 min. Further AFM images zooming in on the regions marked by the squares A and B are shown in Figures 2.9 and 2.10, respectively.

increasing reaction time.

The spatial inhomogeneity of the distribution of initial defects in the MoS_2 sample prepared by mechanical exfoliation[116] is also reflected in the differences in morphology upon functionalization, as illustrated in the two regions marked by the squares labeled A and B in **Figure 3.8**. In **Figure 3.9**, which shows higher resolution AFM images from region A, we observe many thin, long chains of NP groups that connect with each other. The density of defects is likely higher at the corner of the MoS_2 flake, and defects at the edges also contribute to the higher reactivity. In **Figure 3.9d** and **e**, the circled chain disappears in **Figure 3.9f**. This indicates that during the functionalization, desorption can happen in some areas.

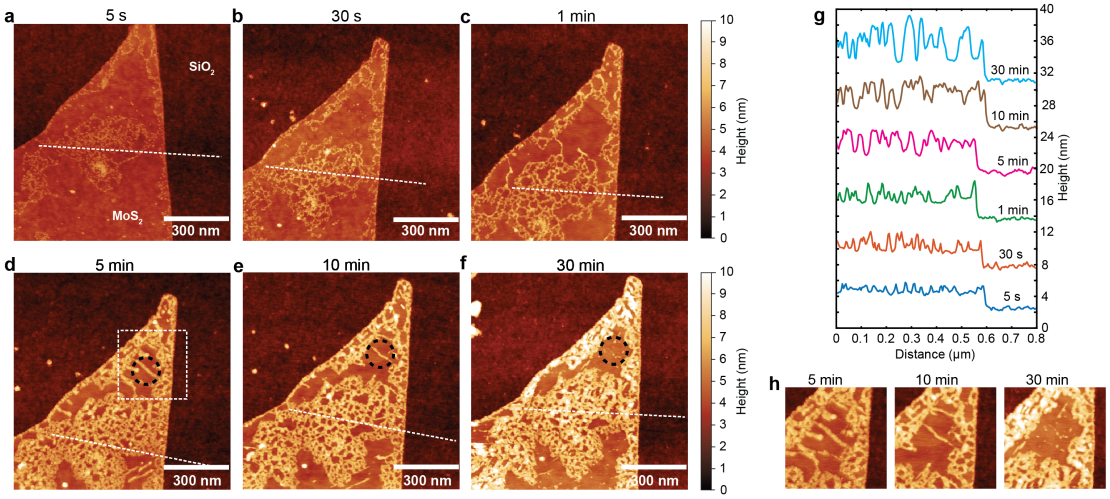

Figure 3.9: Time dependence of functionalization in the region marked by square A from Figure 3.8. (a)-(f) AFM images of MoS_2 flake shown in Figure 3.8 from the bilayer region in square A, taken after different reaction times in a 4-NBD solution of 1 mM concentration. The reaction times are 5 s, 30 s, 1 min, 5 min, 10 min and 30 min. (g) Height profiles along the dashed lines in panels (a)-(f). (h) Enlarged images from the dashed box in (d)-(f) to show the desorption of chains.

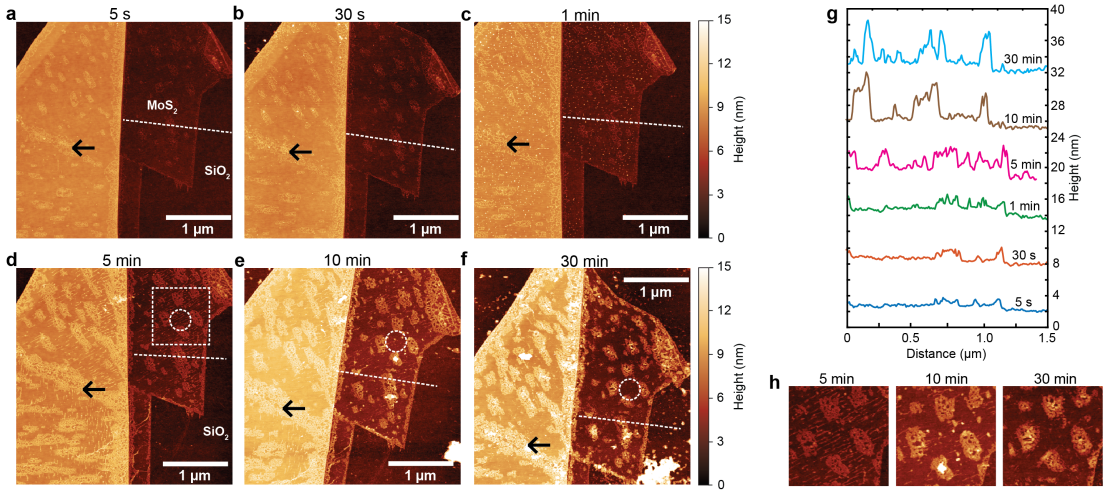

Figure 3.10: Time dependence of functionalization in region marked by square B from Figure 3.8. (a)-(f) AFM images of MoS_2 flake shown in **Figure 3.8** from the monolayer area marked by the square B, taken after different reaction times in a 4-NBD solution of 1 mM concentration. The reaction times are 5 s, 30 s, 1 min, 5 min, 10 min and 30 min. (g) Height profiles along the dashed lines in panels (a)-(f). (h) Enlarged images from the dashed box in (d)-(f) to show the desorption of chains.

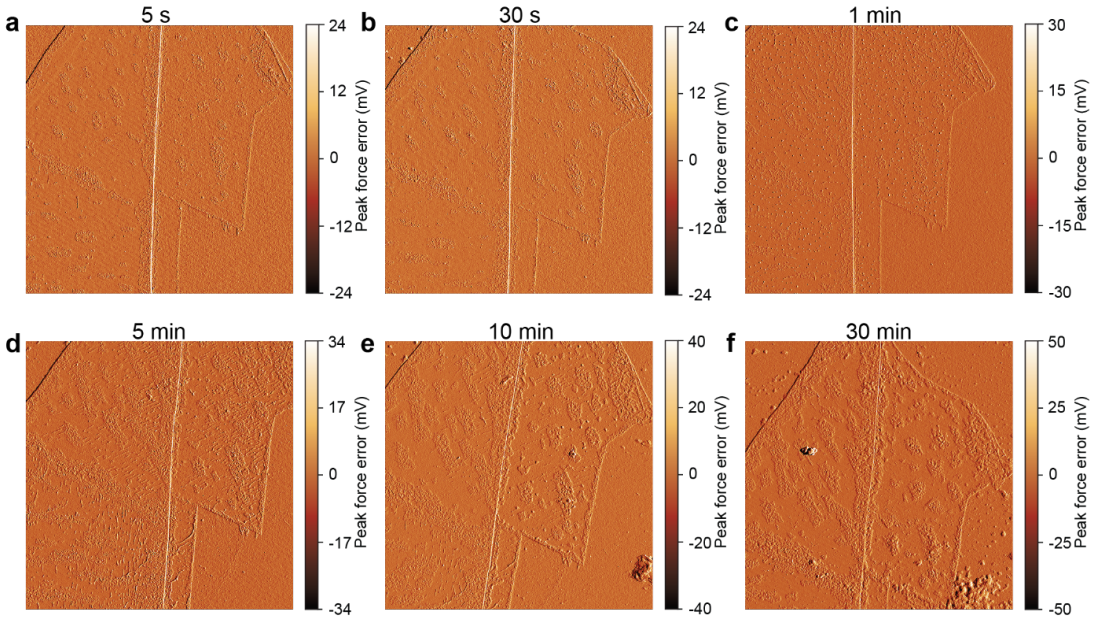

Figure 3.11: Time dependence of functionalization shown by amplitude / peak force error images, corresponding to the AFM topography images shown in **Figure 3.10** of the main text. The 4-NBD reaction times are 5 s, 30 s, 1 min, 5 min, 10 min and 30 min.

A possible explanation for this observation is that the functionalization may be a dynamic process so that some molecules will rearrange themselves on the surface to minimize the total energy. Before the equilibrium is reached, the molecules can either move back to the solution or join the molecules attached in the surrounding area. The desorption of previously attached molecules from the MoS_2 surface was also observed in our earlier DFT simulations in Chu *et al.*[34]. These regions are also enlarged in **Figure 3.9h**. As shown in the height profiles in **Figure 3.9g**, the thickness of the attached NP groups eventually increases from 1-2 nm to 6-8 nm at 30 min reaction time, which is consistent with the formation of oligomers that was previously shown for functionalization of graphene with 4-NBD[117, 118].

Next, higher resolution AFM images from the region marked by square B in **Figure 3.8** are shown in **Figure 3.10** and they exhibit a different morphology

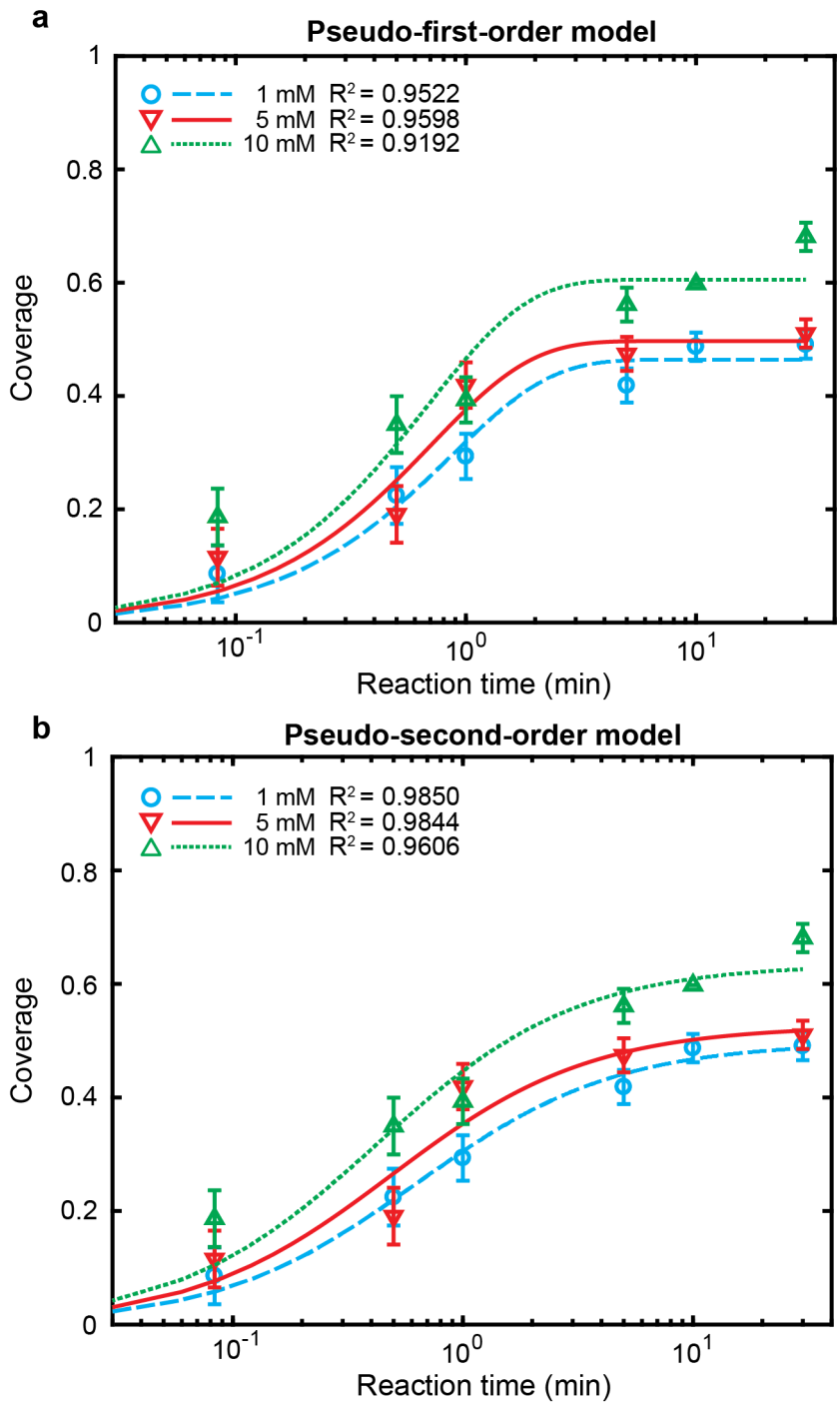

Figure 3.12: Kinetics study of covalent functionalization of monolayer MoS_2. (a) Pseudo-first-order model fit for coverage as a function of reaction time for 4-NBD concentrations of 1 mM, 5 mM and 10 mM. (b) Pseudo-second-order model fit for the same concentrations. The data sets for the fitting curves of 1 mM, 5 mM and 10 mM were calculated from monolayer regions in the samples shown in **Figure 3.10**, **Figure 3.13** and **Figure 3.14**, respectively.

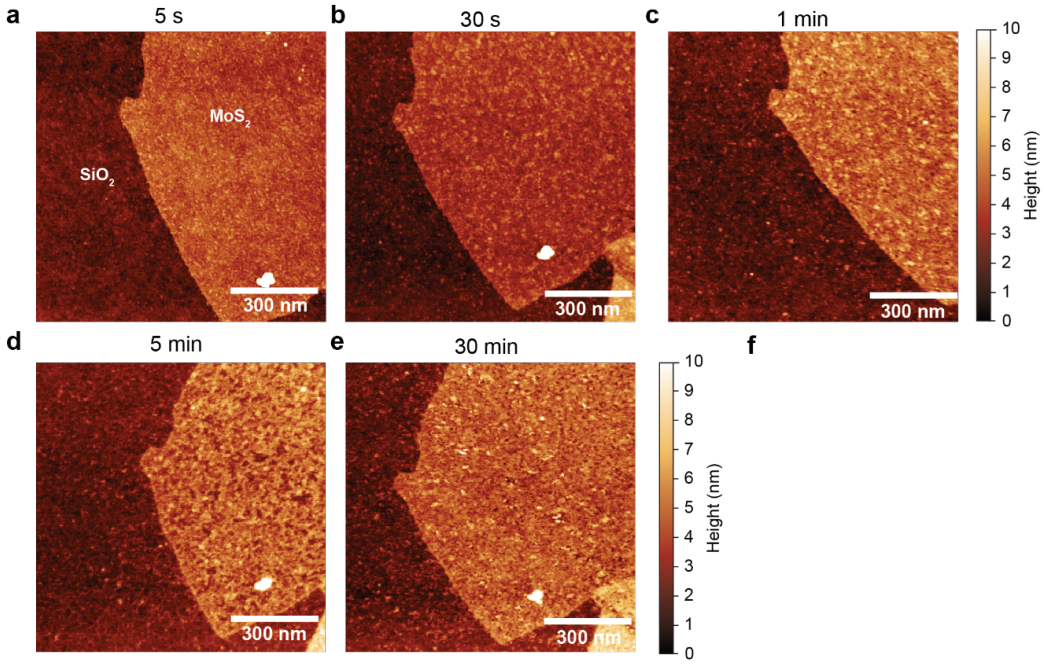

Figure 3.13: Time dependence of functionalization.(a)-(e) AFM images of monolayer MoS_2 taken after different reaction times in a 4-NBD solution of 5 mM concentration at reaction times of 5 s, 30 s, 1 min, 5 min, and 30 min.

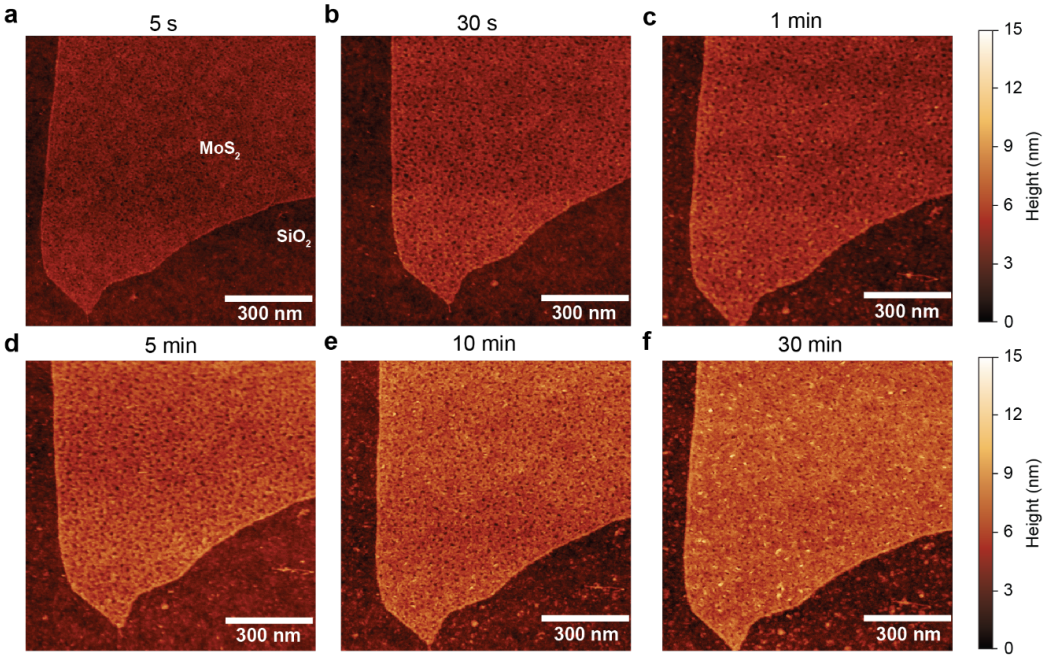

Figure 3.14: Time dependence of functionalization.(a)-(f) AFM images of monolayer MoS_2 taken after different reaction times in a 4-NBD solution of 10 mM concentration at reaction times of 5 s, 30 s, 1 min, 5 min, 10 min and 30 min.

of covalently attached NP groups. Instead of mainly thin chains, the attachment of NP groups also forms small islands that gradually grow larger. Once again, we see that some of the chains that are present at 5 min (**Figure 3.10d**) start to disappear at 10 min (**Figure 3.10e**) are missing at 30 min (**Figure 3.10f**) in the region of white circles, consistent with the simultaneous desorption process noted above for region A. These regions are also enlarged in **Figure 3.10h**. The large, long island formed in the center of the images in **Figure 3.10** (indicated by the arrow) may be due to a higher density of defects along a grain boundary, crack, or region of strain along the direction of mechanical exfoliation. The small islands of increased functionalization are also likely due to a higher local concentration of defects in those locations due to the inhomogeneous distribution of defects in mechanically exfoliated natural MoS_2[116, 123]. Similar to the results in **Figure 3.9**, here in **Figure 3.10** the height profiles show an increase from 1-2 nm to 6-7 nm with the increase of the reaction time. This also indicates that as the number of the attached NP groups increases, the adsorbate-adsorbate interaction drives the free NP groups in solution to attach to the NP groups instead of MoS_2 surface. We note that the formation of the different directions of the chains are not related to the rinsing and drying process of the sample at each reaction time step, since different directions are used for the water and nitrogen flows that are not consistent with the observed chain directions. Finally, simultaneously obtained amplitude / peak force error images corresponding to the images in **Figure 3.10** and **Figure 3.11**, where the topographic changes due to functionalization are also visible.

3.3.4 Reaction Kinetics of Functionalization

The kinetics of the 4-NBD functionalization of MoS_2 was analyzed for three MoS_2 samples functionalized in 4-NBD solutions of three different concentrations (1, 5, and 10 mM) by taking AFM images at different reaction times (5 s, 30 s, 1 min, 5 min, 10 min, and 30 min). We fit the time- and concentration-dependent coverage data to pseudo-first-order and pseudo-second-order kinetic models, using **equations 3.4** and **3.5**[120, 124, 125], respectively:

$$ln\left(\theta_e - \theta\right) = ln\left(\theta_e\right) - k_1 t \tag{3.4}$$

$$\frac{t}{\theta} = \frac{1}{k_2 {\theta_e}^2} + \frac{1}{\theta_e} t \tag{3.5}$$

In these equations, θ is the coverage of NP groups on the monolayer MoS_2 flake, θ_e is the coverage at equilibrium, t is the reaction time, and k_1 and k_2 are the rate constants that are used as fitting parameters. The same process for obtaining surface coverage from AFM images that we used for the isotherms was used here. The coverage as a function of reaction time for the three 4-NBD solution concentrations (1, 5, and 10 mM) along with the pseudo-first-order and pseudo-second-order kinetic fits are shown in **Figure 3.12**. The coverage of molecules on the MoS_2 surface increases rapidly in the first 5 mins, and then slows down. With increasing concentration, there is an increase at the final coverage at 30 min, consistent with the increase of coverage with increasing concentrations that we first observed from the adsorption isotherm study.

The pseudo-second-order model results in higher correlation coefficients (R_2

values) than the pseudo-first-order model for all three 4-NBD concentrations, indicating that the order of this reaction is two. In this model, the 4-NBD molecules in solution are the reactants in excess, and the molecularity of this reaction is greater than two. In other words, there is interaction between 4-NBD molecules during the reaction, which is also consistent with the fitting of the Temkin adsorption isotherm model. In our earlier DFT simulation results in Chu *et al.*[34], we showed that there is a subtle balance between adsorbate-adsorbate and adsorbate-surface interactions so that there is a limit of coverage at 50% with some fraction of molecules also desorbing. However, the observed maximum saturation coverage of 10 mM 4-NBD concentration shown in **Figure 3.12** is higher than 60% (closer to 68%) which may be attributed a a broadening of features due to the AFM tip radius so that each molecule may appear larger and thus resulting in a higher apparent coverage. In addition, the larger clusters appearing at the bottom right corners in **Figure 3.10e** and **f** tend to blunt the AFM tip and increase the tip-broadening effect.

Overall, with the increase of 4-NBD solution concentration, the reaction is accelerated. The process is controlled by both adsorbate-surface and adsorbate-adsorbate interactions. At the beginning of the reaction, the adsorbate-surface interaction is dominant so that the coverage increases rapidly. With the number of attached NP groups increasing, the effect of adsorbate-adsorbate interaction increases and the increase of the coverage slows down. Eventually the balance between adsorbate-adsorbate and adsorbate-surface interaction is achieved and the coverage is saturated.

3.4 Summary and Conclusions

In conclusion, we have conducted a detailed study of the reaction kinetics and reaction mechanism for the covalent functionalization of two-dimensional layers of semiconducting 2H-MoS_2 by the aryl diazonium salt 4-NBD. Our findings here confirm and expand on the reaction model put forth in our earlier work in Chu *et al.*[34]. The adsorption study at different 4-NBD concentrations found that both the Freundlich and Temkin isotherm models are a better description of the reaction because the surface of MoS_2 is not energetically homogeneous and indirect adsorbate-adsorbate interactions from the previously attached NP groups are taken into consideration. Various morphologies and spatial distributions of the covalently attached molecules are found due to the interaction between 4-NBD molecules and the inhomogeneous distribution of defects in the MoS_2 layer. The reaction kinetics was better described using a pseudo-second order model, showing that the order of this reaction is two, thus further confirming the interaction between 4-NBD molecules. This detailed understanding of the functionalization of MoS_2 may have implications for future applications in electronics, environmental remediation, sensing, and energy.

Chapter 4

COVALENT CHEMICAL FUNCTIONALIZATION OF SEMICONDUCTING LAYERED CHALCOGENIDE NANOSHEETS

Layered chalcogenides are a diverse class of crystalline materials that consist of various covalently bound building blocks held together by van der Waals forces. Among these materials are the transition metal dichalcogenides (TMDCs) which can be exfoliated into two-dimensional (2D) nanosheets, and the pnictogen chalcogenides (PCs) which can be exfoliated into one-dimensional (1D) nanoribbons and 2D nanosheets. These materials have recently been extensively studied for their intriguing electronic, optical, and chemical properties. The chemical functionalization of 1D and 2D nanomaterials is an important enabling step for tuning their properties and forming interfaces with other materials and structures. However, broadly applicable and versatile chemical tools that can effectively functionalize a wide range of layered chalcogenide compositions without disruptive pre-treatments need further advancement.

In this chapter, we show the covalent functionalization of nanosheets of the representative TMDC materials MoS_2, WS_2, $MoSe_2$, and WSe_2, and of the representative PC materials Sb_2S_3 and Bi_2S_3 using aryl diazonium salts. Covalent bonds are formed on the basal planes of both mechanically exfoliated and liquid phase dispersed nanosheets, and the chemical and morphological changes upon functionalization are verified using a combination of spectroscopic and microscopic techniques. This work builds on previous demonstrations of diazonium functionalization of 2D materials like MoS_2, and expands it to five additional compositions. Thus, the aryl

diazonium chemistry is shown to be a versatile and powerful approach to covalent functionalization of the 2D nanosheets of a diverse set of semiconducting layered chalcogenide materials.

4.1 Experimental Methods

4.1.1 Materials

Tungsten (IV) sulfide (WS_2, powder, 99%, 2 μm), molybdenum (IV) selenide ($MoSe_2$, 325 mesh, 99.9% trace metals basis), molybdenum(IV) sulfide (MoS_2, powder), bismuth (III) sulfide (Bi_2S_3, 99%), antimony (III) sulfide (Sb_2S_3, powder), 4-nitrobenzenediazonium tetrafluoroborate (4-NBD, 97%), sodium dodecyl sulfate (SDS, BioReagent, suitable for electrophoresis, for molecular biology, 98.5% GC), molybdenum (VI) oxide (MoO_3), and selenium (Se powder) were purchased from Sigma-Aldrich. Tungsten (IV) selenide (WSe_2, 10-20 μm powder, 99.8% metals basis) and sulfur (S powder) were purchased from Alfa Aesar. Single crystals of MoS_2 and WS_2 were purchased from SPI Supplies, $MoSe_2$ from MTI Corporation, and WSe_2 from Nanosurf.

4.1.2 Mechanical Exfoliation

Si/SiO_2 (300 nm) substrates were ultrasonically cleaned in acetone and isopropanol baths sequentially and then blown dry with ultrahigh purity nitrogen gas. The TMDC flakes were prepared by mechanical exfoliation from single crystals, while the PC flakes were prepared by using the same method from bulk powders.

4.1.3 Liquid Phase Exfoliation

Liquid exfoliation for TMDCs and PCs used bulk powder source materials mixed in 1% wt/vol SDS aqueous solutions and subjected to tip sonication (Branson Digital Sonifier 450D) with a 3 mm tip for 2-4 hours at 30-50% amplitude. The mixtures were then centrifuged for 5-30 min at 3234 to 5000 RCF and the supernatant containing the dispersed nanosheets were extracted and used for further experiments. The masses, sonication times and amplitudes, and centrifugation times and speeds for each material are as follows: MoS_2 according to methods in Chu *et al.*[34]; WS_2: 5 g in 110 mL SDS solution, 2 hours at 50% amplitude, 30 minutes at 3234 RCF; $MoSe_2$ and WSe_2: 0.65 g in 20 mL SDS solution, 2 hours at 30% amplitude; Bi_2S_3 and Sb_2S_3: 1.3 g each in 20 mL SDS solution, 4 hours at 35% amplitude, 5 minutes at 5000 RCF.

4.1.4 Functionalization of Mechanically Exfoliated Samples

The mechanically exfoliated flakes of TMDCs and PCs deposited on Si/SiO_2 were immersed in 10 mM of 4-nitrobenzenediazonium tetrafluoroborate (4-NBD) (Sigma Aldrich) aqueous solutions at 35 °C with stirring at 125 rpm. The reaction was conducted in a beaker sealed by parafilm in the dark. Then the samples were removed from the solution and thoroughly rinsed with ultrapure water and blown dry with ultrahigh purity nitrogen gas.

4.1.5 Functionalization of Liquid Phase Exfoliated Samples

Nanosheet dispersions of each material were mixed with 4-NBD powder such that the concentration of 4-NBD was 0.25% wt/vol with respect to the nanosheet

dispersion volumes. The mixtures were then subjected to tip sonication at 20% amplitude for 2 hours for MoS_2, WS_2, $MoSe_2$, and WSe_2 and for 4 hours for Bi_2S_3 and Sb_2S_3. Control samples were prepared by subjecting the nanosheet dispersions to the same sonication treatment but without any 4-NBD.

4.1.6 Raman Spectroscopy

Raman spectroscopy and optical microscopy of mechanically exfoliated nanosheets of TMDCs and PCs were obtained on a WITec alpha300R system confocal Raman microscope system with a 532 nm excitation laser and 100X objective lens with 1 μm laser spot size. The laser power was kept below 1 mW to minimize damage to the samples. Spectra were obtained using the 1800 g/mm grating and 5 s acquisition time.

4.1.7 Atomic Force Microscopy (AFM)

AFM images of mechanically exfoliated nanosheets were taken after different reaction times using a Multimode V system (Bruker Inc.) in ScanAsyst mode with ScanAsyst-Air tips (tip diameter 2 nm). AFM images were processed using Gwyddion[112].

4.1.8 Fourier Transform Infrared Spectroscopy (FTIR)

Nanosheet dispersions of all the TMDCs and PCs in both functionalized and unfunctionalized states were used to make thin films by vacuum filtration onto hydrophilic PTFE membranes (0.1 μm pore size, OMNIPORE, from Millipore) followed by washing with water and vacuum drying between 60 and 90 °C overnight

in a vacuum oven. Transmittance FTIR measurements were performed on the vacuum filtered films using a Nicolet 6700 FTIR with 64 scans taken for each sample and 128 scans taken for a background measurement in air. Within the OMNIC software used to collect the spectra, transmittance measurements were converted to absorbance measurements and a baseline correction was applied to each spectrum. The absorbance spectra were then normalized to a peak corresponding to PTFE that occurs at around 1150 cm^{-1} and plotted using MATLAB.

4.1.9 UV-Vis Absorbance Spectroscopy (UV-Vis)

Nanosheet dispersions were added to plastic cuvettes and their absorbance spectra were measured using a Jasco V-670 Spectrophotometer with 1% SDS solution as a baseline and reference. All dispersions and solutions were measured in plastic cuvettes.

4.1.10 Transmission Electron Microscopy (TEM)

Nanosheet dispersions were dropped onto 400 mesh Cu lacey carbon grids (01824 from Ted Pella) and imaged using a Philips CM 12 TEM operating at 80 kV.

4.1.11 Chemical Vapor Deposition (CVD)

The MoS_2 and $MoSe_2$ samples for XPS analysis were prepared using chemical vapor deposition (CVD) growth in a 1-inch quartz tube in a tube furnace (ThermoFisher Scientific). The target substrates were SiO_2/Si wafers held above the MoO_3 precursors. During the growth of MoS_2, 20 mg of MoO_3 was heated up to

650 ºC in 40 min and held for 30 min. 100 mg of S (Alfa Aesar) was separately heated up to 150ºC at an upstream location. The system was in vacuum with a 300 sccm of Ar flow. During the growth of $MoSe_2$, the growth was conducted in atmospheric pressure. The system was purged with a 500 sccm of Ar flow for 30 min before heating. 30 mg of MoO_3 was heated up to 150 ºC and held for 30 min followed by heating up to 950 ºC in 15 min and holding for 10 min. 200 mg of Se (Sigma-Aldrich) was separately heated up to 200 ºC at an upstream location.

4.1.12 X-ray Photoelectron Spectroscopy (XPS)

XPS analysis was conducted using a Vacuum Generators 220i-XL system with monochromated Al Kα radiation (hν = 1486.6 eV). The pressure in the analysis chamber was 10-9 torr or lower and the X-ray spot size was 400 μm. The spectra were analyzed using the CasaXPS software package.

4.2 Results and Discussion

4.2.1 Chemical Functionalization by Aryl Diazonium Salts

The 2D nanosheets of TMDCs and PCs were prepared by mechanical exfoliation onto SiO_2/Si wafer substrates, by liquid phase exfoliation in aqueous surfactant solutions by tip sonication from powders, and by chemical vapor deposition (CVD) (see section 4.1 for more details). The nanosheets were then covalently functionalized in aqueous solutions of the aryl diazonium salt 4-nitrobenzenediazonium tetrafluoroborate (4-NBD). This molecule, along with other similar derivatives, has been previously used to functionalize graphene[41, 42] and MoS_2[34, 126]. By

choosing a molecule that has been used before, we can more directly compare the results for different substrate nanomaterials without concern over variables in reactivity or morphology that may occur in different diazonium derivatives[118]. The functionalization reaction proceeds as illustrated in the steps in **Figure 4.1e-g**, resulting in covalent C-S and C-Se bonds on the basal planes with nitrophenyl (NP) groups protruding from the surface. This reaction for MoS_2 alone was studied in greater detail in our previous work in Chu *et al.*[34] and Li *et al.*[126], which confirmed the reaction mechanism and kinetics. Briefly, the reaction involves the transfer of charge from the target substrate material (MoS_2 in the case of the earlier work, and other TMDCs and PCs in the present work) to the aryl diazonium group, which forms an aryl radical upon loss of a nitrogen molecule, which then forms a covalent bond with the basal plane. Our earlier work showed that the reaction mechanism relies on the presence of a very small concentration of sulfur vacancies in MoS_2 at which the local charge density is increased in order to initiate the reaction, which then progresses across the surface in a chain-like morphology due to the increased reactivity surrounding covalently functionalized sites[34]. Thus, only a very low number of initial defects was needed for the entire basal plane to be functionalized.

The mechanically exfoliated samples in the current study enabled careful imaging by AFM to observe the formation of covalently attached chemical groups on the nanosheets' surfaces with high spatial resolution, while the liquid phase exfoliated materials provided larger quantities of nanosheets that were suitable for ensemble measurements. Both types of samples and measurements are important for characterizing the overall functionalization of this collection of TMDC and PC layered materials.

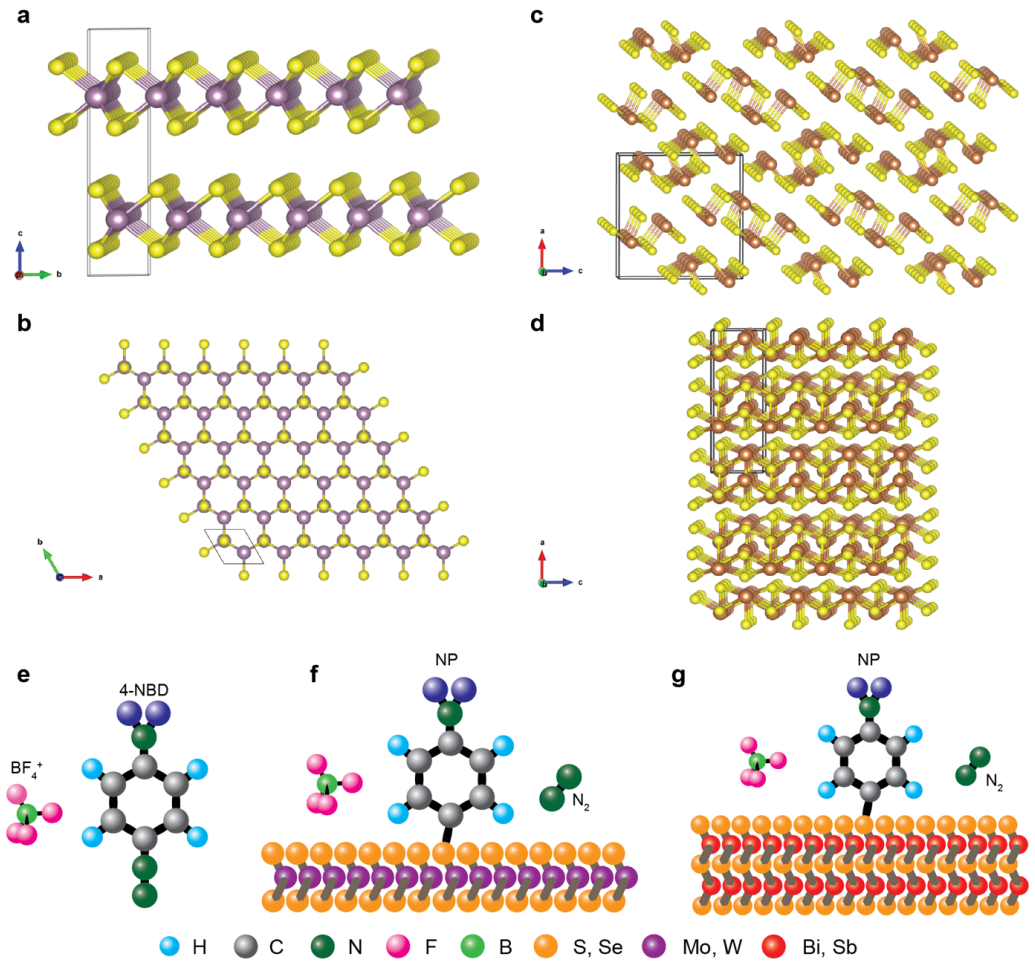

Figure 4.1: Layered chalcogenide materials and diazonium functionalization scheme. (a)-(b) Crystal structure of MX_2 materials in side and top views (yellow atoms: X; purple atoms: M). (c)-(d) Crystal structures of Pn_2X_3 materials in side and top views (yellow atoms: X; brown atoms: Pc). (e)-(g) Reaction scheme for covalent functionalization with aryl diazonium salts: (e) the functionalization is done using 4-nitrobenzenediazonium tetrafluoroborate (4-NBD), which forms a radical upon charge transfer from the substrate; the radical forms a covalent bond with the S or Se atom at the surface; and (f)-(g) there is a covalently bonded nitrophenyl (NP) group on the surface as a result.

4.2.2 Spectral Evidence of Chemical Functionalization

Optical spectroscopy was used to characterize the functionalized and unfunctionalized TMDC and PC materials. For Fourier transform infrared spectroscopy (FTIR), films of nanosheets dispersed by liquid phase exfoliation were formed by vacuum filtration onto PTFE membranes (see Experimental section for more details). For and UV-visible absorbance spectroscopy, the nanosheet dispersions were directly measured in their liquid state. For Raman spectroscopy, mechanically exfoliated flakes were used.

The FTIR results for the TMDCs are shown in **Figure 4.2a**. The spectra for all the functionalized nanosheets show features around 1344 cm^{-1} and 1514 cm^{-1} corresponding to the N-O stretching modes, which indicates the presence of the NO_2 group from 4-NBD. There is also a peak at 1600 cm^{-1} which can be associated with the C=C stretch within the benzene group of an attached nitrophenyl group resulting from the 4-NBD molecule. There is also a peak at 697 cm^{-1} corresponding to the C-S bond, although it is less prominent in some of the materials, possibly due to variations in film thickness. The C-Se bond is expected to occur at about 640 cm^{-1}[103, 104], but that is a busy part of the spectrum for $MoSe_2$, and is too weak to be clear for WSe_2 (although the N-O peaks are also weak in WSe_2). The FTIR spectra for the PCs are shown in **Figure 4.2b**. The same peaks for N-O stretching modes and the C=C stretch can clearly be seen in the 4-NBD treated PC samples, which also suggests the successful functionalization of PC materials. The presence of the C-S peak also indicates formation of covalent bonds on the PC surfaces. All these relevant peaks indicating successful functionalization are indicated by arrows.

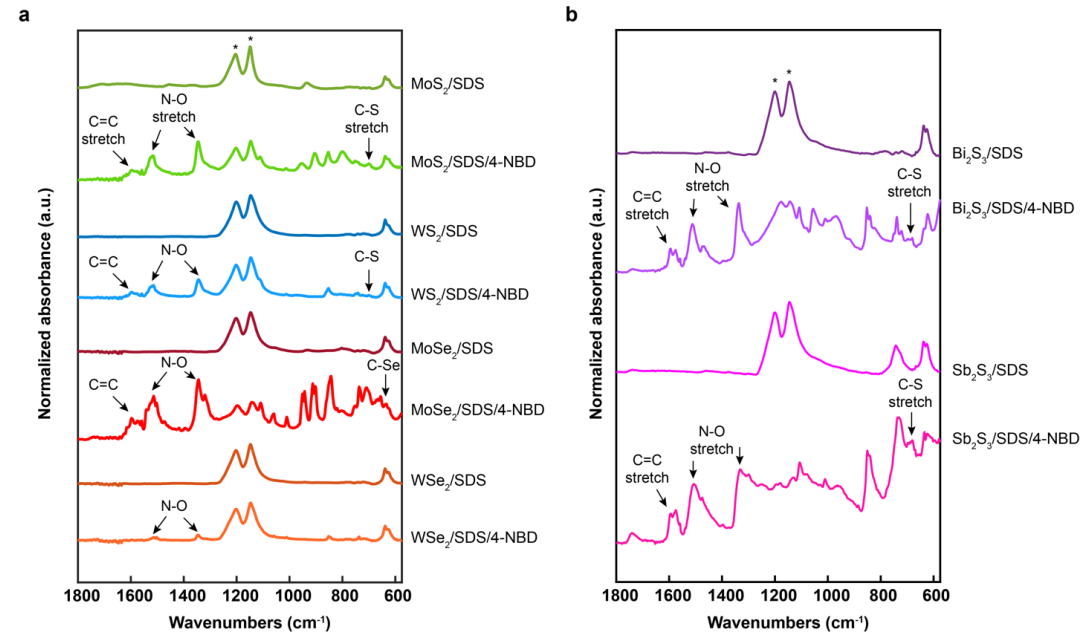

Figure 4.2: Vibrational spectroscopy for functionalized TMDCs and PCs from Fourier transform infrared spectroscopy (FTIR). Spectra for untreated and 4-NBD treated materials show a primary difference in the presence of an N-O stretch and C=C stretch in the treated samples, suggesting the presence of NO_2 and benzene groups and therefore a successful functionalization. The C-S and C-Se peaks associated with forming bonds at the surfaces of TMDCs and PCs are also present. The important peaks are indicated with arrows in the spectra for all the functionalized materials. The peaks from the PTFE support are indicated by asterisks (*).

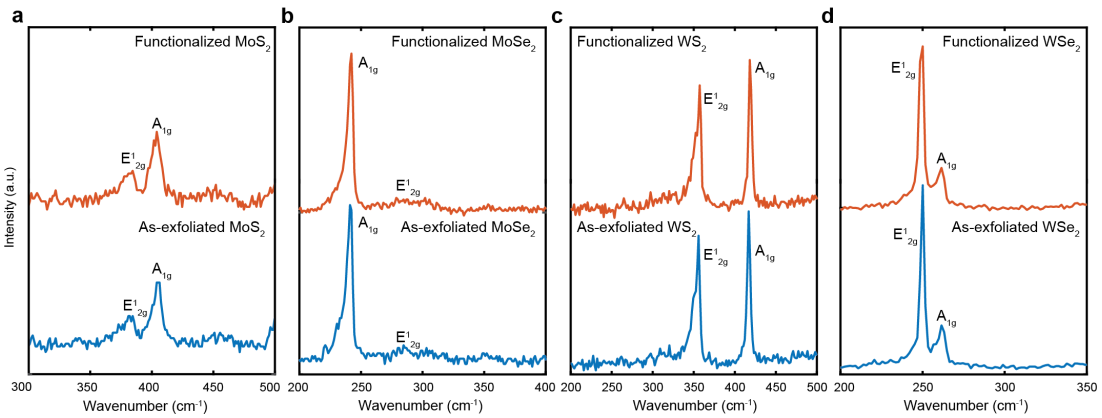

Figure 4.3: Representative Raman spectra of TMDCs as-exfoliated (lower blue traces) and after diazonium functionalization (upper red traces) for (a) MoS_2, (b) $MoSe_2$, (c) WS_2, and (d) WSe_2.

Raman spectroscopy was conducted to verify that no significant structural change or damage occurs due to the 4-NBD functionalization reaction. Nanoflakes of TMDCs and PCs were prepared by mechanical exfoliation from bulk crystals and bulk powders, respectively, and deposited onto SiO_2/Si wafers, and identified with the optical microscope in the Raman system. As shown in **Figure 4.3** of the Electronic Supporting Information, the E^1_{2g} in-plane and A_{1g} intra-plane vibrations are detected both before and after functionalization, with no significant changes. The PC materials behave similarly, as shown in **Figure 4.4**, with the characteristic vibrations indicated. This finding is important because it shows that the covalent attachment enables chemical modification to be conducted on the outer basal plane without significant disruption of the basic crystal structure of these materials.

Optical absorbance spectroscopy (UV-Vis) was conducted to characterize the changes to the excitonic structure of the TMDC and PC materials. Samples were prepared by diluting dispersions of the nanosheets with 1% SDS solution so that their absorbance values were within the instrument's detection range (see Experimental section for more details). The UV-Vis spectra for the TMDCs in **Figure 4.5a** show the characteristic excitonic peaks for MoS_2, WS2, MoSe2 and WSe2 marked with asterisks. After 4-NBD functionalization, there is a slight red shift in these peaks, similar to our observations for MoS_2 in our previous work[34]. We attributed these shifts to the electronic coupling of excitons to the aromatic groups that are attached to the TMDC surfaces, which is similar to the excitonic redshift in functionalized CdSe quantum dots[118], rather than due to an increase in layer thickness[57], because the surface functionalization prevents proper restacking. The UV-Vis spectra for PCs in **Figure 4.5b** are essentially featureless before and after functionalization, as there are no excitonic peaks in this range, but there is some

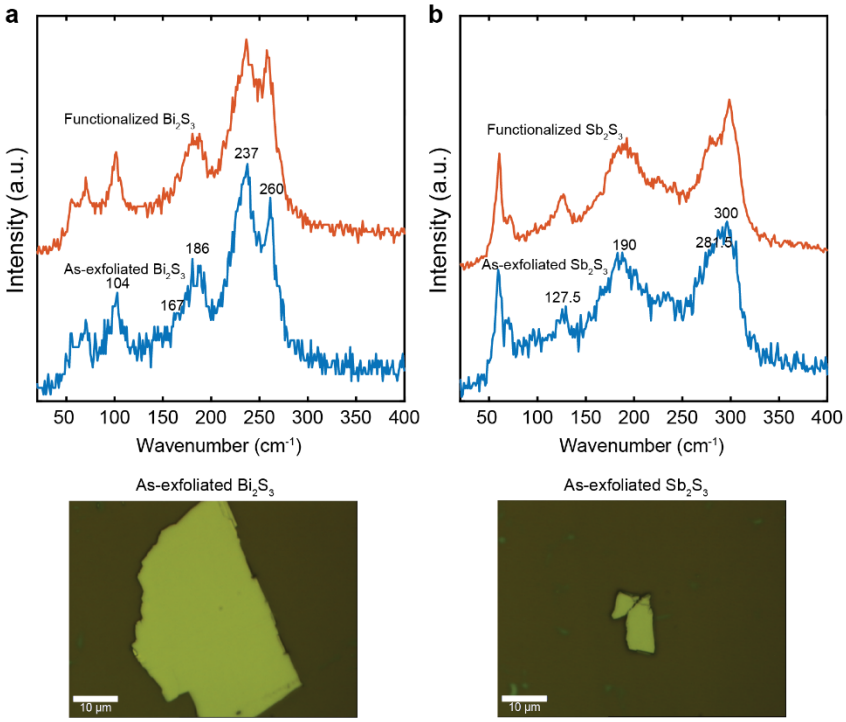

Figure 4.4: Representative Raman spectra for as-exfoliated (lower blue traces) and after diazonium functionalization (upper red traces) for (a) Bi_2S_3 and (b) Sb_2S_3. Optical microscope images for the as-exfoliated flakes on SiO_2/Si wafers are shown below the spectra.

increase in the background below 500 nm due to absorbance of the 4-NBD for the functionalized materials.

X-ray photoelectron spectroscopy (XPS) was conducted for $MoSe_2$ and MoS_2 to characterize the surface chemistry, as shown in **Figure 4.6** of the Electronic Supporting Information. After treating the samples with 4-NBD, clear N-O and N-C peaks due to the NO_2 groups appear and the intensities of the C peaks due to the benzene ring also increase, all indicative of successful functionalization with nitrophenyl groups. These changes in peaks are only known to appear when there is successful covalent functionalization with a molecule containing the diazonium-group, and are not seen for physisorption with the non-diazonium nitrobenzene molecule[34, 127].

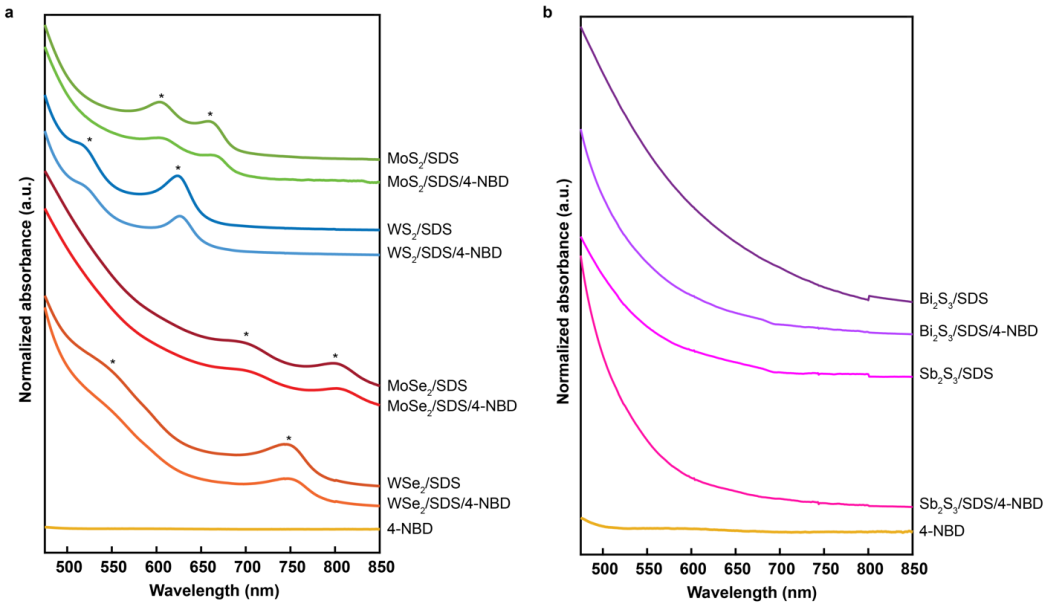

Figure 4.5: Absorbance spectroscopy for functionalized TMDCs and PCs. UV-Vis spectra are shown vertically offset for (a) TMDCs and (b) PCs as-dispersed in SDS and with 4-NBD functionalization. The reference spectrum for 4-NBD is also shown in each panel. Asterisks (*) denote exciton peaks for TMDCs, which are slightly red-shifted after 4-NBD functionalization. The PC spectra are relatively featureless.

X-ray photoelectron spectroscopy (XPS) was used to characterize the chemical bonding on large area samples of MoS_2 and $MoSe_2$ grown on SiO_2/Si substrates using chemical vapor deposition (CVD), both before and after the diazonium functionalization. Large-area CVD samples are needed for XPS to accommodate the large x-ray spot size, so mechanically exfoliated flakes were not suitable. MoS_2 and $MoSe_2$ were chosen as representative sulfide and selenide materials for which we could reliably produce high quality large-area CVD samples.

The XPS spectra are shown in **Figure 4.6**. The wide scans are shown in **Figure 4.6a** and **b**. In the N 1s region in panel (c), there was no clear N peak in the spectra of as-grown MoS_2 and $MoSe_2$. After the functionalization with 4-NBD for 30 min,

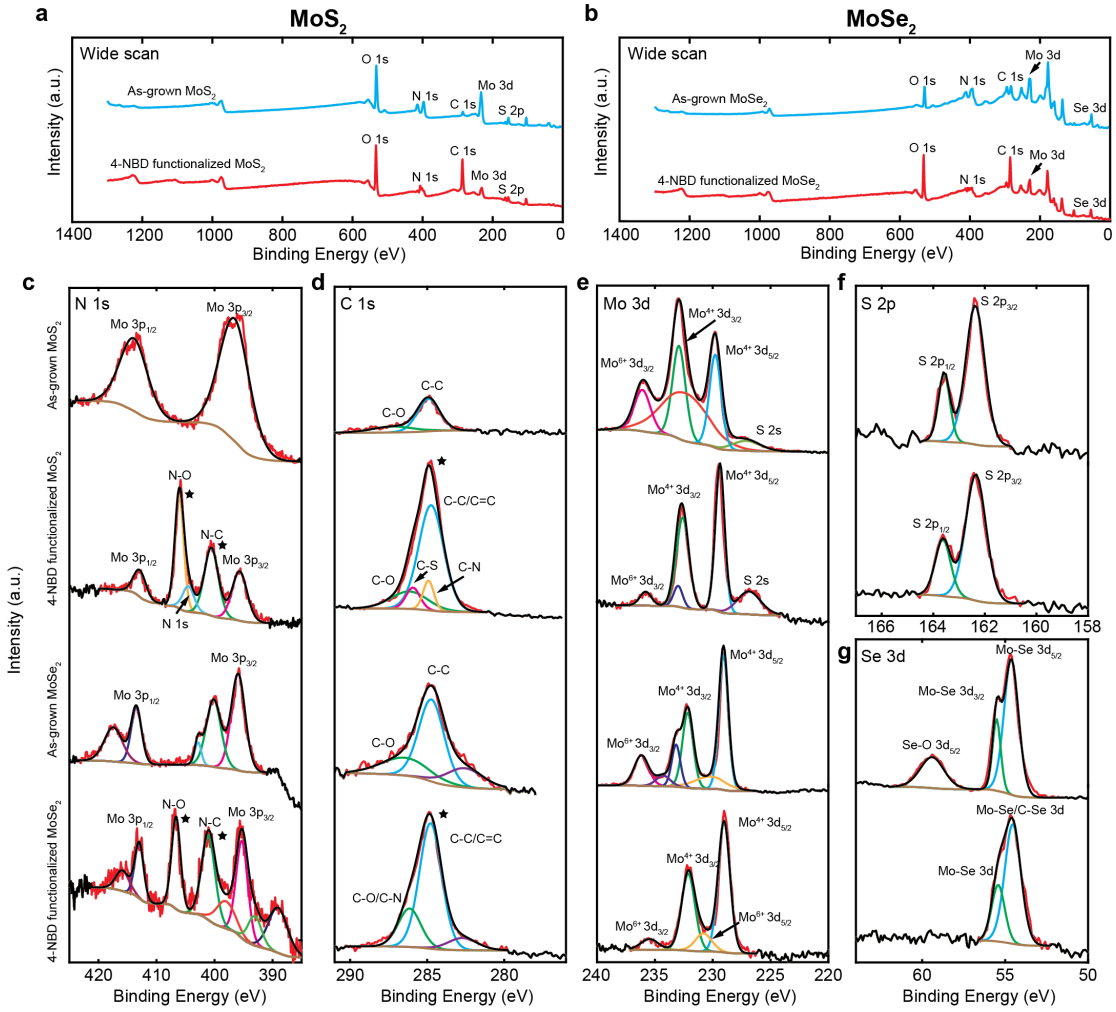

Figure 4.6: XPS spectra for CVD-grown MoS_2 and $MoSe_2$, before and after diazonium functionalization. a) Wide scan spectra for MoS_2. (b) Wide scan spectra for $MoSe_2$. (c)-(g) Detailed scans for the (c) N 1s region, (d) C 1 s region, (e) Mo 3d region, (f) S 2p region, and (g) Se 3d region. Important peak changes after functionalization in the N and C regions are indicated by stars.

sharp and clear peaks from N-O and N-C appear between the two Mo 3p peaks due to the attachment of nitrophenyl (NP) groups on both the MoS_2 and $MoSe_2$ surfaces. These peaks are indicated by stars. In the C 1s region in **Figure 4.6d**, the intensities of the C peaks on both MoS_2 and $MoSe_2$ increase after functionalization, indicating that there is an increase in the amount of carbon-containing bonds on the surface, primarily from the covalently attached groups. The spectra also suggest that in addition to the C-O and C-C/C=C peaks, there are also contributions from C-S bonds[128, 129] and C-N bonds[130] after functionalization. The C peaks with increased intensity are also marked by stars. In the Mo 3d region in **Figure S4.6e**, the typical peaks for MoS_2 and $MoSe_2$ are present. There are also peaks from Mo^{6+} 3d and Mo^{4+} 3d likely due to residues of the MoO_3 CVD growth precursor, which is a common impurity in these types of samples[131, 132]. Since the reaction time was only 30 min, the peak from the C-S bond in the S 2p region in panel **f** is too small to be seen (in our earlier work in Chu *et al.*[34] the C-S peak is most clear at 6 h of functionalization time). However, Se 3d peak in **Figure 4.6g** is broader after functionalization, which may be due to a contribution from the C-Se peak at about 54-55 eV[104], and further demonstrates the covalent attachment of NP groups on $MoSe_2$ surface.

4.2.3 Morphology of Functionalized Layered Chalcogenide Materials

The morphologies of the TMDCs and PCs upon functionalization were characterized by AFM and TEM imaging on mechanically exfoliated and liquid phase exfoliated samples, respectively. AFM imaging is particularly valuable here to directly show the attachment of organic groups on the surfaces of the TMDCs and PCs, and was previously used in our earlier work to elucidate reaction mechanisms

and kinetics by analyzing the change in surface coverage on MoS_2[34, 126]. The AFM images of as-exfoliated and functionalized TMDCs are shown in **Figure 4.7**. The thickness of the flakes ranges from 1 to 2 nm and corresponds to atomically thin monolayers and bilayers as shown in **Figure 4.7a-d**. After 5 s reaction in 4-NBD aqueous solution, small protrusions are observed on all the MoS_2, $MoSe_2$, WS_2 and WSe_2 flakes as shown in **Figure 4.7e-h**. The protrusions can be more clearly seen in the zoomed-in images in **Figure 4.7i-l**, which are from the areas highlighted by squares in **Figure 4.7e-h**. The heights of the protrusions range from 1 to 2 nm which is observed from height profiles shown in **Figure 4.7m-p**. The protrusions can be attributed to the nitrophenyl groups covalently attached onto the surfaces of the TMDCs nanosheets after reaction in 4-NBD aqueous solution. In addition, many of the protrusions are arranged in chain-like features are also observed on all the TMDCs because the attachment of 4-NBD molecules tend to propagate near the previously attached molecules, as found in our previous work on MoS_2 in Chu *et al.*[34] and Li *et al.*[126] which are also included in **Figure 4.7**. Physisorption is not expected to be a significant contribution because the samples were rinsed thoroughly with ultrapure water, and we previously showed in Chu *et al.*[34] via a control reaction with a molecule that lacks the diazonium group to form the covalent reaction that very little physisorption occurs[34].

AFM images of Bi_2S_3 and Sb_2S_3 flakes mechanically exfoliated from bulk powders are shown in **Figure 4.8**. The initial unreacted surfaces are shown in **Figure 4.8a-b**, where there are numerous atomic step edges visible, which tend to form ribbon-like features due to the presence of 1D chains in the crystal structure (see **Figure 4.1c-d**). The same regions of the samples are then shown after functionalization in **Figure 4.8c-f** (the asterisks indicate features that appear both before and after

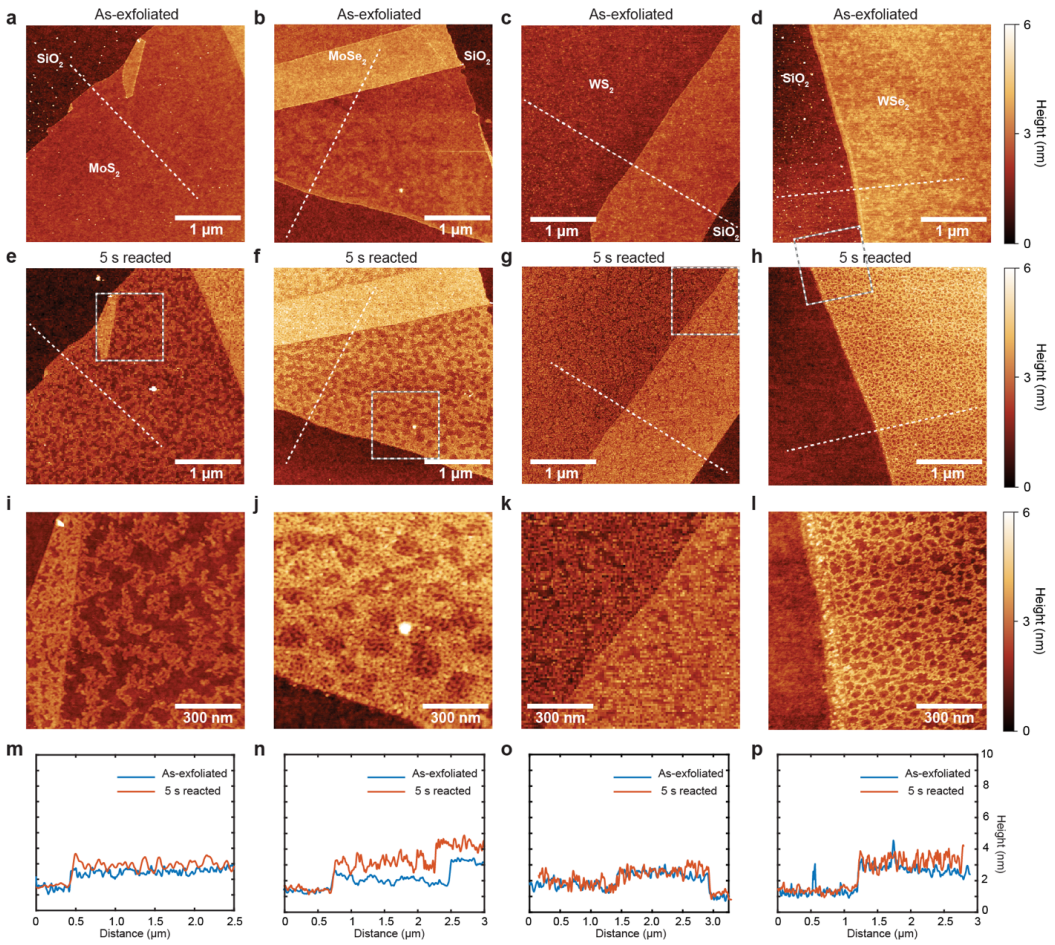

Figure 4.7: Surface functionalization of TMDCs imaged by atomic force microscopy (AFM). (a)-(d) As-exfoliated flakes of MoS_2, $MoSe_2$, WS_2 and WSe_2. (e)-(h) The flakes shown in (a)-(d) after 5 s functionalization with 10 mM of 4-NBD aqueous solution. (i)-(l) Zoom-in images of areas highlighted with dashed squares shown in (e)-(h). (m)-(p) Height profiles of the lines drawn across the flakes before and after functionalization. (Panels (a), (e), and (i) reprinted with permission from Chu *et al*[34]. Copyright 2018 American Chemical Society.)

functionalization to help guide the eye), where there are many protrusions uniformly covering the surfaces. The appearance of these protrusions is very similar to those that appear on TMDCs in **Figure 4.7**. There are some clusters observed in **Figure 4.8f** and the height ranges from 1-4 nm which is similar to our earlier results in Li *et al.*[126]. Thus, the PC materials and TMDC materials possess similar morphology after functionalization, suggesting consistent attachment of organic groups to the surfaces are 4-NBD treatment.

The morphologies of liquid exfoliated samples before and after 4-NBD functionalization were characterized by TEM imaging. Dispersions of nanosheets of TMDCs and PCs were prepared by dropping them onto lacey carbon grids. The samples that were studied were as-dispersed, treated with 4-NBD solution by sonication, and treated without 4-NBD solution by sonication as controls. Representative TEM images of these nanosheets are shown in **Figure 4.9**. There is relatively little visible change between the functionalized and non-functionalized WS_2 nanosheets as seen in **Figure 4.9a-c**. The nanosheets are still clearly visible as being quite thin, having different layer thicknesses, and being about 50-100 nm across.

For the PCs, a few distinct changes can be seen between functionalized and unfunctionalized samples. For Bi_2S_3, the as-dispersed nanosheets in **Figure 4.9d** have a distribution of large (a few hundred nanometers across) and small flakes, as do the control nanosheets with additional sonication but no 4-NBD exposure (**Figure 4.9e**). When the as-dispersed samples are functionalized with 4-NBD, as shown in **Figure 4.9f**, there are small particles on the surface of the flakes that are observed. We attribute these small particles to similar protrusions that are observed in AFM in **Figure 4.8e**, suggesting the successful attachment of NP groups onto the surface

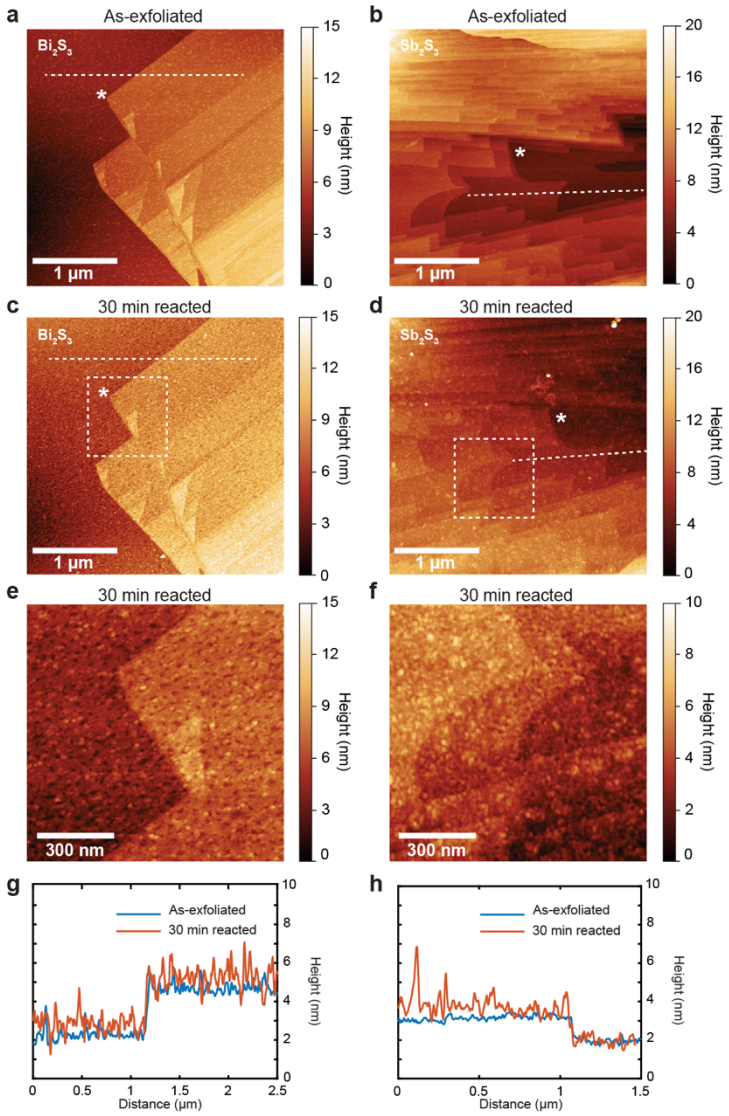

Figure 4.8: Surface functionalization of PCs imaged by atomic force microscopy (AFM). (a)-(b) As-exfoliated multilayer flakes of Bi_2S_3 and Sb_2S_3. Images are taken in the interiors of multilayer flakes, so the SiO_2/Si substrate is not shown. (c)-(d) The flakes shown in (a)-(b) after 30 min functionalization with 10 mM of 4-NBD aqueous solution. (e)-(f) Zoomed-in images of areas highlighted with dashed squares in (c)-(d). (g)-(h) Height profiles of the dashed lines drawn across the flakes before and after functionalization.

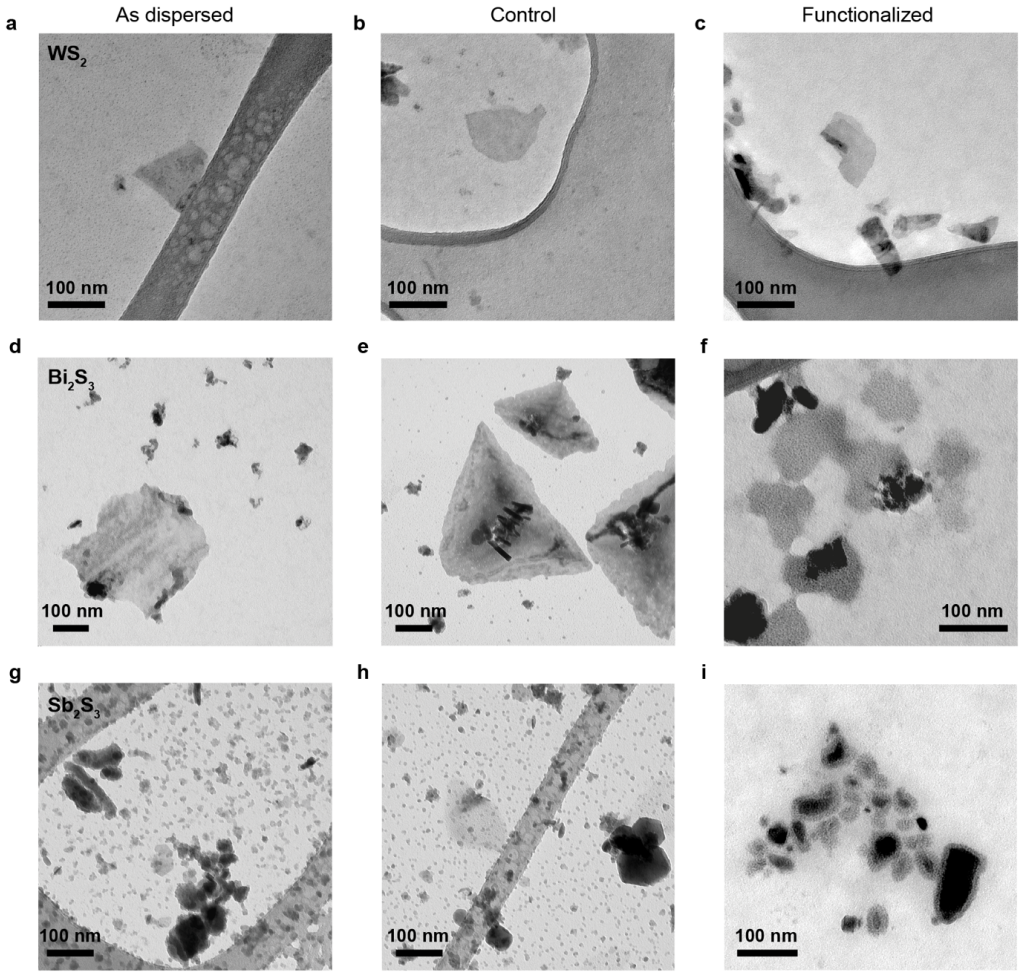

Figure 4.9: Transmission electron microscopy (TEM) of functionalized nanosheets. (a), (d) and (g) show nanosheets after exfoliation in SDS for WS_2, Bi_2S_3, and Sb_2S_3. (b), (e) and (h) show exfoliated flakes after additional sonication treatment with no 4-NBD to serve as a control. (c), (f) and (i) show exfoliated flakes after additional sonication treatment in the presence of 4-NBD to functionalize them.

of Bi_2S_3. In the case of Sb_2S_3, the as-dispersed control in **Figure 4.9g** and treated samples without 4-NBD (**Figure 4.9h**) showed similar morphologies, but the 4-NBD treated samples (**Figure 4.9i**) seem to have a coating around them, which may be due to a higher degree of functionalization extending into an oligomer formation or surface polymerization regime for these samples since the functionalization time for these materials was 4 h to ensure strong signals in FTIR, while the AFM samples were reacted for 30 min to maintain visibility of the underlying PC nanosheet surface.

The combination of spectroscopic and microscopic characterization methods here show the successful covalent functionalization of layered chalcogenide materials. FTIR spectroscopy reveals the successful attachment of nitrophenyl groups on TMDCs and PCs, particularly from the presence of the vibrations from the N-O, C=C, C-S, and C-Se bonds. Similarly from XPS data on MoS_2 and $MoSe_2$, we observe peaks consistent with successful covalent functionalization with the nitrophenyl groups. The TMDC and PC materials do not undergo any significant changes to their intrinsic crystal structures as elucidated by Raman spectroscopy. AFM and TEM imaging show the changes in morphology of the TMDCs and PCs upon functionalization. AFM imaging in particular clearly reveals the formation of small protrusions on the surfaces of all the mechanically exfoliated TMDCs and PCs, consistent with our previous observations for the functionalization of MoS_2[34, 126]. These protrusions have a similar height, and are attributed to the nitrophenyl groups attached to the basal planes of the layered chalcogenides. TEM imaging shows the nanosheets from liquid phase dispersion remain well-dispersed and stable upon functionalization, and with some low density features such as particles and overlayers that may correspond to the organic material covalently attached to the PCs. The functionalized materials also remain stable in aqueous dispersions, without

noticeable clumping or precipitation.

The proposed reaction mechanism for these materials is briefly discussed here. In our earlier work in Chu *et al.*[34] we showed for MoS_2 via DFT calculations and experiments using Ar^+ ions to introduce point defects imaged by STM that the functionalization reaction does depend on the presence of existing defects to initiate the reaction. Thus, an otherwise perfect crystal can be fully functionalized with just one initial defect, with the reaction propagating across the surface in a chain-like morphology. Our evidence from Raman, FTIR and AFM imaging suggests that a similar effect may be occurring for the new materials compositions in the current study. That is, the initial layered chalcogenide materials are nearly perfect based on their Raman spectra and the functionalization reaction proceeds by initiating at defects and edges and progresses in chain-like formations which can be seen in AFM images.

This functionalization scheme with diazonium salts is thus compatible with both wafer-scale and solution-based processing of TMDCs and PCs, and can be extended to other chemistries that have been previously used with graphene and MoS_2 to build from the aryl diazonium salts to form composite structures with quantum dots[133], polymers[134], and proteins[34, 41], and to induces changes to the electronic properties[43, 44]. We anticipate similar changes and applications will be possible for the TMDCd and PCs. That is, we will be able to exploit the known chemistries that were developed for the earlier materials like graphene and apply them to the TMDCs and PCs.

4.3 Conclusions

In conclusion, the functionalization of several compositions of 2D layered chalcogens from the TMDC and PC families has been demonstrated using aryl diazonium chemistry. While our earlier work studied the functionalization of only MoS_2 in detail, the present work demonstrates that this chemistry can readily be expanded to many other 2D layered chalcogens, in both mechanically exfoliated flakes and liquid phase dispersions. Thus, we have established that the aryl diazonium chemistry is a generalizable, effective, and broadly applicable approach to covalent functionalization of a diverse range of several compositions of 2D layered chalcogenides. The functionalized materials are characterized by a combination of spectroscopic and microscopic methods to show the presence of nitrophenyl groups attached to the surfaces of the TMDC materials MoS_2, $MoSe_2$, WS_2, and WSe_2, and the PC materials Bi_2S_3 and Sb_2S_3. This work provides a valuable chemical tool for the modification and application of layered chalcogenides, and opens the door to further chemistries that will expand the functionalities of these low-dimensional materials.

Chapter 5

ADSORPTION OF HEAVL METAL IONS ON MOS_2

Heavy metals contaminating water even at trace concentrations are very harmful for human health, and more effective technologies for removing them are needed. Two-dimensional (2D) materials have high specific surface areas that enable new surface phenomena and are promising new active components in water purification. Here, we demonstrate the adsorption of the heavy metals Pb, Cd, Zn and Co from aqueous solution on the surface of 2D molybdenum disulfide (MoS_2). Using atomic force microscopy (AFM), scanning electron microscopy (SEM), and elemental analysis by X-ray photoelectron spectroscopy (XPS), we show that the metals form nanoclusters on the MoS_2 surface without affecting the structure of the MoS_2 itself. We then show the metals can be readily desorbed from the MoS_2 surface by thermal annealing. The ability to adsorb metals from aqueous solution at low concentrations and then to thermally desorb them suggests a potential future application for MoS_2 as a regenerable water purification material. To make a practical adsorbent, we synthesize a composite foam from MoS_2 and polyurethane that demonstrates effective removal of Pb from water, with up to 89% removal efficiency at concentrations below 200 ppb. This strategy is a promising route for the synthesis of effective adsorbents from composites of polymers and 2D materials to remove heavy metal ions from water.

5.1 Experimental Methods

5.1.1 Preparation of As-Exfoliated MoS_2

Atomically thin MoS_2 samples were obtained by mechanical exfoliation from a bulk crystal of MoS_2 (SPI Supplies) by using scotch tape, and deposited onto a Si substrate coated with a 300 nm SiO_2 layer. The substrate was initially cleaned in sequential baths of acetone and 2-propanol, and blown dry with ultrahigh purity nitrogen before MoS_2 exfoliation. Single layer and multilayer MoS_2 flakes were identified by optical microscopy and Raman spectroscopy.

5.1.2 Adsorption of Metal Ions on MoS_2

As-exfoliated MoS_2 samples were immersed in aqueous solutions of heavy metal nitrates for 30 min. The solutions were made from $Pb(NO_3)_2$ (Sigma-Aldrich, ACS reagent, 99.0%), $Cd(NO_3)_2$ (Sigma-Aldrich, purum p.a., 99.0%), $Zn(NO_3)_2$ (Sigma-Aldrich, reagent grade, 98%), and $Co(NO_3)_2$ (Sigma-Aldrich, ACS reagent, 98%) in micropure water (18 MΩ). After rinsing thoroughly with micropure water, samples were blown dry with ultrahigh purity nitrogen. Atomic force microscope (AFM) images were taken before and after the metal ion exposure to detect the adsorption of metals forming into particles and islands.

5.1.3 Preparation of CVD-Grown MoS_2 for XPS

The SiO_2/Si growth substrate was sonicated in sequential baths of acetone and 2-propanol for 5 min each, followed by oxygen plasma cleaning (Harrick Plasma, PDC-32G) at high RF power (18 W). The growth was conducted in a horizontal tube

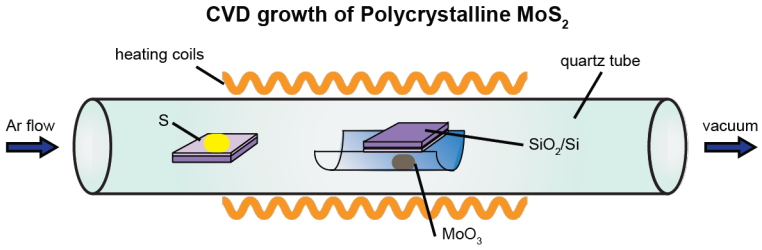

Figure 5.1: CVD growth of polycrystalline MoS_2. The growth substrate was sonicated in sequential baths of acetone and 2-propanol for 5 min each, followed by oxygen plasma cleaning at high RF power. 100 mg of S powder was held at the end of the heating coils at upstream, while 15 mg of MoO_3 was held in a curved Mo foil boat at the center of the heating zone as the precursors. The polished surface of the SiO_2/Si growth substrate was placed facing down across the Mo foil boat. The furnace was heated at 650°C for 30 min in vacuum with 300 sccm flow of ultrapure Ar.

furnace (ThermoFisher Lindberg) with 1-inch diameter quartz tube. The precursors were 100 mg of S powder (Alfa Aesar, precipitated, 99.5%) placed at the end of the heating coils at an upstream position, and 15 mg of MoO_3 (Sigma-Aldrich, ACS reagent, 99.5%) placed in a boat bent from Mo foil at the center of the heating zone. The polished surface of the SiO_2/Si growth substrate was placed face down across the Mo boat. The furnace was heated at 650°C for 30 min in vacuum with 300 sccm flow of ultrahigh purity Ar, followed by opening the furnace lid and cooling by an external fan. A schematic of the growth setup is shown in **Figure 5.1**.

5.1.4 Thermal Desorption of Metal Ions

The MoS_2 samples exposed to metal nitrate solutions were annealed in a tube furnace with a 1-inch diameter quartz tube at 300 °C for 2 hrs with a flow of 200 sccm of ultrahigh purity Ar as a carrier gas followed by AFM imaging.

5.1.5 Preparation of 3D Structures of 2D MoS_2

Based on a previously reported method, 60 13.1 g of 4,4'methylenebis(phenylisocyanate) (Sigma-Aldrich, MDI, 98%) flakes were crushed into powder in a weigh boat. Then, 0.4 g of silicone oil (Sigma-Aldrich, Dow Corning 200® fluid, viscosity 60,000 cSt @ 25 °C) and 20 mL glycerol propoxylate-block-ethoxylate (Sigma-Aldrich, average Mw 4000) were mixed into an HDPE beaker. Next, 0.7 mL of water and 0.188 mL of dibutyltin dilaurate (Sigma-Aldrich, 95%) were added to the HDPE beaker and the mixture was stirred. The MDI was added to the mixture, which was then rapidly mixed and left undisturbed. After about 1 hour, the foam was taken out and put in an oven set at 60 °C to dry overnight.

The same procedure as above was used, except that in place of 0.7 mL of water, 0.7 mL of a solution phase dispersion of MoS_2 in 1% w/v sodium dodecyl benzenesulfonate (SDBS technical grade) was used. To prepare the dispersion, 1.0 g MoS_2 powder (Sigma-Aldrich, <2 μm, 99%) was mixed with 6 mL of 1% w/v SDBS and tip sonicated in a Branson Sonifier 450 (tip diameter 3 mm) for 1 hour at 20% amplitude. The resulting sonicated dispersion was centrifuged at 5000 RCF for 4 minutes and the supernatant dispersion was extracted.

5.1.6 Removal of Metal Ions from Water

Pb, Cd, Zn, and Co nitrate solutions were prepared at 1000 ppb, 200 ppb and 50 ppb concentrations to test the performance of the polymer composite at different levels of contamination. In each experiment, 0.5 g of the MoS_2-polyurethane composite was immersed in 7 mL of metal nitrate aqueous solutions in metal-free

centrifuge tubes for 12 hours. The solutions were shaken thoroughly before and after the adsorption. Aliquots of the aqueous solutions were taken with plastic pipettes and diluted to proper concentrations with 0.32 M HNO_3 (BDH Aristar Plus, trace metal analysis, 67-70%) aqueous solution for acidification and measured by ICP-MS (ThermoFisher ELEMENT 2). The unmodified polyurethane foam was tested with the same protocol.

5.2 Results and Discussion

5.2.1 Adsorption of Metals on MoS_2 from Solution

The adsorption of Pb, Cd, Zn and Co on MoS_2 monolayers from aqueous solution was investigated by atomic force microscopy (AFM) using the steps shown in **Figure 5.2a-c**. Mechanically exfoliated MoS_2 flakes supported on SiO_2/Si substrates were immersed in aqueous solutions of metal nitrates at a concentration of 0.1 mM. The valency of all metal ions used in this study is +2. After exposure to the metal ion solutions, the MoS_2 samples were rinsed thoroughly with micropure water (18.2 MΩ) and blown dry with ultrahigh purity nitrogen, followed by AFM imaging. Pb, Co, Zn and Cd all appear to have good adsorption on MoS_2 based on AFM imaging as shown in **Figure 5.2** and **Figure 5.3**.

The pristine as-exfoliated MoS_2 surface is shown in the AFM image of **Figure 5.2d**. This sample includes monolayer, bilayer and trilayer regions of MoS_2. After being immersed in a lead nitrate ($Pb(NO_3)_2$) solution at 0.1 mM concentration and then rinsed and dried, AFM imaging reveals small nanometer-tall protrusions clearly visible on the MoS_2 surface, and not on the surrounding SiO_2 substrate as shown in

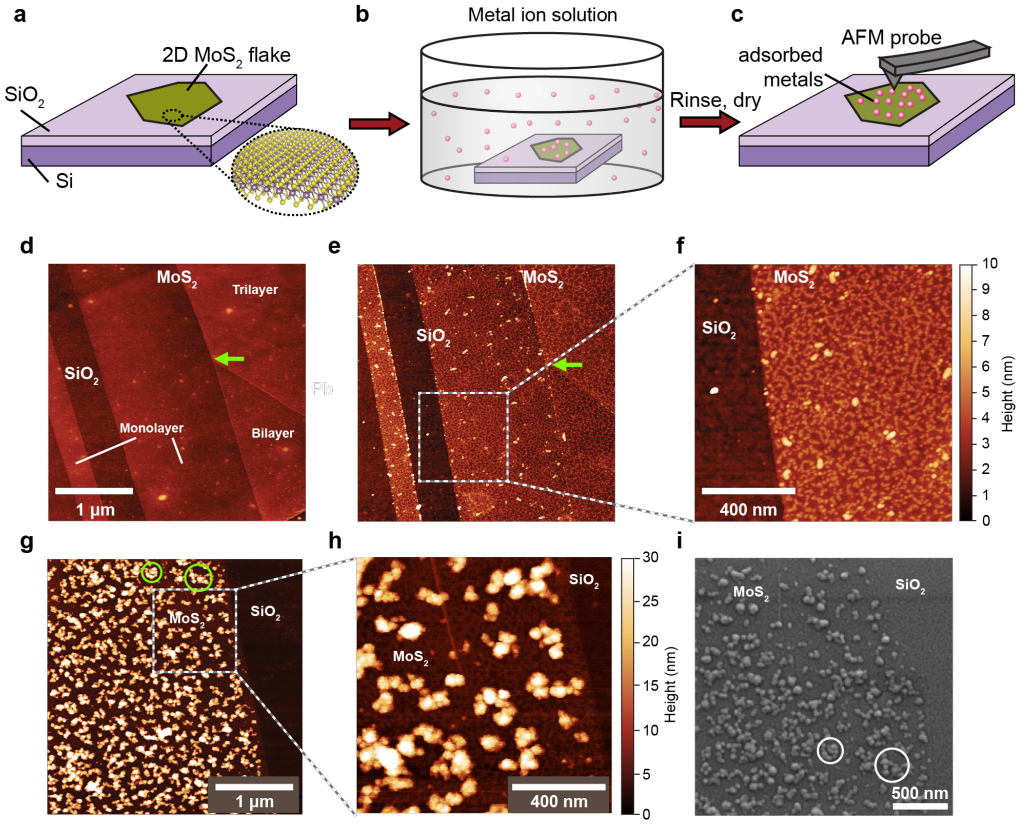

Figure 5.2: Adsorption of metal ions on MoS_2. (a) Schematic illustration of a mechanically exfoliated 2D MoS_2 flake on SiO_2/Si substrate. (b) MoS_2 samples are immersed in aqueous solutions of metal nitrates. (c) MoS_2 samples are then rinsed with purified water and blown dry with nitrogen before atomic force microscope (AFM) imaging. (d) AFM image of pristine as-exfoliated MoS_2. (e) AFM image in the same region as (d) after adsorption of Pb from aqueous solution. The arrows in (d) and (e) indicate the same spot on the sample. Small protrusions appear on MoS_2 but not on SiO_2 substrate. (f) Enlarged AFM image in the region marked by the dashed square in (e). (g)-(h) AFM images after adsorption of Co, with (h) showing the area in the dashed square in (g). (i) SEM image after adsorption of Co from aqueous solution. Panels (g) and (i) are approximately in the same position on the sample, with the circles indicating the same protrusions on the sample in both images.

Figure 5.2e-f. Similarly, after Cd and Zn deposition from $Cd(NO_3)_2$ and $Zn(NO_3)_2$ aqueous solutions at the same 0.1 mM concentration, small protrusions (1-2 nm tall) are found on MoS_2 surface as shown in **Figure 5.3**. In addition, some larger protrusions (8-10 nm tall), which we attribute to be Pb and Zn clusters, are visible after MoS_2 was immersed in Pb and Zn solutions. After exposure in Co, there are also some much larger clusters of about 25-30 nm in height and 50-100 nm in diameter as shown in **Figure 5.2g-h**. These protrusions were also confirmed by scanning electron microscopy (SEM) as shown in **Figure 5.2i**. The clusters we observe are not due to supersaturation of the solution, because the concentration of the $Co(NO_3)_2$ solution we used is several magnitudes lower than the solubility of Co (5.408 M at 18 °C)[135]. In addition, the samples were thoroughly rinsed with micropure water, and we do not observe any protrusions or clusters on the surrounding SiO_2.

5.2.2 Mechanism of Metal Adsorption on MoS_2 and Formation of the Clusters

Elemental analysis by X-ray photoelectron spectroscopy (XPS) was conducted after the metal adsorption from aqueous solutions to confirm the presence of metal ions on MoS_2, and to determine that the nitrate ions are not adsorbed (**Figure 5.4**). Continuous polycrystalline MoS_2 films were prepared by chemical vapor deposition (CVD) growth to accommodate the X-ray spotsize (see Methods for more details). The resulting 2-4 nm thin film of MoS_2 grown on SiO_2/Si is shown in **Figure 5.5**. Separate samples of MoS_2 were each dipped in metal nitrate solutions of Cd, Zn, and Pb for 30 min, followed by thorough rinsing before characterization with XPS.

In **Figure 5.4**, the rows show the XPS spectra of (from top to bottom) as-grown MoS_2, after adsorption of Cd, after adsorption of Zn and after adsorption of Pb,

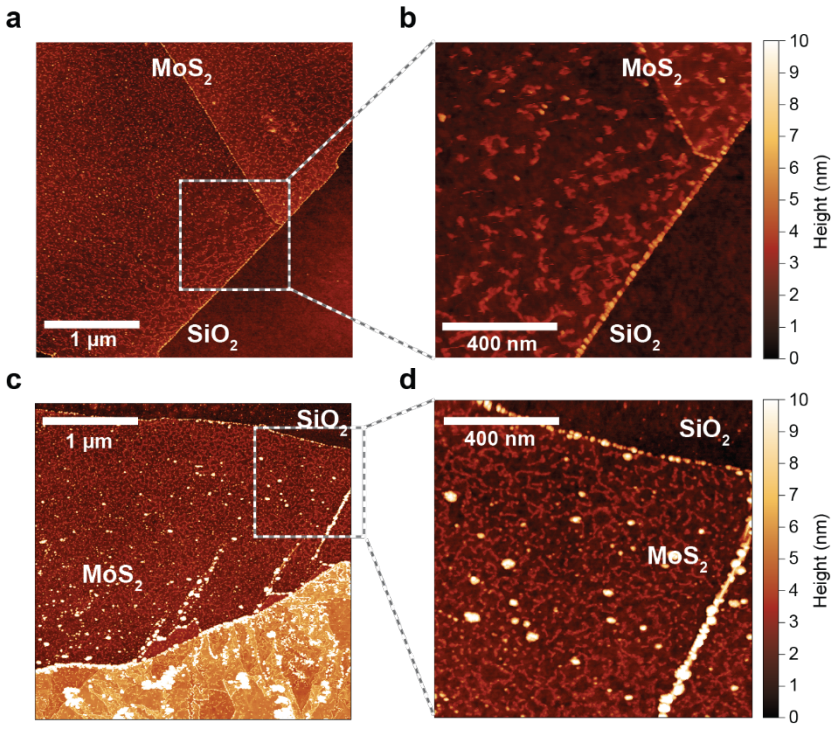

Figure 5.3: Adsorption of Cd and Zn on mechanically exfoliated MoS_2. (a) AFM image after adsorption of Cd from 0.1 mM aqueous solution of $Cd(NO_3)_2$. Small protrusions appear on MoS_2 but not on SiO_2 substrate. (b) Enlarged AFM image in the region marked by the dashed square in (a). (c) AFM image after adsorption of Zn from 0.1 mM aqueous solution of $Zn(NO_3)_2$. Small protrusions appear on MoS_2 but not on SiO_2 substrate. (d) Enlarged AFM image in the region marked by the dashed square in (c).

respectively. The energy ranges for N, Mo and S peaks are shown in columns a, b, and c, respectively. These results show that the MoS_2 material is largely unaffected by the metal nitrate solutions based on the similar intensities, positions, and shapes of the Mo^{4+} $3d_{3/2}$ peak, Mo^{4+} $3d_{5/2}$ peak[136, 137], and S peaks[136, 138, 139] as indicated by the results in **Figure 5.4b-c**. In addition, Mo^{6+} was also detected since the precursors for CVD growth of MoS_2 included MoO_3[140, 141]. In **Figure 5.4c**, the S $2p_{3/2}$ peak comes from MoS_2[136], whereas the S $2p_{1/2}$ peak may partially come from the S powder precursor[139]. In **Figure 5.4a**, compared to as-grown MoS_2, there are no N peaks emerging around 408.3 eV, which is reported to be the

typical position of the nitrooxy ($-O-NO_2$) peak[142]. This finding indicates that all nitrates were not adsorbed to the MoS_2 surface.

There is a more complicated situation in the second row of **Figure 5.4a**, since the binding energy ranges of Mo 3p, N, and Cd 3d partially overlap. Two components of Cd^{2+} were identified in the second row of **Figure 5.4a**, demonstrating the presence of Cd on the MoS_2 surface. The smaller component around 405 eV most likely originates from Cd $3d_{5/2}$[143]. The asymmetric peak at 412 eV is clearly different from that of the as-grown MoS_2, with another component that is likely from Cd $3d_{3/2}$[143].

In addition, clear Pb 4f peaks[144, 145] and Zn 2p peaks[146, 147] are respectively shown in **Figure 5.4d-e**, indicating the presence of Pb and Zn on MoS_2 surfaces of the samples immersed in those metal solutions. The absence of peaks due to covalent chemical bonds suggests that Zn is physisorbed to MoS_2 without strong bonding. According to reported DFT calculations, the adsorption energy of Zn is small and may be related to the fully filled 3d orbitals[35]. This observation is also supported by the weak intensity of Zn 2p peaks compared to the background. The intensity of Cd $3d_{5/2}$ is also weak and may be related to Cd having a similar electron configuration as Zn. However, it is reported that the Cd–S bonding peak is around 405.3 eV[143], and the Pb–S bonding peak is around 137.8 eV[144], which are both observed in our XPS results in **Figure 5.44.4c** and **f**. It is likely that there are more 3d electrons from Cd and 4f electrons from Pb transferred to MoS_2 compared to 2p electrons transferred from Zn. Therefore, these observations indicate Pb and Cd are more likely to be chemisorbed on MoS_2.

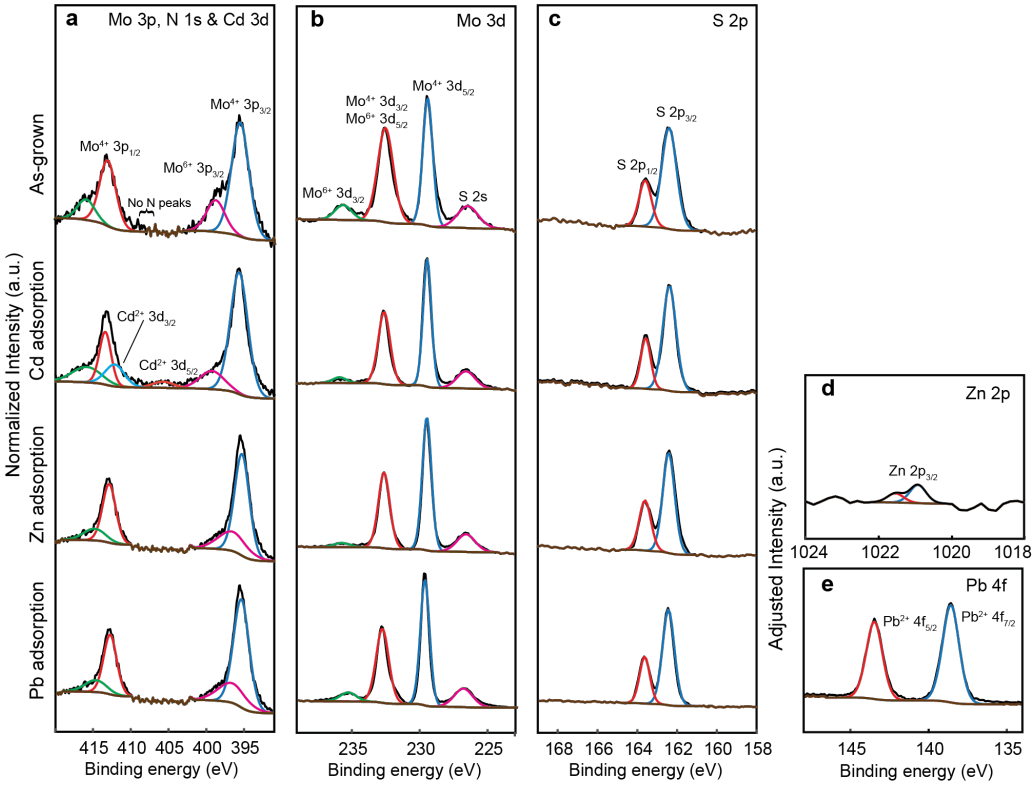

Figure 5.4: Chemical analysis of metal adsorption. X-ray photoelectron spectroscopy (XPS) spectra of MoS_2 grown by chemical vapor deposition are shown from top to bottom: as-grown, and after immersion in aqueous solutions of Cd, Zn and Pb nitrates, respectively, at 10 mM concentrations for 30 min. The spectra are vertically offset for clarity. (a) Mo 3p, N 1s, and Cd 3d peaks. (b) Mo 3d peaks. (c) S 2p peaks. The intensities of columns (a), (b), and (c) are normalized to the Mo^{4+} $3p^{3/2}$, Mo^{4+} $3d^{5/2}$, and S $2p^{3/2}$ peaks, respectively. Mo 3d and S 2p peaks do not change much in (a)-(c). (d) Zn 2p peaks. (e) Pb 4f peaks. The intensities of (d) and (e) are adjusted to show the peaks more clearly. Cd, Zn and Pb peaks are detected after adsorption of the respective metal ions, whereas N peaks are absent, indicating the nitrates have not adsorbed.

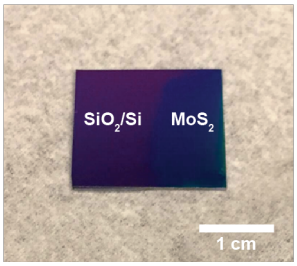

Figure 5.5: CVD-grown polycrystalline MoS_2 thin film. Photograph of MoS_2 grown on SiO_2/Si. The purple region on the left is the bare wafer and the blue region on the right shows a 2-4 nm thick polycrystalline film of MoS_2.

Usually the surface of MoS_2 is negatively charged due to the defects or reduction during its synthesis containing H^+ or Li^+ as counterions[39, 63, 83]. The primary mechanism could be ion exchange which happens between heavy metal ions and the cations on MoS_2 surface[148, 149]. Due to the stronger electrostatic attraction, heavy metal ions, for instance, Pb_2^+, could first approach to MoS_2 surface and replace H^+, and then form a Pb-S complexation with one or two S atoms, depending on the abundance of Pb_2^+ ions[150]. The formation of Pb-S complexation is supported by the reaction between Lewis acids and 2D materials[74]. At the top layer of MoS_2, each S atom possesses a tetrahedral electron configuration because of sp^3 hybridization. Three of the sp^3 orbitals form Mo–S bonds while the fourth is occupied by a lone pair of electrons to form a Lewis base[74, 151]. Therefore, heavy metal ions, as typical Lewis acids which can accept donated unshared electron pair[151], will react with 2D MoS_2. In this theory, Pb^{2+} as a Lewis acid can accept the lone pair electrons on MoS_2 surface due to its empty 6p orbitals and form stable coordinate covalent bonds[74]. Similarly, both electrostatic attraction and metal-sulfur complexation contribute to the adsorption of metal ions on MoS_2 surface[148, 149]. The clear Pb-S and Cd-S peaks indicate the complexation is dominant for Pb and Cd adsorption. The electrostatic attraction contributes more to the outer layer of adsorbed Pb. However, in the adsorption of Co, electrostatic is more crucial[152]. The weaker peaks in the adsorption of Zn compared to Pb and Cd, also demonstrate the complexation is not dominant and even physisorption could exist.

Another mechanism involving redox reaction could contribute to the interaction between metal ions and MoS_2 surface[40]. Ag^+ or other heavy metal ions could behave as a mild oxidant and may reduce itself to metallic state and deposit on MoS_2 when oxidizing MoS_2 to soluble molybdate and sulfate[153]. Hypothetically a similar

redox reaction may happen with the presence of other heavy metal ions which we are focusing on in this thesis. To further confirm the dominance of this redox reaction mechanism, we may need to determine the concentration of Mo in the solution after the removal of heavy metal ions using ICP-MS.

Other than the metal-MoS_2 adsorption, there has also been interaction between the metal ions. As a result, the formation and growth of the clusters are determined by the energy of both interactions[33]. We state the adsorption energy as E_{ad} and the correlation energy between the metal ions as E_{co}. E_{ad} and E_{co} energies of each elements are different due to the difference between the electron configurations and these parameters were investigated before[83, 154–156]. In their theoretical results, if $E_{ad} \gg E_{co}$, it would prefer to form uniformly distributed small protrusions to minimize the total energy, while it would form more 3D islands or clusters due to the stronger metal-metal interaction when $E_{ad} \ll E_{co}$. With our findings in AFM results as shown in **Figure 5.2f** and **Figure 5.3b**, we hypothesize that in the case of Pb and Cd adsorption, it agrees with the $E_{ad} \gg E_{co}$ situation. AFM results in **Figure 5.3c** shows more cluster indicating that E_{ad} may be much smaller than E_{co} in Zn adsorption. However, even if E_{ad}/E_{co} is reasonably large as 0.8, it still would form large clusters because the diffusion barrier of 0.8-0.9 eV to separate Co^{2+} ions is much harder to overcome[33].

5.2.3 Thermal Desorption of Metals

The adsorption of metal ions as nanoparticles on MoS_2 nanoflakes described in the AFM and XPS results above demonstrate that MoS_2 has potential to be an active agent in removing heavy metal pollutants from aqueous solution. The

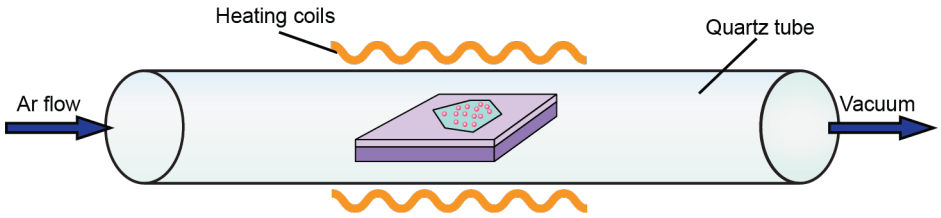

Figure 5.6: Schematic illustration of thermal desorption of metals from the MoS_2 surface via heating in a tube furnace. A sample of MoS_2 with adsorbed metal clusters was heated in a tube furnace under a 200 sccm flow of ultrahigh purity Ar gas in vacuum at 300 °C for 2 hours.

ability to regenerate and reuse the adsorbent material would be more efficient and economical as a water purification technology. Thus, the desorption of metals from the MoS_2 surface was studied to examine the possibility of employing MoS_2 as a reusable adsorbent. The method and experimental setup are illustrated in **Figure 5.6**. A sample of MoS_2 with adsorbed metal clusters was heated in a tube furnace under ultrahigh purity Ar gas flow at 300 °C for 2 hours, followed by AFM imaging. The sample with Pb clusters adsorbed shown above in **Figure 5.7c-d** was annealed, which resulted in the previously adsorbed Pb clusters being completely removed without damaging the MoS_2 surface. The Raman spectra of pristine as-exfoliated MoS2 and after thermal desorption shown in **Figure 5.8** are not significant changed, indicating that any structural changes have a very low concentration.

The same sample was then immersed in aqueous solutions of $Pb(NO_3)_2$ at a concentration of 0.1 mM to test its ability to readsorb Pb. As shown in **Figure 5.7g-h**, even more Pb protrusions are observed on MoS_2 surface demonstrating the reusability of MoS_2, suggesting its potential to be used as a regenerable adsorbent. The same protocol of desorption was applied to exfoliated MoS_2 after exposure to Zn and Cd nitrate aqueous solutions; we observe that almost all of the previously adsorbed Cd and Zn are removed as shown in **Figure 5.9** and **Figure 5.10**. A

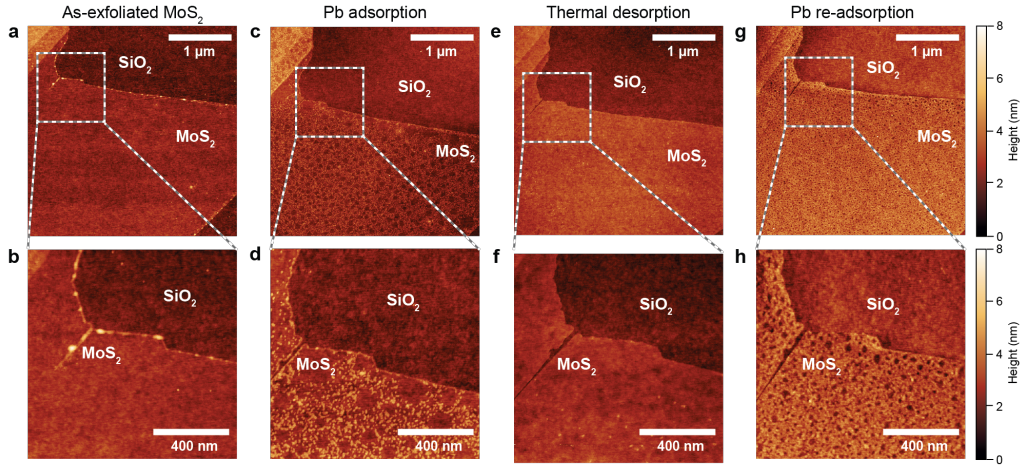

Figure 5.7: Thermal desorption of Pb from the MoS_2 surface. (a) AFM image of pristine as-exfoliated MoS_2 flake. (b) AFM image in area marked by dashed square in (a). (c) AFM image of MoS_2 after Pb adsorption from aqueous solution in the same area as (a) showing protrusions on the surface due to Pb adsorption. (d) AFM image in area marked by dashed square in (c). (e) AFM image of same sample after annealing at 300°C for 2 hours in vacuum with ultrahigh purity Ar as the carrier gas in the same area as (c) showing removal of the Pb clusters. (f) AFM image in area marked by dashed square in (e). (g) AFM image of same sample after Pb re-adsorption from aqueous solution in the same area as (e) showing higher coverage than in (c). (h) AFM image in area marked by dashed square in (g). The height scale for all images is the same as for (g) and (h).

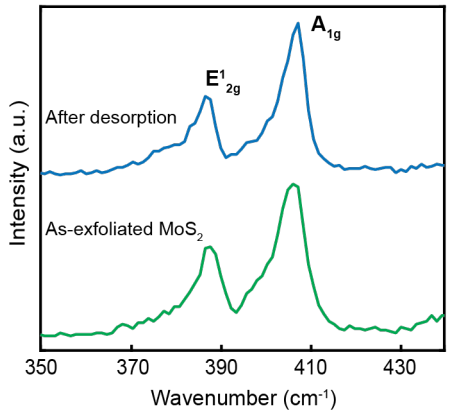

Figure 5.8: Raman spectra of as-exfoliated MoS_2 monolayer and MoS_2 monolayer after thermal desorption. Raman spectra taken from pristine as-exfoliated MoS_2 (green curve) and Pb adsorbed MoS_2 after thermal desorption (blue curve). The characteristic E^1_{2g} and A_{1g} peaks of MoS_2 are marked.

control experiment of Pb desorption at 180 °C was conducted without changes in all other parameters and the results are as shown in **Figure 5.11**. We observe that even though complete removal is not achieved, a considerable amount of Pb is still removed from the MoS_2 surface. This lower adsorption temperature will help to reduce the cost of desorption in potential future applications and expand the variety of the materials which can be combined with MoS_2.

Annealing in vacuum environment could help to induce more defects to MoS_2 surface[157] and we hypothesize the mechanism of metal desorption could be similar. In the case of Pb, with the temperature increasing, adsorbed Pb could detach from MoS_2 surface together with one or two sulfur atom to form PbS/PbS_2 and leave sulfur vacancies. With more sulfur vacancies, the reactivity of MoS_2 surface increases due to the higher density of states. It also helps to explain that more Pb ions get adsorbed on MoS_2. The mechanism could also apply to other metal ions. We hypothesize that there may be increasing concentrations of S-vacancies if the thermal desorption process and Pb adsorption are repeated for multiple cycles. One possible method to further restore the MoS_2 surface is to introduce thiol-containing molecules[158] after each thermal desorption step to either compensate the vacancies.

Control experiments with mechanically exfoliated monolayer graphene were conducted using the same protocol as described above, as an analogue to carbon-based water purification technologies such as activated carbon and other graphene-based adsorbents[159–161]. The adsorption and desorption of Zn and Cd on graphene are shown in **Figure 5.12**. While both Zn and Cd are readily adsorbed on graphene, thermal annealing was ineffective for removing the metals. Compared to MoS_2, metals adsorbed on graphene cannot be easily removed, indicating that it is difficult

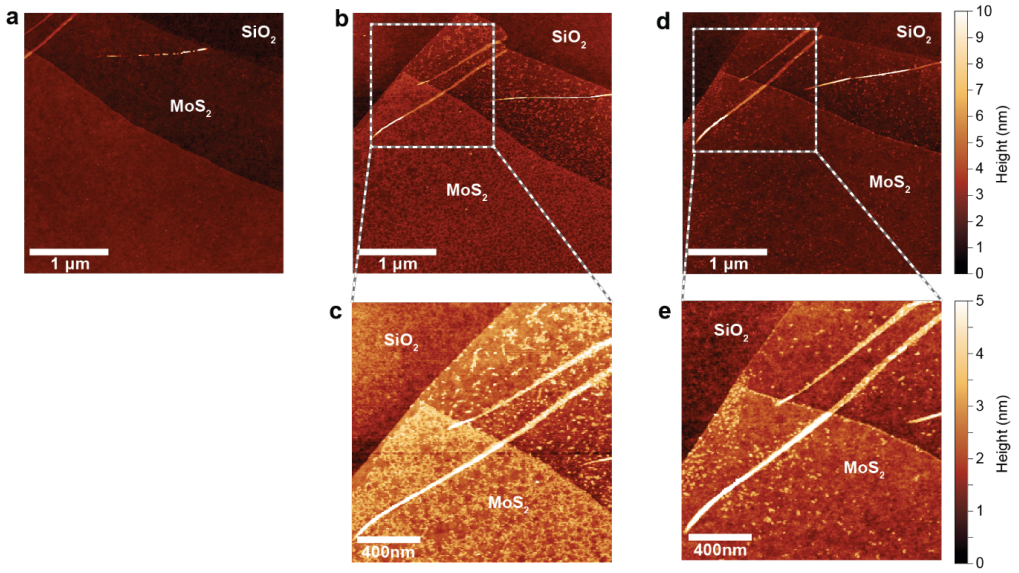

Figure 5.9: Thermal desorption of Cd from the MoS_2 surface. (a) AFM image of pristine as-exfoliated MoS_2 flake. (b) AFM image of MoS_2 after Cd adsorption from 0.1 mM aqueous solution of $Cd(NO_3)_2$ on the same MoS_2 sample as (a) showing protrusions on the surface due to Cd adsorption. (c) AFM image in area marked by dashed square in (b). (d) AFM image of same sample after annealing at 300 °C for 2 hours in vacuum with ultrapure Ar as carrier gas in the same area as (b) showing most of the Cd clusters have been removed. (e) AFM image in area marked by dashed square in (d).

to regenerate a graphene-based adsorbent for the removal of heavy metals. Based on this convenient thermal desorption procedure, MoS_2 has the potential to be applied in water purification as a reusable adsorbent material that can be regenerated by heating, making it a sustainable and cost-effective solution. Throughout these various processes in both liquid phase and gas phase, the MoS_2 material remains stable and is not significantly changed.

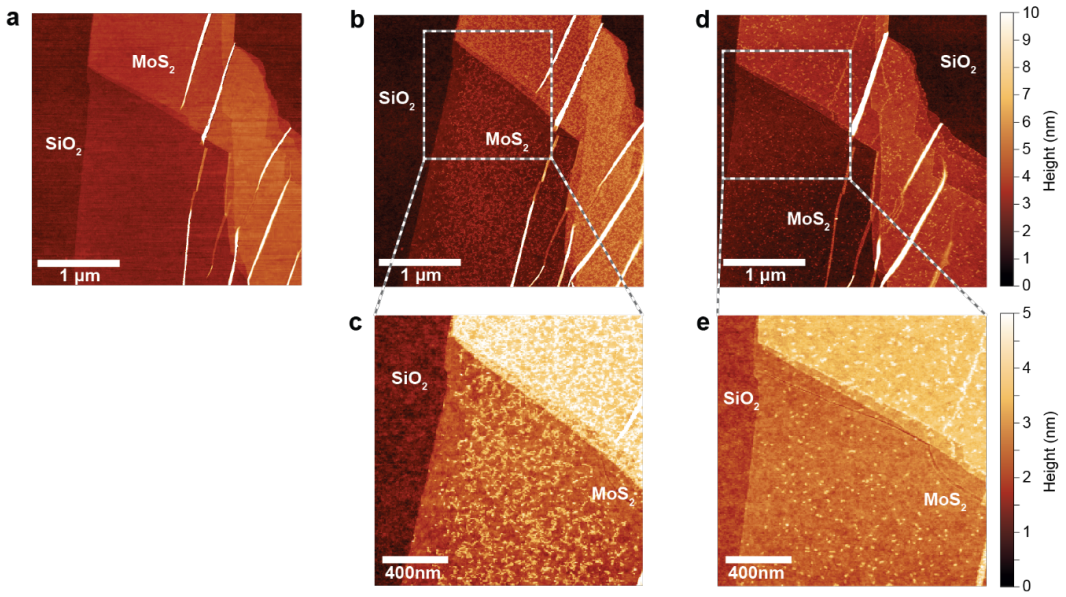

Figure 5.10: Thermal desorption of Zn from the MoS_2 surface. (a) AFM image of pristine as-exfoliated MoS_2 flake. (b) AFM image of MoS_2 after Zn adsorption from 0.1 mM aqueous solution of $Zn(NO_3)_2$ in the same area as (a) showing protrusions on the surface due to Zn adsorption. (c) AFM image in area marked by dashed square in (b). (d) AFM image of the same sample after annealing at 300 °C for 2 hours in vacuum with ultrapure Ar as carrier gas in the same area as (b) showing most of the Zn clusters have been removed. (e) AFM image in area marked by dashed square in (d).

5.2.4 Water Purification Using MoS_2-Polymer Composite Foam

In order to make a practical adsorbent material, it is necessary to engineer the 2D MoS_2 into a more robust, porous 3D macroscopic structure[162]. Unlike atomically thin membranes with nanopores[163], the composites which we fabricated have interconnected microscopic hollow spaces to form a 3D microporous structure that is structurally and mechanically robust. We synthesized polyurethane foam composites by combining solution phase dispersions of MoS_2 with a polyol precursor solution as schematically illustrated in **Figure 5.13a**. A typical polyurethane foam synthesis involves a polycondensation reaction between a trifunctional polyol and a

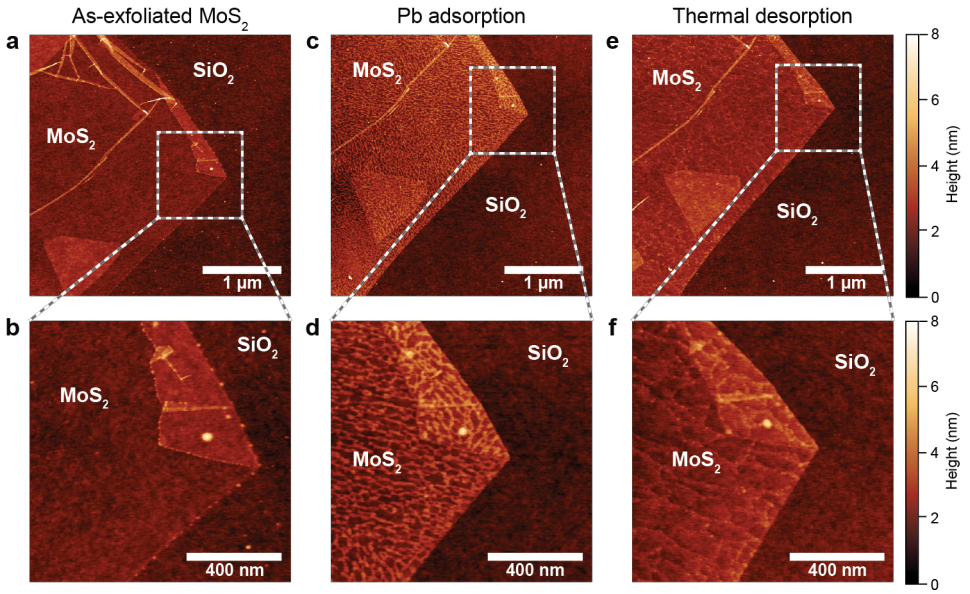

Figure 5.11: Thermal desorption of Pb from the MoS_2 surface at 180°C. (a) AFM image of pristine as-exfoliated MoS_2 flake. (b) AFM image in area marked by dashed square in (a). (c) AFM image of MoS_2 after Pb adsorption from 0.1 mM aqueous solution of $Pb(NO_3)_2$ in the same area as (a) showing protrusions on the surface due to Pb adsorption. (d) AFM image in area marked by dashed square in (c). (e) AFM image of same sample after annealing at 180 °C for 2 hours in vacuum with ultrahigh purity Ar as the carrier gas in the same area as (c) showing removal of the Pb clusters. (f) AFM image in area marked by dashed square in (e). The height scale for all images is the same as for (e) and (f).

diisocyanate in the presence of a surfactant, catalyst and blowing agent[164]. Here we added an aqueous MoS_2 dispersion as a blowing agent to a polyol solution containing a surfactant and catalyst, then added a diisocyanate to induce room temperature polymerization and foaming. We chose polyurethane as the polymer matrix because it is a commonly used and chemically inert foam material[165], with no exposure limits as established by the Occupational Safety and Health Administration (OSHA) or the American Conference of Governmental Industrial Hygienists (ACGIH), and because it is mechanically robust.

A solution phase dispersion of MoS_2 flakes in sodium dodecyl benzenesulfonate

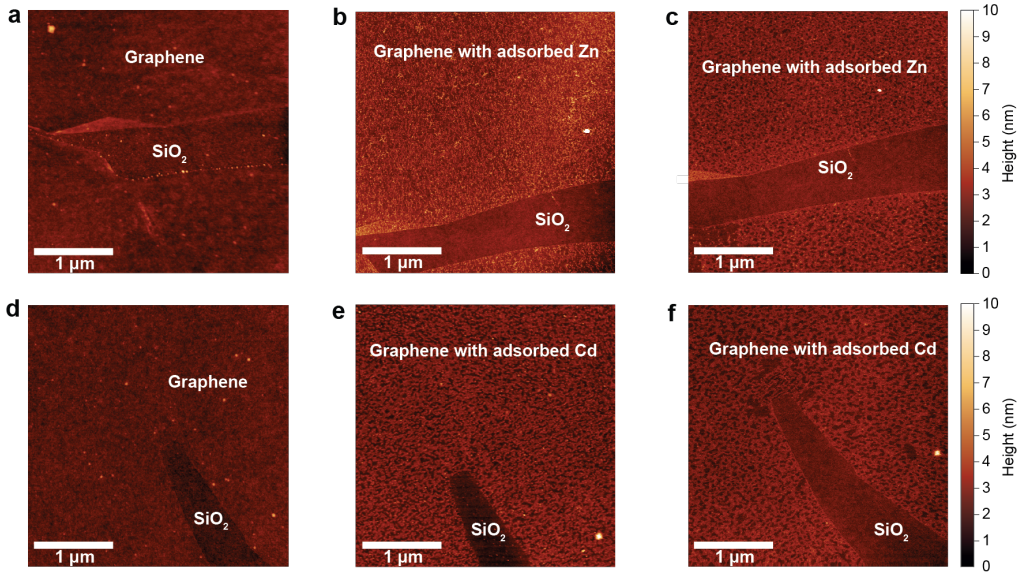

Figure 5.12: Adsorption and lack of thermal desorption of Zn and Cd on graphene. (a) AFM image of pristine as-exfoliated monolayer graphene. (b) AFM image of graphene after Zn adsorption. (c) AFM image of Zn adsorbed graphene after annealing at 300 °C for 2 hours in vacuum with ultrapure Ar as carrier gas in the same area as (b) showing negligible removal of the Zn. (d) AFM image of pristine as-exfoliated monolayer graphene. (e) AFM image of graphene after Cd adsorption. (f) AFM image of Cd-adsorbed graphene after annealing at the same condition showing negligible removal of Cd.

(SDBS) is shown in **Figure 5.13b**. The dispersion is dark green due to the high concentration of MoS_2 flakes. An AFM image of some MoS_2 nanoflakes in this dispersion spin-coated on a graphite substrate is shown in **Figure 5.14a**, and the height profile of one MoS_2 nanoflake is shown in **Figure 5.14b**. The sizes of the flakes range from 50 nm to a few hundred nanometers across. A plain polyurethane foam and one with MoS_2 embedded throughout were prepared (see Methods for more details), and are shown in **Figure 5.13c** and **d**, respectively. The polyurethane foam is white while MoS_2-polyurethane foam is green due to the presence of MoS_2. The change in color indicates that MoS_2 flakes have been uniformly distributed and embedded. Raman spectra of the unmodified foam and the composite with embedded MoS2 flakes are

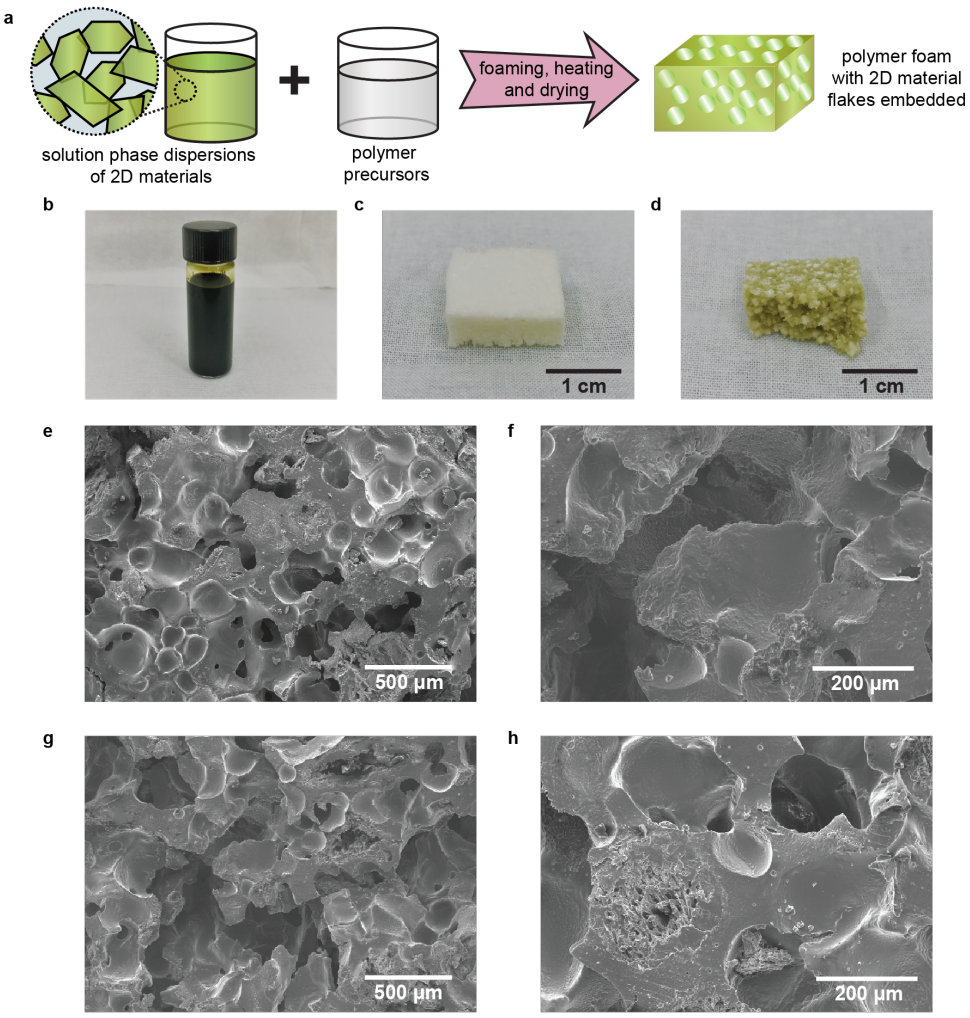

Figure 5.13: Forming 3D structures with 2D MoS_2. (a) Schematic illustration of synthesis process for polymer composites. Flakes of 2D materials dispersed in aqueous surfactant solution are mixed with polymer precursors. The mixture is foaming and drying to form a polymer foam with embedded 2D flakes. (b) Photograph of MoS_2 dispersed in SDBS aqueous solution. (c) Photograph of a polyurethane foam. (d) Photograph of a MoS_2-polyurethane composite foam. (e)-(f) SEM images of the polyurethane foam. (g)-(h) SEM images of the MoS_2-polyurethane composite foam.

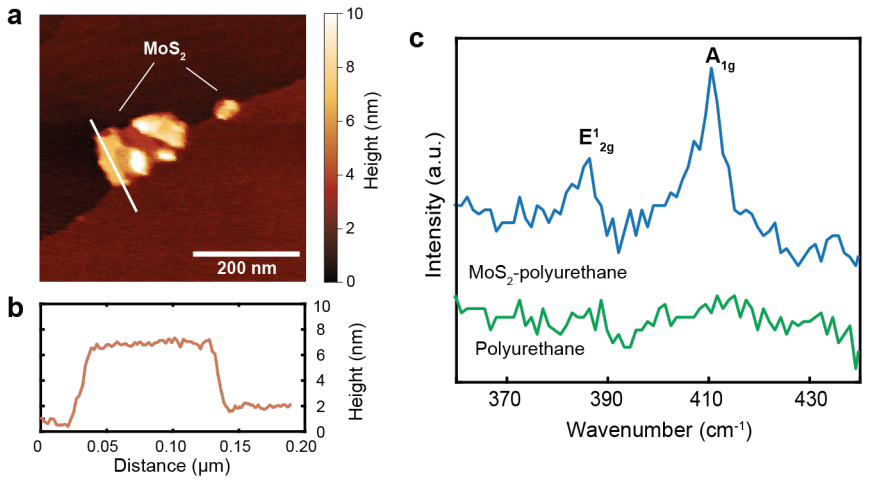

Figure 5.14: MoS_2 flakes from solution phase dispersion. (a) AFM image of MoS_2 nanoflakes from solution phase dispersion spin-coated on graphite substrate. (b) Line profile of the MoS_2 flake crossed by white line in (a). (c) Raman spectra taken from MoS_2-polyurethane composite foam (blue curve) and unmodified polyurethane foam (green curve). The characteristic $E^1{}_{2g}$ and A_{1g} peaks of MoS_2 are marked.

shown in **Figure 5.14c** and clear peaks characteristic of MoS_2 are only observed from the MoS_2-polyurethane composite indicating the successful embedding of MoS_2. SEM images of polyurethane foam are shown in **Figure 5.13e** and **f**, and of the MoS_2-polyurethane foam are shown in **Figure 5.13g** and **h**. Both types of foams have microporous structures, which provides high surface areas that are favorable in an adsorbent material. We note that the resolution of the SEM is not high enough to resolve the individual MoS_2 flakes. Batch adsorption experiments were conducted to study the performance of the MoS_2-polyurethane foam for removing metal ions from water. In all experiments, 0.5 g of adsorbent samples were immersed in metal-free centrifuge tubes with 7 mL of metal nitrate aqueous solutions to reach equilibrium at three initial concentrations. **Figure 5.15** shows the removal efficiency of Pb and Zn at 1000, 200 and 50 ppb concentrations. The removal efficiencies were calculated as the ratio of the metal ion concentrations before and after adsorption, which were measured by inductively coupled plasma mass spectrometry (ICP-MS). Control

experiments with polyurethane foam alone shows that it also has some adsorptive affinity for the metal ions. In the case of Pb, the embedded MoS_2 improved the adsorptive properties since the removal efficiency is much higher at all tested concentration levels. The removal efficiency of MoS_2-polyurethane foam at 1000 ppb is 61% which is nearly twice the efficiency of the polyurethane-only foam, and it also increases by 26.2 and 15.4 percentage points at 200 ppb and 50 ppb as shown in **Figure 5.15a**, respectively. At the 200 ppb and 50 ppb concentrations, we are able to remove 88.9% and 84.8% of the Pb, respectively. For Zn, the MoS_2-polyurethane foam also has higher removal efficiency, especially at 200 ppb and 50 ppb, where the polyurethane-only foam was not able to remove any Zn, as shown in **Figure 5.15c**. In additional experiments with Co, and Cd, we did not observe significant improvements in removal efficiency by adding MoS_2 to the polyurethane (see **Figure 5.16**), despite evidence of adsorption of metal clusters on MoS_2 from AFM measurements. Because of the wide variety of 2D materials available, future work will focus on engineering other 2D materials into 3D structures for use as adsorbent materials for removing these and other harmful metal ions from aqueous solutions.

From these ICP-MS results, both types of foam have selectivity for Pb and Zn, with the addition of MoS_2 improving the adsorption efficiency. The EPA limit for Pb in drinking water is 15 ppb[111], and the foam composite we synthesized has a potential to be applied as an adsorbent for removing Pb at concentrations lower than trace levels (concentrations below 100 ppm)[166], which is an improvement over many conventional adsorbents for removing Pb which are usually more effective at concentrations in the ppm range[135, 167]. MoS_2 can also be attached to 3D support structures beyond polyurethane which have better thermal performance for regenerating the material by thermal desorption, so detailed temperature dependent desorption will be addressed in future work. The diversity of available 2D materials and

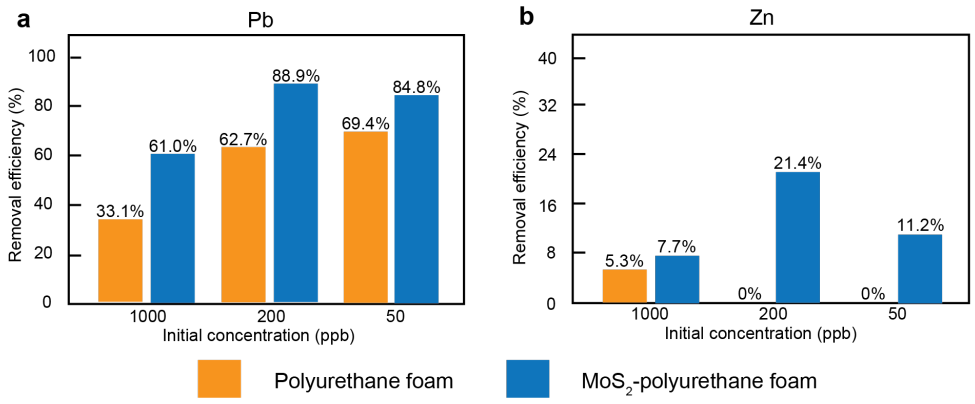

Figure 5.15: Removal of Pb and Zn from water. Inductively coupled plasma mass spectrometry (ICP-MS) was used to measure the metal ion concentrations of aqueous solutions before and after adsorption with polyurethane and MoS_2-polyurethane foams. Orange bars represent the removal efficiency of polyurethane foam alone and blue bars represent the removal efficiency of MoS_2-polyurethane composite foam. Adsorption efficiencies are calculated as ion concentration after adsorption divided by initial concentration. (a) Adsorption efficiencies for Pb solutions. (b) Adsorption efficiencies for Zn solutions. The initial concentrations are 1000, 200 and 50 ppb.

polymers to form a variety of composites suggests possibilities for removing different pollutants from water supplies. The thermal desorption of metals for regenerating the adsorbent can be also pursued via joule heating of the entire foam structure, as was demonstrated for the graphene foam composite cited earlier[168].

5.3 Conclusions

In conclusion, the adsorption of Pb, Cd, Zn and Co on MoS_2 from nitrate solutions has been demonstrated with AFM, SEM, and XPS. Both metal-sulfur complexation and the electrostatic attraction contribute to the adsorption of metal ions on MoS_2 surface. Pb and Cd ions were adsorbed onto the surface of MoS_2 as small 2D protrusions, while Co and Zn were adsorbed as larger clusters. We hypothesize that the metal complexation could desorb from MoS_2 as metal sulfide compounds by thermal annealing, indicating that MoS_2 has the potential to be

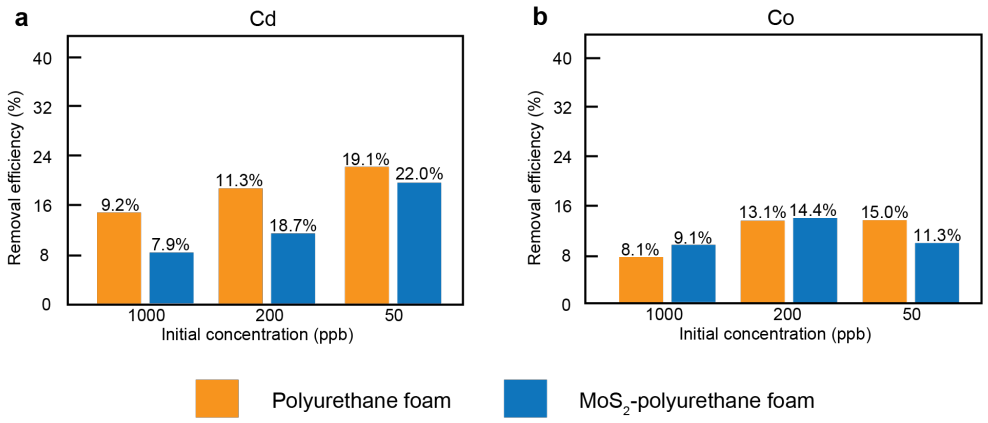

Figure 5.16: Removal of Cd and Co from water. Inductively coupled plasma mass spectrometry (ICP-MS) was used to measure the metal ion concentrations of aqueous solutions before and after adsorption with MoS_2-polyurethane foams. Orange bars represent the removal efficiency of polyurethane foam alone and blue bars represent the removal efficiency of MoS_2-polyurethane composite. Adsorption efficiencies are calculated as ion concentration after adsorption divided by initial concentration. (a) Adsorption efficiencies for Cd solutions. (b) Adsorption efficiencies for Co solutions. The initial concentrations are 1000, 200 and 50 ppb.

applied as a regenerable adsorbent. We synthesized a MoS_2-polyurethane composite foam that showed effective removal of Pb from water, especially at concentrations below 200 ppb where we achieve 85-89% removal of Pb. This work opens the door to studying the use of other 2D materials engineered into composites to be used as adsorbents for removing other pollutants from water. Further studies of detailed mechanisms of adsorption and desorption will provide deeper fundamental understanding.

5.4 Future Work

In order to confirm the mechanism and explore the potential of other applications for metal ions adsorbed on MoS_2, we plan to perform more characterization for the protrusions and clusters. The metal ions adsorption will be conducted with either

CVD-grown MoS_2 or solution phase dispersion of MoS_2 and characterized using TEM to analyze the crystal structure of the clusters. Besides heavy metals, the adsorption of other metal ions on MoS_2 will be investigated to confirm and expand our theory for the formation of different morphologies with different metal ions. DFT will be applied to simulate the adsorption of ions on MoS_2, to investigate the interactions, stable geometry and magnetic and electronic properties. We plan to work with our collaborator, Prof. Elton Santos at Queen's University Belfast who is an expert in DFT studies, to conduct these investigations. We will test the regenerability by performing multiple adsorption-desorption cycles and investigate the thermal desorption of metal ions from MoS_2 with the presence of molecules containing thiol group to extend the reusability.

Chapter 6

CONCLUSIONS

In this thesis, we have conducted thorough research on two crucial aspects of surface modification of MoS_2 and layered chalcogenides. First, our detailed study of the reaction kinetics and reaction mechanism confirmed and expanded on the reaction model put forth in our earlier work for the direct covalent functionalization of two-dimensional layers of semiconducting 2H-MoS_2 by the aryl diazonium salt 4-NBD in Chu et al.[34]. The adsorption study at different 4-NBD concentrations found that due to the energetically inhomogeneous surface of MoS_2 and indirect adsorbate-adsorbate interactions from the previously attached NP groups, both the Freundlich and Temkin isotherm models are a better description of the reaction. The reaction kinetics was better described using a pseudo-second order model, showing that the order of this reaction is two, and it further confirms the interaction between 4-NBD molecules.

Second, using a combination of optical, vibrational, and mechanical characterization techniques, we demonstrates that the functionalization chemistry for MoS_2 with aryl diazonium salts can readily be expanded to many other 2D layered TMDCs, such as $MoSe_2$, WS_2, and WSe_2, and the PCs, such as Bi_2S_3 and Sb_2S_3, in both mechanically exfoliated flakes and liquid phase dispersions. Thus, we have established that the aryl diazonium chemistry is a generalizable, effective, and broadly applicable approach to covalent functionalization of a diverse range of several compositions of 2D layered chalcogenides.

Finally, we confirmed the adsorption of Pb, Cd, Zn and Co on MoS_2 from nitrate solutions with AFM, SEM, and XPS. The metal ions were adsorbed onto the surface of MoS_2 as small nanoclusters, while the nitrates were rinsed away. The thermal desorption of metals from MoS_2 surface further demonstrates its potential in heavy metal removal from water due to its regenerability. We synthesized a MoS_2-polyurethane composite foam that showed effective removal of Pb from water. Our work provides more fundamental understanding for the application of MoS2 in water purification.

Overall, the work in this thesis helps to build the fundamental understanding of the surface modification of MoS_2, which may have implications for future applications in electronics, chemical sensing, biosensing and water purification. The broadened covalent functionalization chemistry also provides a valuable chemical tool for the modification and application of layered chalcogenides, and opens the door to further chemistries that will expand the functionalities of these low-dimensional materials.

Chapter 7

FUTURE WORK

In this thesis, we have conducted a fundamental investigation of surface interactions in layered chalcogenides undergoing covalent functionalization and metal adsorption. In this chapter, we will describe some potential future work to build on the results presented here.

The covalent functionalization of TMDCs and PCs has been demonstrated for a wide range of layered chalcogenide compositions, and can be used to enable future applications such as electronic devices and biosensors. Future work should be done to characterize the full extent of changes to the electronic and optical properties of all these materials. The diazonium chemistry can then be used to attach other structures such as proteins, DNA, and quantum dots to the chalcogenide surfaces to make hybrid materials that combine features and properties of different classes of materials. The presence of the organic groups may also be used to enhance the adsorption of heavy metals[169–172].

We will perform Pb adsorption together with competing species, such as Zn, Co and Cd, on both 4-NBD functionalized MoS_2 prepared by both mechanical exfoliation and liquid phase exfoliation. AFM will be used to characterize the morphology of Pb adsorbed on MoS_2 surface. We will perform SEM and TEM to investigate the crystal structure of Pb adsorbed on liquid phase exfoliated MoS_2. XPS will be applied to verify the metal-sulfur complexation and the selectivity to Pb. EDS mapping will also be used to identify the distribution of the ions to

demonstrate the selectivity to Pb. The control experiments will be completed by replacing the 4-NBD functionalized MoS_2 with as-exfoliated or as-dispersed MoS_2.

In addition, we plan to perform more characterization for the protrusions and clusters formed during metal adsorption on MoS_2 to further confirm the mechanism. We will use TEM to analyze the structure of the clusters adsorbed on MoS_2. The samples will be prepared using either CVD-grown or liquid phase exfoliated MoS_2 transferred onto lacey carbon grid. Other metal ions adsorption on MoS_2 will also be investigated to confirm and expand our theory for the formation of different morphologies with different metal ions. We plan to work with our collaborator, Prof. Elton Santos at Queen's University Belfast who is an expert in DFT studies, to conduct DFT simulation of the metal ion adsorption on MoS_2, to investigate the stable structure and mechanism. We will perform the stability test for adsorption-desorption and examine the thermal desorption of metal ions from MoS_2 with the presence of molecules containing thiol group to extend the reusability.

Finally, the metal nanoclusters adsorbed on MoS_2 can be characterized for potential optical, plasmonic, and magnetic properties. Nanoclusters of metals like gold and silver may have exhibit plasmonic enhancement and may serve as substrates for surface enhanced Raman spectroscopy (SERS). Nanoclusters of metals like cobalt, nickel, or iron may have magnetic properties.

REFERENCES

1. Wang, Q. H., Kalantar-Zadeh, K., Kis, A., Coleman, J. N. & Strano, M. S. Electronics and optoelectronics of two-dimensional transition metal dichalcogenides. *Nature Nanotechnology* **7,** 699 (2012).
2. Chhowalla, M. *et al.* The chemistry of two-dimensional layered transition metal dichalcogenide nanosheets. *Nature Chemistry* **5,** 263 (2013).
3. Novoselov, K. S. *et al.* Two-dimensional atomic crystals. *Proceedings of the National Academy of Sciences* **102,** 10451–10453 (2005).
4. Mak, K. F., Lee, C., Hone, J., Shan, J. & Heinz, T. F. Atomically thin MoS2: a new direct-gap semiconductor. *Physical Review Letters* **105,** 136805 (2010).
5. Splendiani, A. *et al.* Emerging photoluminescence in monolayer MoS2. *Nano Letters* **10,** 1271–1275 (2010).
6. Mattheiss, L. Band structures of transition-metal-dichalcogenide layer compounds. *Physical Review B* **8,** 3719 (1973).
7. Wilson, J. A. & Yoffe, A. The transition metal dichalcogenides discussion and interpretation of the observed optical, electrical and structural properties. *Advances in Physics* **18,** 193–335 (1969).
8. Hwang, J.-Y., Kim, Y.-M., Lee, K. H., Ohta, H. & Kim, S. W. Te monolayer-driven spontaneous van der waals epitaxy of two-dimensional pnictogen chalcogenide film on sapphire. *Nano Letters* **17,** 6140–6145 (2017).
9. García-Mendoza, C. *et al.* Synthesis of Bi2S3 nanorods supported on ZrO2 semiconductor as an efficient photocatalyst for hydrogen production under UV and visible light. *Journal of Chemical Technology & Biotechnology* **92,** 1503–1510 (2017).
10. Dean, C. R. *et al.* Boron nitride substrates for high-quality graphene electronics. *Nature Nanotechnology* **5,** 722 (2010).
11. Pacile, D., Meyer, J., Girit, Ç. & Zettl, A. The two-dimensional phase of boron nitride: Few-atomic-layer sheets and suspended membranes. *Applied Physics Letters* **92,** 133107 (2008).
12. Osada, M. & Sasaki, T. Two-dimensional dielectric nanosheets: novel nanoelectronics from nanocrystal building blocks. *Advanced Materials* **24,** 210–228 (2012).
13. Ayari, A., Cobas, E., Ogundadegbe, O. & Fuhrer, M. S. Realization and electrical characterization of ultrathin crystals of layered transition-metal dichalcogenides. *Journal of Applied Physics* **101,** 014507 (2007).

14. Radisavljevic, B., Radenovic, A., Brivio, J., Giacometti, i. V. & Kis, A. Single-layer MoS2 transistors. *Nature Nanotechnology* **6,** 147 (2011).

15. Ding, Y. *et al.* First principles study of structural, vibrational and electronic properties of graphene-like MX2 (M= Mo, Nb, W, Ta; X= S, Se, Te) monolayers. *Physica B: Condensed Matter* **406,** 2254–2260 (2011).

16. Beal, A., Hughes, H. & Liang, W. The reflectivity spectra of some group VA transition metal dichalcogenides. *Journal of Physics C: Solid State Physics* **8,** 4236 (1975).

17. Liu, L., Kumar, S. B., Ouyang, Y. & Guo, J. Performance limits of monolayer transition metal dichalcogenide transistors. *IEEE Transactions on Electron Devices* **58,** 3042–3047 (2011).

18. Kam, K. & Parkinson, B. Detailed photocurrent spectroscopy of the semiconducting group VIB transition metal dichalcogenides. *The Journal of Physical Chemistry* **86,** 463–467 (1982).

19. Kuc, A., Zibouche, N. & Heine, T. Influence of quantum confinement on the electronic structure of the transition metal sulfide T S 2. *Physical Review B* **83,** 245213 (2011).

20. Luo, Y. *et al.* Wet chemical synthesis of Bi2S3 nanorods for efficient photocatalysis. *Materials Letters* **105,** 12–15 (2013).

21. Sigman, M. B. & Korgel, B. A. Solventless synthesis of Bi2S3 (bismuthinite) nanorods, nanowires, and nanofabric. *Chemistry of Materials* **17,** 1655–1660 (2005).

22. Wen, S., Zhao, J., Zhao, Y., Xu, T. & Xu, J. Reduced graphene oxide (RGO) decorated Sb2S3 nanorods as anode material for sodium-ion batteries. *Chemical Physics Letters* **716,** 171–176 (2019).

23. Lu, F. *et al.* Improving the Field-Effect Performance of Bi2S3 Single Nanowires by an Asymmetric Device Fabrication. *ChemPhysChem* **16,** 99–103 (2015).

24. Yu, Y., Jin, C., Wang, R., Chen, Q. & Peng, L.-M. High-quality ultralong Bi2S3 nanowires: structure, growth, and properties. *The Journal of Physical Chemistry B* **109,** 18772–18776 (2005).

25. Dhar, N. *et al.* Exfoliation behavior of van der Waals strings: case study of Bi2S3. *ACS Applied Materials & Interfaces* **10,** 42603–42611 (2018).

26. Clark, R. M. *et al.* Exfoliation of Quasi-Stratified Bi2S3 Crystals into Micron-Scale Ultrathin Corrugated Nanosheets. *Chemistry of Materials* **28,** 8942–8950 (2016).

27. Guo, Y. *et al.* Efficient mixed-solvent exfoliation of few-quintuple layer Bi2S3 and its photoelectric response. *Nanotechnology* **28,** 335602 (2017).

28. Hou, H. *et al.* One-dimensional rod-like Sb2S3-based anode for high-performance sodium-ion batteries. *ACS Applied Materials & Interfaces* **7,** 19362–19369 (2015).

29. Ito, S., Tanaka, S., Manabe, K. & Nishino, H. Effects of surface blocking layer of Sb2S3 on nanocrystalline TiO2 for CH3NH3PbI3 perovskite solar cells. *The Journal of Physical Chemistry C* **118,** 16995–17000 (2014).

30. Moon, S.-J. *et al.* Sb2S3-based mesoscopic solar cell using an organic hole conductor. *The Journal of Physical Chemistry Letters* **1,** 1524–1527 (2010).

31. Hinnemann, B. *et al.* Biomimetic hydrogen evolution: MoS2 nanoparticles as catalyst for hydrogen evolution. *Journal of the American Chemical Society* **127,** 5308–5309 (2005).

32. Tsai, C., Abild-Pedersen, F. & Nørskov, J. K. Tuning the MoS2 edge-site activity for hydrogen evolution via support interactions. *Nano Letters* **14,** 1381–1387 (2014).

33. Saidi, W. A. Trends in the adsorption and growth morphology of metals on the MoS2 (001) surface. *Crystal Growth & Design* **15,** 3190–3200 (2015).

34. Chu, X. S. *et al.* Direct Covalent Chemical Functionalization of Unmodified Two-Dimensional Molybdenum Disulfide. *Chemistry of Materials* **30,** 2112–2128 (2018).

35. Wang, Y. *et al.* First-principles study of transition-metal atoms adsorption on MoS2 monolayer. *Physica E: Low-dimensional Systems and Nanostructures* **63,** 276–282 (2014).

36. Zhu, H. *et al.* Biochar derived from sawdust embedded with molybdenum disulfide for highly selective removal of Pb2+. *ACS Applied Nano Materials* **1,** 2689–2698 (2018).

37. Zhang, M., Jia, F., Dai, M. & Song, S. Combined electrosorption and chemisorption of low concentration Pb (II) from aqueous solutions with molybdenum disulfide as electrode. *Applied Surface Science* **455,** 258–266 (2018).

38. Pei, H. *et al.* Interfacial growth of nitrogen-doped carbon with multi-functional groups on the MoS2 skeleton for efficient Pb (II) removal. *Science of The Total Environment* **631,** 912–920 (2018).

39. Ai, K., Ruan, C., Shen, M. & Lu, L. MoS2 nanosheets with widened interlayer spacing for high-efficiency removal of mercury in aquatic systems. *Advanced Functional Materials* **26,** 5542–5549 (2016).

40. Wang, Z., Sim, A., Urban, J. J. & Mi, B. Removal and Recovery of Heavy Metal Ions by Two-dimensional MoS2 Nanosheets: Performance and Mechanisms. *Environmental Science & Technology* **52,** 9741–9748 (2018).

41. Wang, Q. H. *et al.* Understanding and controlling the substrate effect on graphene electron-transfer chemistry via reactivity imprint lithography. *Nature Chemistry* **4,** 724 (2012).

42. Wang, Q. H., Shih, C.-J., Paulus, G. L. & Strano, M. S. Evolution of physical and electronic structures of bilayer graphene upon chemical functionalization. *Journal of the American Chemical Society* **135,** 18866–18875 (2013).

43. Kaplan, A. *et al.* Current and future directions in electron transfer chemistry of graphene. *Chemical Society Reviews* **46,** 4530–4571 (2017).

44. Shih, C.-J. *et al.* Disorder imposed limits of mono-and bilayer graphene electronic modification using covalent chemistry. *Nano Letters* **13,** 809–817 (2013).

45. Alem, N. *et al.* Atomically thin hexagonal boron nitride probed by ultrahigh-resolution transmission electron microscopy. *Physical Review B* **80,** 155425 (2009).

46. Lee, C. *et al.* Anomalous lattice vibrations of single-and few-layer MoS2. *ACS Nano* **4,** 2695–2700 (2010).

47. Bertolazzi, S., Brivio, J. & Kis, A. Stretching and breaking of ultrathin MoS2. *ACS Nano* **5,** 9703–9709 (2011).

48. Tsai, H.-L., Heising, J., Schindler, J. L., Kannewurf, C. R. & Kanatzidis, M. G. Exfoliated- restacked phase of WS2. *Chemistry of Materials* **9,** 879–882 (1997).

49. Coleman, J. N. *et al.* Two-dimensional nanosheets produced by liquid exfoliation of layered materials. *Science* **331,** 568–571 (2011).

50. Smith, R. J. *et al.* Large-scale exfoliation of inorganic layered compounds in aqueous surfactant solutions. *Advanced Materials* **23,** 3944–3948 (2011).

51. Zhan, Y., Liu, Z., Najmaei, S., Ajayan, P. M. & Lou, J. Large-area vapor-phase growth and characterization of MoS2 atomic layers on a SiO2 substrate. *Small* **8,** 966–971 (2012).

52. Liu, K.-K. *et al.* Growth of large-area and highly crystalline MoS2 thin layers on insulating substrates. *Nano Letters* **12,** 1538–1544 (2012).

53. Balendhran, S. *et al.* Atomically thin layers of MoS2 via a two step thermal evaporation–exfoliation method. *Nanoscale* **4,** 461–466 (2012).

54. Shi, Y. *et al.* van der Waals epitaxy of MoS2 layers using graphene as growth templates. *Nano Letters* **12,** 2784–2791 (2012).

55. Late, D. J., Liu, B., Matte, H. R., Rao, C. & Dravid, V. P. Rapid characterization of ultrathin layers of chalcogenides on SiO2/Si substrates. *Advanced Functional Materials* **22,** 1894–1905 (2012).

56. Molina-Sanchez, A. & Wirtz, L. Phonons in single-layer and few-layer MoS2 and WS2. *Physical Review B* **84,** 155413 (2011).

57. Eda, G. *et al.* Photoluminescence from chemically exfoliated MoS2. *Nano Letters* **11,** 5111–5116 (2011).

58. Presolski, S. & Pumera, M. Covalent functionalization of MoS2. *Materials Today* **19,** 140–145 (2016).

59. Stergiou, A. & Tagmatarchis, N. Molecular Functionalization of Two-Dimensional MoS2 Nanosheets. *Chemistry–A European Journal* **24,** 18246–18257 (2018).

60. Kuila, T. *et al.* Chemical functionalization of graphene and its applications. *Progress in Materials Science* **57,** 1061–1105 (2012).

61. Paulus, G. L., Wang, Q. H. & Strano, M. S. Covalent electron transfer chemistry of graphene with diazonium salts. *Accounts of chemical research* **46,** 160–170 (2012).

62. Kalantar-zadeh, K. *et al.* Two-dimensional transition metal dichalcogenides in biosystems. *Advanced Functional Materials* **25,** 5086–5099 (2015).

63. Chou, S. S. *et al.* Ligand conjugation of chemically exfoliated MoS2. *Journal of the American Chemical Society* **135,** 4584–4587 (2013).

64. Kang, T. W. *et al.* 2D transition metal dichalcogenides with glucan multivalency for antibody-free pathogen recognition. *Nature Communications* **9,** 2549 (2018).

65. Karunakaran, S., Pandit, S., Basu, B. & De, M. Simultaneous Exfoliation and Functionalization of 2H-MoS2 by Thiolated Surfactants: Applications in Enhanced Antibacterial Activity. *Journal of the American Chemical Society* **140,** 12634–12644 (2018).

66. Huang, X.-W. *et al.* Silk fibroin-assisted exfoliation and functionalization of transition metal dichalcogenide nanosheets for antibacterial wound dressings. *Nanoscale* **9,** 17193–17198 (2017).

67. Yang, S. *et al.* Phosphonate and carboxylic acid co-functionalized MoS2 sheets for efficient sorption of uranium and europium: Multiple groups for broad-spectrum adsorption. *Journal of Hazardous Materials* **354,** 191–197 (2018).

68. Hong, S. *et al.* n-Type Doping Effect of CVD-Grown Multilayer MoSe2 Thin Film Transistors by Two-Step Functionalization. *Advanced Electronic Materials* **4,** 1800308 (2018).

69. Chen, X. & McDonald, A. R. Functionalization of Two-Dimensional Transition-Metal Dichalcogenides. *Advanced Materials* **28,** 5738–5746 (2016).

70. Voiry, D. *et al.* Covalent functionalization of monolayered transition metal dichalcogenides by phase engineering. *Nature Chemistry* **7,** 45 (2015).

71. Knirsch, K. C. *et al.* Basal-plane functionalization of chemically exfoliated molybdenum disulfide by diazonium salts. *ACS Nano* **9,** 6018–6030 (2015).

72. Lin, Y.-C., Dumcenco, D. O., Huang, Y.-S. & Suenaga, K. Atomic mechanism of the semiconducting-to-metallic phase transition in single-layered MoS2. *Nature Nanotechnology* **9,** 391 (2014).

73. Wypych, F. & Schöllhorn, R. 1T-MoS2, a new metallic modification of molybdenum disulfide. *Journal of the Chemical Society, Chemical Communications,* 1386–1388 (1992).

74. Lei, S. *et al.* Surface functionalization of two-dimensional metal chalcogenides by Lewis acid–base chemistry. *Nature Nanotechnology* **11,** 465 (2016).

75. Cowell, E. Chemical warfare and the doctor - I. English. *BRITISH MEDICAL JOURNAL* **2,** 736–738. ISSN: 0959-535X (JUL-DEC 1939).

76. Du, Y., Liu, H., Neal, A. T., Si, M. & Peide, D. Y. Molecular Doping of Multilayer MoS2 Field-Effect Transistors: Reduction in Sheet and Contact Resistances. *IEEE Electron Device Letters* **34,** 1328–1330 (2013).

77. Yang, L. *et al.* Chloride molecular doping technique on 2D materials: WS2 and MoS2. *Nano Letters* **14,** 6275–6280 (2014).

78. Dhakal, K. P. *et al.* Confocal absorption spectral imaging of MoS2: optical transitions depending on the atomic thickness of intrinsic and chemically doped MoS2. *Nanoscale* **6,** 13028–13035 (2014).

79. Mouri, S., Miyauchi, Y. & Matsuda, K. Tunable photoluminescence of monolayer MoS2 via chemical doping. *Nano Letters* **13,** 5944–5948 (2013).

80. Schmidt, H., Giustiniano, F. & Eda, G. Electronic transport properties of transition metal dichalcogenide field-effect devices: surface and interface effects. *Chemical Society Reviews* **44,** 7715–7736 (2015).

81. Backes, C. *et al.* Functionalization of liquid-exfoliated two-dimensional 2H-MoS2. *Angewandte Chemie International Edition* **54,** 2638–2642 (2015).

82. Manos, M. J. & Kanatzidis, M. G. Metal sulfide ion exchangers: superior sorbents for the capture of toxic and nuclear waste-related metal ions. *Chemical science* **7,** 4804–4824 (2016).

83. Wang, Z. & Mi, B. Environmental applications of 2D molybdenum disulfide (MoS2) nanosheets. *Environmental Science & Technology* **51,** 8229–8244 (2017).

84. Song, H. J., You, S., Jia, X. H. & Yang, J. MoS2 nanosheets decorated with magnetic Fe3O4 nanoparticles and their ultrafast adsorption for wastewater treatment. *Ceramics International* **41,** 13896–13902 (2015).

85. Massey, A. T., Gusain, R., Kumari, S. & Khatri, O. P. Hierarchical microspheres of MoS2 nanosheets: efficient and regenerative adsorbent for removal of water-soluble dyes. *Industrial & Engineering Chemistry Research* **55,** 7124–7131 (2016).

86. Gao, X., Wang, X., Ouyang, X. & Wen, C. Flexible Superhydrophobic and Superoleophilic MoS2 sponge for highly efficient oil-water separation. *Scientific Reports* **6,** 27207 (2016).

87. Roobakhsh, S., Rostami, Z. & Azizian, S. Can MoS2 nanosheets be used as adsorbent for water treatment? *Separation and Purification Technology* **200,** 23–28 (2018).

88. Gan, X. *et al.* Covalent functionalization of MoS2 nanosheets synthesized by liquid phase exfoliation to construct electrochemical sensors for Cd (II) detection. *Talanta* **182,** 38–48 (2018).

89. Gao, L., Yang, Z.-D. & Zhang, G. A theoretical study for electronic and transport properties of covalent functionalized MoS2 monolayer. *Chemical Physics* **490,** 29–37 (2017).

90. Chen, C. *et al.* Effect of glycine functionalization of 2D titanium carbide (MXene) on charge storage. *Journal of Materials Chemistry A* **6,** 4617–4622 (2018).

91. Liu, S. *et al.* Functionalization of hexagonal boron nitride nanosheets and their copolymerized solid glasses. *2D Materials* **5,** 035036 (2018).

92. Yin, Z. *et al.* Single-layer MoS2 phototransistors. *ACS Nano* **6,** 74–80 (2011).

93. Akinwande, D., Petrone, N. & Hone, J. Two-dimensional flexible nanoelectronics. *Nature Communications* **5,** 5678 (2014).

94. Sarkar, D. *et al.* Functionalization of transition metal dichalcogenides with metallic nanoparticles: implications for doping and gas-sensing. *Nano Letters* **15,** 2852–2862 (2015).

95. Kang, P., Wang, M. C. & Nam, S. Bioelectronics with two-dimensional materials. *Microelectronic Engineering* **161,** 18–35 (2016).

96. Kalantar-zadeh, K. & Ou, J. Z. Biosensors based on two-dimensional MoS2. *Acs Sensors* **1,** 5–16 (2015).

97. Wang, Y. *et al.* BSA-Mediated Synthesis of Bismuth Sulfide Nanotheranostic Agents for Tumor Multimodal Imaging and Thermoradiotherapy. *Advanced Functional Materials* **26,** 5335–5344 (2016).

98. Ryder, C. R. *et al.* Covalent functionalization and passivation of exfoliated black phosphorus via aryl diazonium chemistry. *Nature Chemistry* **8,** 597 (2016).

99. Bahr, J. L. *et al.* Functionalization of carbon nanotubes by electrochemical reduction of aryl diazonium salts: a bucky paper electrode. *Journal of the American Chemical Society* **123,** 6536–6542 (2001).

100. Wang, J. *et al.* Construction of multifunctional MoSe2 hybrid towards the simultaneous improvements in fire safety and mechanical property of polymer. *Journal of Hazardous Materials* **352,** 36–46 (2018).

101. Chen, Z. *et al.* Amino functionalization of graphene/graphene-like MoSe2 hybrids as lubricant additives for bismaleimide composites: Preparation, mechanical and tribological properties. *Composites Part B: Engineering* **161,** 263–271 (2019).

102. Grayfer, E. D., Kozlova, M. N. & Fedorov, V. E. Colloidal 2D nanosheets of MoS2 and other transition metal dichalcogenides through liquid-phase exfoliation. *Advances in Colloid and Interface Science* **245,** 40–61 (2017).

103. Manjunatha, S., Rajesh, S., Vishnoi, P. & Rao, C. Reaction with organic halides as a general method for the covalent functionalization of nanosheets of 2D chalcogenides and related materials. *Journal of Materials Research* **32,** 2984–2992 (2017).

104. Vishnoi, P., Sampath, A., Waghmare, U. V. & Rao, C. Covalent functionalization of nanosheets of MoS2 and MoSe2 by substituted benzenes and other organic molecules. *Chemistry–A European Journal* **23,** 886–895 (2017).

105. Ramanery, F. P., Mansur, A. A., Mansur, H. S., Carvalho, S. M. & Fonseca, M. C. Biocompatible Fluorescent Core-Shell Nanoconjugates Based on Chitosan/Bi 2 S 3 Quantum Dots. *Nanoscale Research Letters* **11,** 187 (2016).

106. Mansur, A. A., Ramanery, F. P., Oliveira, L. C. & Mansur, H. S. Carboxymethyl chitosan functionalization of Bi2S3 quantum dots: towards ecofriendly fluorescent core-shell nanoprobes. *Carbohydrate Polymers* **146,** 455–466 (2016).

107. Dou, R. *et al.* The polyvinylpyrrolidone functionalized rGO/Bi 2 S 3 nanocomposite as a near-infrared light-responsive nanovehicle for chemo-photothermal therapy of cancer. *Nanoscale* **8,** 11531–11542 (2016).

108. Lukowski, M. A. *et al.* Enhanced hydrogen evolution catalysis from chemically exfoliated metallic MoS2 nanosheets. *Journal of the American Chemical Society* **135,** 10274–10277 (2013).

109. Huang, X. *et al.* Solution-phase epitaxial growth of noble metal nanostructures on dispersible single-layer molybdenum disulfide nanosheets. *Nature Communications* **4,** 1444 (2013).

110. Järup, L. Hazards of heavy metal contamination. *British Medical Bulletin* **68,** 167–182 (2003).

111. EPA, U. Environmental Protection Agency, National Primary Drinking Water Regulations: Radio Nuclides; Proposed Rules. *Federal Register* **56,** 33050 (1991).

112. Nečas, D. & Klapetek, P. Gwyddion: an open-source software for SPM data analysis. *Open Physics* **10,** 181–188 (2012).

113. Schindelin, J. *et al.* Fiji: an open-source platform for biological-image analysis. *Nature Methods* **9,** 676 (2012).

114. Jariwala, D. *et al.* Nanoscale doping heterogeneity in few-layer WSe2 exfoliated onto noble metals revealed by correlated SPM and TERS imaging. *2D Materials* **5,** 035003 (2018).

115. Mignuzzi, S. *et al.* Effect of disorder on Raman scattering of single-layer Mo S 2. *Physical Review B* **91,** 195411 (2015).

116. McDonnell, S., Addou, R., Buie, C., Wallace, R. M. & Hinkle, C. L. Defect-dominated doping and contact resistance in MoS2. *ACS Nano* **8,** 2880–2888 (2014).

117. Hossain, M. Z., Walsh, M. A. & Hersam, M. C. Scanning tunneling microscopy, spectroscopy, and nanolithography of epitaxial graphene chemically modified with aryl moieties. *Journal of the American Chemical Society* **132,** 15399–15403 (2010).

118. Greenwood, J. *et al.* Covalent modification of graphene and graphite using diazonium chemistry: tunable grafting and nanomanipulation. *ACS Nano* **9,** 5520–5535 (2015).

119. Masel, R. I. *Principles of Adsorption and Reaction on Solid Surfaces* (John Wiley & Sons, 1996).

120. Tan, I., Ahmad, A. & Hameed, B. Adsorption of basic dye on high-surface-area activated carbon prepared from coconut husk: Equilibrium, kinetic and thermodynamic studies. *Journal of Hazardous Materials* **154,** 337–346 (2008).

121. Hosseini, M., Mertens, S. F., Ghorbani, M. & Arshadi, M. R. Asymmetrical Schiff bases as inhibitors of mild steel corrosion in sulphuric acid media. *Materials Chemistry and Physics* **78,** 800–808 (2003).

122. Unni, A. B. *et al.* Probing the density variation of confined polymer thin films via simple model-independent nanoparticle adsorption. *Macromolecules* **50,** 1027–1036 (2017).

123. Addou, R., Colombo, L. & Wallace, R. M. Surface defects on natural MoS2. *ACS Applied Materials & Interfaces* **7,** 11921–11929 (2015).

124. Ho, Y.-S. & McKay, G. Sorption of dye from aqueous solution by peat. *Chemical Engineering Journal* **70,** 115–124 (1998).

125. Lagergren, S. Zur theorie der sogenannten adsorption geloster stoffe. *Kungliga svenska vetenskapsakademiens. Handlingar* **24,** 1–39 (1898).

126. Li, D. O., Chu, X. S. & Wang, Q. H. Reaction kinetics for the covalent functionalization of two-dimensional MoS2 by aryl diazonium salts. *Langmuir* (2019).

127. Koehler, F. M., Jacobsen, A., Ensslin, K., Stampfer, C. & Stark, W. J. Selective chemical modification of graphene surfaces: distinction between single-and bilayer graphene. *Small* **6,** 1125–1130 (2010).

128. Zhang, L. *et al.* Electronic structure and chemical bonding of a graphene oxide–sulfur nanocomposite for use in superior performance lithium–sulfur cells. *Physical Chemistry Chemical Physics* **14,** 13670–13675 (2012).

129. Huang, Y. *et al.* Sulfurized activated carbon for high energy density supercapacitors. *Journal of Power Sources* **252,** 90–97 (2014).

130. Girard, H. *et al.* Surface properties of hydrogenated nanodiamonds: a chemical investigation. *Physical Chemistry Chemical Physics* **13,** 11517–11523 (2011).

131. Lin, Y.-C. *et al.* Wafer-scale MoS2 thin layers prepared by MoO 3 sulfurization. *Nanoscale* **4,** 6637–6641 (2012).

132. Kim, I. S. *et al.* Influence of stoichiometry on the optical and electrical properties of chemical vapor deposition derived MoS2. *ACS Nano* **8,** 10551–10558 (2014).

133. Liang, Y., Thorne, J. E. & Parkinson, B. Controlling the electronic coupling between CdSe quantum dots and thiol capping ligands via pH and ligand selection. *Langmuir* **28,** 11072–11077 (2012).

134. Liu, J., Cui, L., Kong, N., Barrow, C. J. & Yang, W. RAFT controlled synthesis of graphene/polymer hydrogel with enhanced mechanical property for pH-controlled drug release. *European Polymer Journal* **50,** 9–17 (2014).

135. Stern, K. H. *High temperature properties and thermal decomposition of inorganic salts with oxyanions* (CRC press, 2000).

136. Turner, N. & Single, A. Determination of peak positions and areas from wide-scan XPS spectra. *Surface and Interface Analysis* **15,** 215–222 (1990).

137. Smith, M. & Ozkan, U. Transient isotopic labeling studies under steady-state conditions in partial oxidation of methane to formaldehyde over MoO3 catalysts. *Journal of Catalysis* **142,** 226–236 (1993).

138. Korányi, T. I., Manninger, I., Paál, Z., Marks, O. & Günter, J. R. Activation of unsupported Co Mo catalysts in thiophene hydrodesulfurization. *Journal of Catalysis* **116,** 422–439 (1989).

139. Peisert, H., Chassé, T., Streubel, P., Meisel, A. & Szargan, R. Relaxation energies in XPS and XAES of solid sulfur compounds. *Journal of Electron Spectroscopy and Related Phenomena* **68,** 321–328 (1994).

140. Brox, B. & Olefjord, I. ESCA studies of MoO2 and MoO3. *Surface and Interface Analysis* **13,** 3–6 (1988).

141. Durbin, T. D., Lince, J. R., Didziulis, S. V., Shuh, D. K. & Yarmoff, J. A. Soft X-ray photoelectron spectroscopy study of the interaction of Cr with MoS2 (0001). *Surface Science* **302,** 314–328 (1994).

142. Worley, C., Vannet, M., Ball, G. & Moddeman, W. Surface chemistry of a microcoated energetic material, pentaerythritoltetranitrate (PETN). *Surface and Interface Analysis* **10,** 273–279 (1987).

143. Gaarenstroom, S. & Winograd, N. Initial and final state effects in the ESCA spectra of cadmium and silver oxides. *The Journal of Chemical Physics* **67,** 3500–3506 (1977).

144. Ettema, A. & Haas, C. An X-ray photoemission spectroscopy study of interlayer charge transfer in some misfit layer compounds. *Journal of Physics: Condensed Matter* **5,** 3817 (1993).

145. Laajalehto, K., Kartio, I. & Nowak, P. XPS study of clean metal sulfide surfaces. *Applied Surface Science* **81,** 11–15 (1994).

146. Chadwick, D. & Hashemi, T. Adsorbed corrosion inhibitors studied by electron spectroscopy: benzotriazole on copper and copper alloys. *Corrosion Science* **18,** 39–51 (1978).

147. Dake, L., Baer, D. & Zachara, J. Auger parameter measurements of zinc compounds relevant to zinc transport in the environment. *Surface and Interface Analysis* **14,** 71–75 (1989).

148. Zhi, L., Zuo, W., Chen, F. & Wang, B. 3D MoS2 composition aerogels as chemosensors and adsorbents for colorimetric detection and high-capacity adsorption of Hg2+. *ACS Sustainable Chemistry & Engineering* **4,** 3398–3408 (2016).

149. Jia, F., Zhang, X. & Song, S. AFM study on the adsorption of Hg 2+ on natural molybdenum disulfide in aqueous solutions. *Physical Chemistry Chemical Physics* **19,** 3837–3844 (2017).

150. Wang, J. *et al.* One-pot synthesis of multifunctional magnetic ferrite–MoS2–carbon dot nanohybrid adsorbent for efficient Pb (ii) removal. *Journal of Materials Chemistry A* **4,** 3893–3900 (2016).

151. Jensen, W. B. Overview Lecture The Lewis acid-base concepts: recent results and prospects for the future. *Journal of Adhesion Science and Technology* **5,** 1–21 (1991).

152. Aghagoli, M. J., Beyki, M. H. & Shemirani, F. Application of dahlia-like molybdenum disulfide nanosheets for solid phase extraction of Co (II) in vegetable and water samples. *Food Chemistry* **223,** 8–15 (2017).

153. Wang, Z. *et al.* Chemical dissolution pathways of MoS2 nanosheets in biological and environmental media. *Environmental Science & Technology* **50,** 7208–7217 (2016).

154. Kittel, C. Introduction to solid state physics, John Wiley & Sons. *Inc., New York* (2005).

155. Chen, Q., Ouyang, Y., Yuan, S., Li, R. & Wang, J. Uniformly wetting deposition of Co atoms on MoS2 monolayer: a promising two-dimensional robust half-metallic ferromagnet. *ACS Applied Materials & Interfaces* **6,** 16835–16840 (2014).

156. Ataca, C. & Ciraci, S. Functionalization of single-layer MoS2 honeycomb structures. *The Journal of Physical Chemistry C* **115,** 13303–13311 (2011).

157. Donarelli, M., Bisti, F., Perrozzi, F. & Ottaviano, L. Tunable sulfur desorption in exfoliated MoS2 by means of thermal annealing in ultra-high vacuum. *Chemical Physics Letters* **588,** 198–202 (2013).

158. Zhang, X. *et al.* Poly (4-styrenesulfonate)-induced sulfur vacancy self-healing strategy for monolayer MoS2 homojunction photodiode. *Nature Communications* **8,** 15881 (2017).

159. Nguyen-Phan, T.-D. *et al.* Reduced graphene oxide–titanate hybrids: morphologic evolution by alkali-solvothermal treatment and applications in water purification. *Applied Surface Science* **258,** 4551–4557 (2012).

160. Zhang, H. & Lee, H. K. Plunger-in-needle solid-phase microextraction with graphene-based sol–gel coating as sorbent for determination of polybrominated diphenyl ethers. *Journal of Chromatography A* **1218,** 4509–4516 (2011).

161. Chen, J. *et al.* Preparation and evaluation of graphene-coated solid-phase microextraction fiber. *Analytica Chimica Acta* **678,** 44–49 (2010).

162. Shehzad, K., Xu, Y., Gao, C. & Duan, X. Three-dimensional macro-structures of two-dimensional nanomaterials. *Chemical Society Reviews* **45,** 5541–5588 (2016).

163. Wang, L. *et al.* Fundamental transport mechanisms, fabrication and potential applications of nanoporous atomically thin membranes. *Nature Nanotechnology* **12,** 509 (2017).

164. Pinto, M. L. Formulation, preparation, and characterization of polyurethane foams. *Journal of Chemical Education* **87,** 212–215 (2010).

165. DERNEHL, C. U. Health hazards associated with polyurethane foams. *Journal of Occupational and Environmental Medicine* **8,** 59–62 (1966).

166. Bowen, H. Trace Elements in Biochemistry Academic Press. *London-New York,* 189–193 (1966).

167. Sitko, R. *et al.* Green approach for ultratrace determination of divalent metal ions and arsenic species using total-reflection X-ray fluorescence spectrometry and mercapto-modified graphene oxide nanosheets as a novel adsorbent. *Analytical Chemistry* **87,** 3535–3542 (2015).

168. Ge, J. *et al.* Joule-heated graphene-wrapped sponge enables fast clean-up of viscous crude-oil spill. *Nature Nanotechnology* **12,** 434 (2017).

169. Liu, J., Yu, M., Wang, X.-C. & Zhang, Z. A highly selective colorimetric sensor for Hg2+ based on nitrophenyl-aminothiourea. *Spectrochimica Acta Part A: Molecular and Biomolecular Spectroscopy* **93,** 245–249 (2012).

170. Ulewicz, M., Sadowska, K. & Biernat, J. F. Facilitated transport of Zn (II), Cd (II) and Pb (II) across polymer inclusion membranes doped with imidazole azocrown ethers. *Desalination* **214,** 352–364 (2007).

171. Arvand, M., Moghimi, A. M., Afshari, A. & Mahmoodi, N. Potentiometric membrane sensor based on 6-(4-nitrophenyl)-2, 4-diphenyl-3, 5-diaza-bicyclo [3.1. 0] hex-2-ene for detection of Sn (II) in real samples. *Analytica Chimica Acta* **579,** 102–108 (2006).

172. Kumar, B. N., Venkata Ramana, D., Harinath, Y., Seshaiah, K. & Wang, M. Separation and preconcentration of Cd (II), Cu (II), Ni (II), and Pb (II) in water and food Samples using Amberlite XAD-2 functionalized with 3-(2-Nitrophenyl)-1 H-1, 2, 4-triazole-5 (4 H)-thione and determination by Inductively Coupled Plasma–Atomic Emission Spectrometry. *Journal of Agricultural and Food Chemistry* **59,** 11352–11358 (2011).